QATAR UNIVERSITY

COLLEGE OF ENGINEERING

TRIBO-MECHANICAL, BIOCOMPATIBILITY, AND CORROSION PROPERTIES INVESTIGATION OF ZIRCONIUM AND SST 304 BY APPLICATION OF HYDROXYAPATITE/REDUCED GRAPHENE OXIDE/PALLADIUM-PLATINUM NANOCOMPOSITE COATINGS

BY

HUDA FADOL S. ALYAFEI

A Dissertation Submitted to

the College of Engineering

in Partial Fulfillment of the Requirements for the Degree of

Doctorate of Philosophy in Materials Science and Engineering

January 2020

COMMITTEE PAGE

The members of the Committee approve the Dissertation of

Huda Fadol S. AlYafei defended on 10/12/2019.

_____

Prof. Abdel Magid Hamouda
Thesis/Dissertation Supervisor

_____

Dr. Mohamed Arselene Ayari
Office of Graduate Studies Representative

_____

Prof. Elsadig Mahdi
Committee Member

_____

Prof. Faris Tarlochan
Committee Member

_____

Prof. Tahir Khan
Committee Member (External)

Approved:

_____

Khalid Kamal Naji, Dean, College of Engineering

ABSTRACT

ALYAFEI, HUDA, F., Doctorate : January : 2020,

Doctorate of Philosophy in Materials Science and E

Title: Tribo-Mechanical, Biocompatibility, and Corrosion Properties Investigation of Zirconium and SST 304 by Application of Hydroxyapatite/Reduced Graphene Oxide/Palladium-Platinium Nanocomposite Coatings

Supervisor of Dissertation: Prof. Abdel Magid, Hamouda.

This thesis describes the synthesis of HA/rGO/Pd and HA/rGO/Pt nanocomposite thin film coatings on stainless steel 304 and pure zirconium applied via an electrodeposition method. The corrosion and biocompatibility characteristics of HA/rGO/Pd and HA/rGO/Pt nanocomposite thin films are investigated here. Biocompatibility tests were carried out on uncoated, HA-coated, HA/rGO-coated, HA/rGO/Pd-coated, and HA/rGO/Pt-coated substrates using the human cell line MDA-MB-231, which had a green fluorescent protein to report the presence of living cells. Experiments revealed that the biocompatibility of the SST 304 surface showed the best cell spreading and proliferation when coated with the HA/rGO/Pd nanocomposite. The zirconium substrate coated with HA/rGO/Pt showed decreased cell proliferation and adhesion compared with HA/rGO, showing that Pt did not improve the biocompatibility.

A synthetic medium was used to conduct corrosion tests, which confirmed that the HA/rGO/Pd-coated SST 304 had a significantly higher corrosion resistance than the uncoated, HA-coated, and HA/rGO-coated SST 304 samples. In addition, the HA/rGO/Pd-coated SST 304 and the HA/rGO/Pt-coated zirconium substrates were annealed at different temperatures (200, 300, 400, and 600 ^{o}C) to investigate their corrosion and wear behaviors.

The HA/rGO/Pd-coated substrate annealed at 600 °C showed better wear resistance compared with the other samples. The wear tests result of bare and electrodeposited specimens before and after heat treatment for the HA/rGO/Pt showed that the coated samples heated at 300 °C had superior resistance against wear compared with bare and electrodeposited substrates at other annealing temperatures.

DEDICATION

Thank you to my academic adviser who guided me in this process and my co-adviser who kept me on track. .

Many Thanks for my family who inspired me to pursue my doctoral degree

ACKNOWLEDGMENTS

First, praises and thanks to the God, the Almighty, for His showers of blessings throughout my research work to complete the research successfully. I would like to express my deep and sincere gratitude to my research supervisor, Dr.Abdalmagid Hamouda and co-advisor, Dr.Erfan Zalnezhad.

TABLE OF CONTENTS

LIST OF TABLES

LIST OF FIGURES

LIST OF ABBREVIATIONS

316LSS: 316L stainless steel

AgCl: silver chloride

Al: aluminum

ALP: activity of alkaline phosphate

Ar: argon

BICV: bone-implant contact value

C: carbon

Ca: calcium

$CaCl_2$: calcium chloride

CNTs: carbon nanotubes

Co: cobalt

Co-Cr: cobalt-chromium

COF: coefficient of friction

Cr: chromium

Cu: copper

CVD: chemical vapor deposition

DMEM: Dulbecco's Modified Eagle's Medium

ECD: electrochemical deposition

EDS: energy dispersive spectroscopy

EDX: energy-dispersive X-ray spectroscopy

EEC: electrical equivalent circuit

EIS: electrochemical impedance spectroscopy

Fe: iron

FESEM: field emission scanning electron microscopy

FTIR: Fourier-transform infrared spectroscopy

GFP: green fluorescent protein

GO: graphene oxide

H_2O: water

H_2O_2: hydrogen peroxide

H_2SO_4: sulfuric acid

HA: hydroxyapatite

HAP: hydroxylapatite

HCl: hydrochloric acid

HF: hydrofluoric acid

hMSC: human mesenchymal stem cells

K_2PtCl_4: potassium tetrachloroplatinate

KBr: potassium bromide

$KMnO_4$: potassium permanganate

MEA: microelectrode arrays

Mg: magnesium

mRNA: messenger ribonucleic acid

MSC: mesenchymal stem cells

NaCl: sodium chloride

NaOH: sodium hydroxide

NBCS: newborn calf serum

$NH_4H_2PO_4$: ammonium dihydrogen phosphate

$NH_4H_2PO_4$: mono ammonium phosphate

Ni: nickel

O: oxygen

OCP: open circuit potential

ODH: oxygen diffusion hardening

P.E.: protection efficiency

P: phosphorous

Pd: palladium

PDS: Potentiodynamic scan

PMMA: poly(methyl methacrylate)

Pt: platinum

PTFE: poly(tetrafluoroethylene)

PVD: physical vapor deposition

R&D: Research and development

rGO: reduced graphene oxide

SAM: self-assembled monolayer

SCE: saturated calomel electrode

SEM: scanning electron microscopy

SiC: silicon carbide

SST: stainless steel

St: antimony

TEM: transmission electron microscopy

THR: total hip replacement

Ti: titanium

TiN: titanium nitride

TKR: total knee replacement

UHMWPE: ultra-high-molecular-weight polyethylene

XRD: X-ray diffraction

Zr: zirconium

β-TCP: β-tricalcium phosphate

Chapter 1 : Introduction

1.1 Research Background

Many different implants (bone plates, ligaments, joint replacements, heart valves, intraocular lenses, vascular grafts, dental implants, and sutures) and devices (blood tubes, artificial hearts, biosensors, and pacemakers) are currently used in the medical field. Medical devices and implants are made of biomaterials to restore and/or replace the function of degenerated or traumatized organs or tissues to correct abnormalities, improve function, assist in healing, and consequently improve the quality of life of patients [1].

Today, one of the most challenging tasks in materials science is the development of new biomaterials for medical applications. The need for better implants is obvious, and thus the capability to manufacture artificial tissues is highly demanded [2].

One of the most vital factors that differentiate biomedical materials from other materials is that they must be biocompatible and non-toxic in a manner that does not harm human tissues. The development of sustainable biomaterials that coexist with tissues in a mutually acceptable manner has long been of interest in the field of biomaterials and to medical device users [3].

The high concentrations of interstitial fluid and chloride ions in serum creates an extremely corrosive environment for bio-metallic materials. Body fluid (containing electrolytes) contains numerous proteins and amino acids that corrode metallic materials. Furthermore, the dissolved oxygen concentration in the bodily fluid is low, which delays the regeneration of oxide layers on metallic biomaterials, and when the film is detached, many metal ions are released [4, 5].

Hence, to improve the performance of implants *in vitro* and *in vivo*, it is essential to control the interfacial behaviors between the implant and host. Surface treatments can successfully change the chemical and physical properties of the surface of biomaterials to extend and enhance the functionalities and properties of the original materials. Such treatments can decrease the undesirable interfacial interactions between implants and their surrounding biological environment. For decades, many surface treatment techniques have been developed to eventually upgrade the hemocompatibility and biocompatibility of zirconium-based alloys. These techniques include the deposition of polymer coatings or inorganic thin films (zirconium nitride, diamond-like carbon, zirconium oxide, etc.), and the fabrication of a multifunctional layer to immobilize biomolecules via wet chemical methods [6-9]. Due in part to these advances, considerable progress has been made in the areas of blood compatibility and biocompatibility.

In this study, hydroxyapatite (HA)-based composite coatings, reduced graphene oxide (rGO), and pure platinum (Pt) and palladium (Pd) were deposited on zirconium (Zr) and SST 304 substrates via electrodeposition. The overall goal of this research was to produce a biocompatible hybrid ceramic-metal coating, reinforced with graphene oxide, to simultaneously enhance the biomaterial's corrosion and wear resistance. The tribo-biomechanical properties and corrosion resistance of the composite-coated substrates were evaluated. Structural and morphological analysis and characterizations were performed using transmission electron microscopy (TEM), scanning electron microscopy (SEM), X-ray diffraction (XRD), and Fourier-transform infrared (FTIR) spectroscopy.

1.2 Research Problem Statement

Materials and alloys made from titanium, zirconium, and stainless steel have a desirable combination of good mechanical properties and high biocompatibility, making them ideal materials for applications that require them to come in contact with hard and/or soft tissue, such as in implants [10, 11]. The low elastic modulus (close to the bone) and high fatigue strength of these alloys has made them the preferred choice, particularly in the replacement of hard tissue, e.g., as anchoring parts in total hip and knee arthroplasty [12]. Titanium high biocompatibility and the body does not recognize it as foreign material in cellular environments [13, 14]. However, shortly after implantation, aseptic loosening of titanium-based prostheses may occur, resulting in relative movement between hard tissue/bone cement which may potentially form debris from the prosthesis surface whose particles form a native oxide layer that is only a few nanometers thick with low mechanical stabilities [15]. These generated small abrasive particles cause an inflammatory reaction of the surrounding tissue, which eventually causes bone loss [1-17]. Various methods have been researched to improve the surface tribological properties of titanium in several reports.

1.3 Importance of Study

To describe the benefits of the currently proposed research project, it is necessary to consider both the economic and technological justification for using a nanocomposite thin layer coating atop the aforementioned alloys. In this regard, the following key points will be considered to assess the merits of the proposed project:

- Vast application of stainless steel and zirconium alloys in marine, aviation, and biomedical applications.

- Superior mechanical and physical properties of stainless steel and zirconium.
- The role of HA/rGO/Pt and HA/rGO/Pd nanocomposites in enhancing the tribo-mechanical, corrosion, biocompatibility, and physical properties of stainless steel and zirconium (implants) by a combination of electrodeposition and heat treatment techniques.

Stainless steel and zirconium play leading roles in energy, aviation, biomedical, and marine industries due to the superior mechanical and physical properties. In early research and applications, the focus of stainless steel and zirconium was on their high specific strength, impact strength, creep resistance, and high fatigue life, even at elevated temperatures. Attention was later given to the unique corrosion resistance and non-magnetic properties of stainless steel and zirconium. Currently, the use of stainless steel and zirconium in different engineering structures has become more prominent.

The design and manufacture of medical devices must be precise, especially in a world progressively fixated on retribution claims and lawsuits for damage or injury incurred through medical negligence. Thus, any material coming into contact with or being surgically implanted inside the body must be accomplished without fail, making this one of the most challenging engineering problems facing the medical industry. Medical devices must be created in a variety of sizes and shapes to suit their wide range of applications. This has led to the development and use of many different materials to ensure precise design specifications.

HA has often been used because of its high biocompatibility, but it has a low fracture toughness which leads to failure in the body due to cracking and fracture. The mechanical

properties of these unique materials (HA) can be enhanced by making a composite of HA/rGO/Pd and HA/rGO/Pt. Furthermore, a study on the nanostructured morphology of nanocomposites is becoming increasingly necessary since these properties rely on the morphology of a material.

1.4 Objectives of the Study

The purpose of this research is to develop and characterize the properties of stainless steel and zirconium alloys coated with reduced graphene oxide-hydroxyapatite-palladium (HA/rGO/Pd) and reduced graphene oxide-hydroxyapatite-platinum (HA/rGO/Pt) nano-composites. Specifically, the research aims are to achieve the following objectives:

i. To characterize and analyze the structure and morphology of HA/rGO/Pd and HA/rGO/Pt nanocomposites.
ii. To examine the wear resistance of the HA/rGO/Pd and HA/rGO/Pt nanocomposites.
iii. To investigate the corrosion behavior of the substrates coated by HA/rGO/Pd and HA/rGO/Pt nanocomposites.
iv. To study the biocompatibility of HA/rGO/Pd and HA/rGO/Pt nanocomposites.

1.5 Research Methodology

The substrates were purchased commercially as plates, which were cleaned and polished using silicon carbide papers with grade sizes of up to 2400. The plates were washed using ultrasonication in a beaker containing acetone and were finally rinsed using distilled water to remove any surface suspensions.

HA/rGO/Pd and HA/rGO/Pt nanocomposite thin films were deposited using electrodeposition and heat treatment techniques. The rGO, palladium, platinum, and HA

were mixed at different weight percent (wt%) to determine the optimal loading for the best surface integrity and higher biocompatibility. Several samples were prepared for corrosion and wear resistance and biocompatibility tests.

Chapter 2 : Literature Review

2.1 Introduction

The history biomaterials as a professionally-recognized field of study can be traced to 1969 when the first conference on biomaterials was held at Clemson University, South Carolina, USA. Since then, the field has continued to command substantial attention on different societal fronts. By definition, biomaterials are natural or manmade materials that are utilized to make structures or implants used in the human body as replacements to lost or compromised biological structures to restore functionality. As a result, biomaterials play critical roles in either enhancing the quality of life or prolonging the life of human beings. This is true given the significance of these materials in replacing lost or impaired body parts or organs. As the aging population continues to increase, the demand for biomaterials is rapidly growing, which has caused the popularity and research and development in this field to increase. Applications of biomaterials on the human body are numerous and range from artificial heart valves and installations of stents in blood vessels to a number of replacement implants such as knees, oral dental structures, and shoulders, as well as hips and ears [18-20]. Biomaterials have also seen use as cardiac simulators and as construction for compromised urinary tracts.

However, of the various applications, the use of biomaterials as replacement implants on the spinal cord, hip, and knee are increasingly common in modern society. This trend is likely occurring because of the naturally high vulnerability of human joints which are affected by degenerative health complications such as arthritis, which are not only highly painful but also a common cause of loss of function. An estimated 90% of adults aged 40

years and above are afflicted by one or more degenerative diseases [21]. This is a major public health concern given the rapidly increasing percentage of the aging population, a trend that is expected to continue or even worsen in the foreseeable future. Estimated to cost society about $125 billion every year, musculoskeletal disorders are among the most common health complications in modern society [22]. Biomaterials are increasingly proving to be the ultimate solution to treat these and other disabilities and health problems since implants can conveniently restore the functional health of otherwise compromised body parts. Figure 2.1 provides examples of implants on the hip and knee joints using biomaterials. Available statistics show that demand for long-lasting implants has been increasing, and by 2030, it is estimated that the number of hip replacement implant procedures will increase by 174%, and knee implants by more than 670% [23].

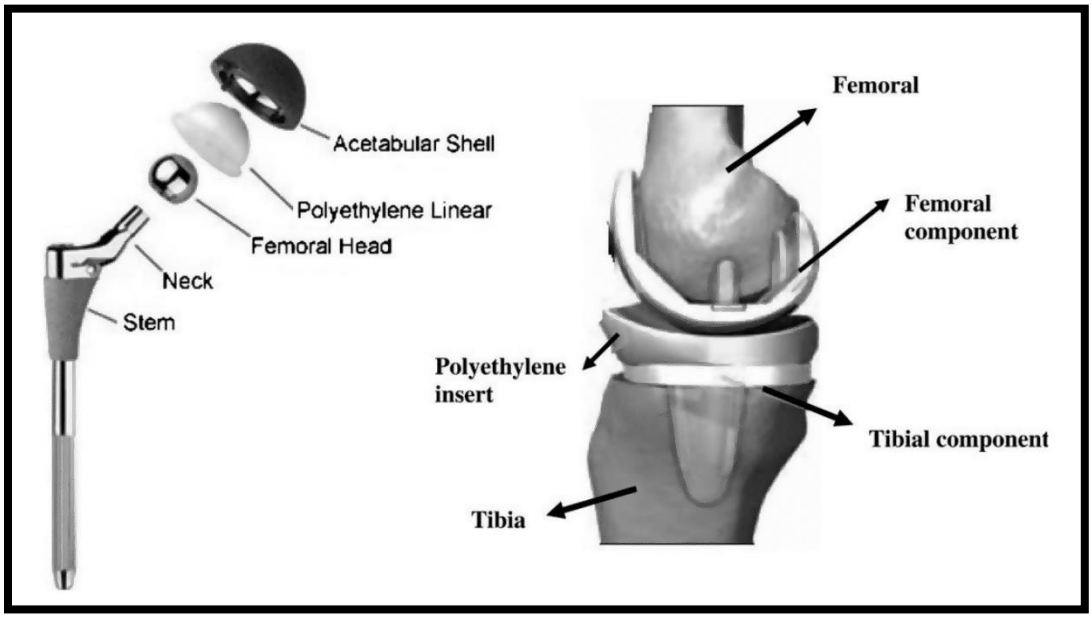

Figure 2.1. Total hip and knee implants replacements (THR and TKR) [23].

In addition to an increasing number of replacement implants, there is a growing trend in the number of revision surgeries on hip and knee implants. However, revision surgeries are not only painful and expensive but also generally have poor success rates. Despite these concerns, the number of revision surgeries is expected by an increase of 137 percent and 607 percent for hip and knee implants respectively by 2030 [24]. This implies great future business prospects for the implant manufacturing industry and a need to accelerate the research and development of biomaterials for enhanced efficacy in meeting the specific needs of a rapidly growing market. For example, biomaterials for use in orthopedic implants should be biocompatible, corrosion-resistant in bodily settings, and have high strength [25]. In addition, these materials should have low moduli, no cytotoxicity, and

should be highly resistant to fatigue and wear [26]. Currently, common materials used for orthopedic implants include 316L stainless steel and different alloys of cobalt, chromium, and titanium, which all have high failure tendencies in long-term use. This problem has been blamed on the fact that these materials generally have high moduli, poor biocompatibility, and poor resistance to wear and corrosion. Figure 2.2 shows some of the common causes for revision surgery.

However, the increasing number of revision surgeries has also risen with longer life expectancies. For example, THR has traditionally been used on individuals 65 years and older, with expected life longevity of about another 15 years [27]. However, as medical technology advances, people are living longer than before, which increases the likelihood of requiring additional revision surgeries. The problem of earlier implants has also been increased by modern high-impact sporting activities and an ever-growing problem of fatal accidents from different sources. This implies that implants have increased expectations to last longer than before, hence the need for continued investment of resources and concerted efforts in R&D to develop new reliable biomaterials.

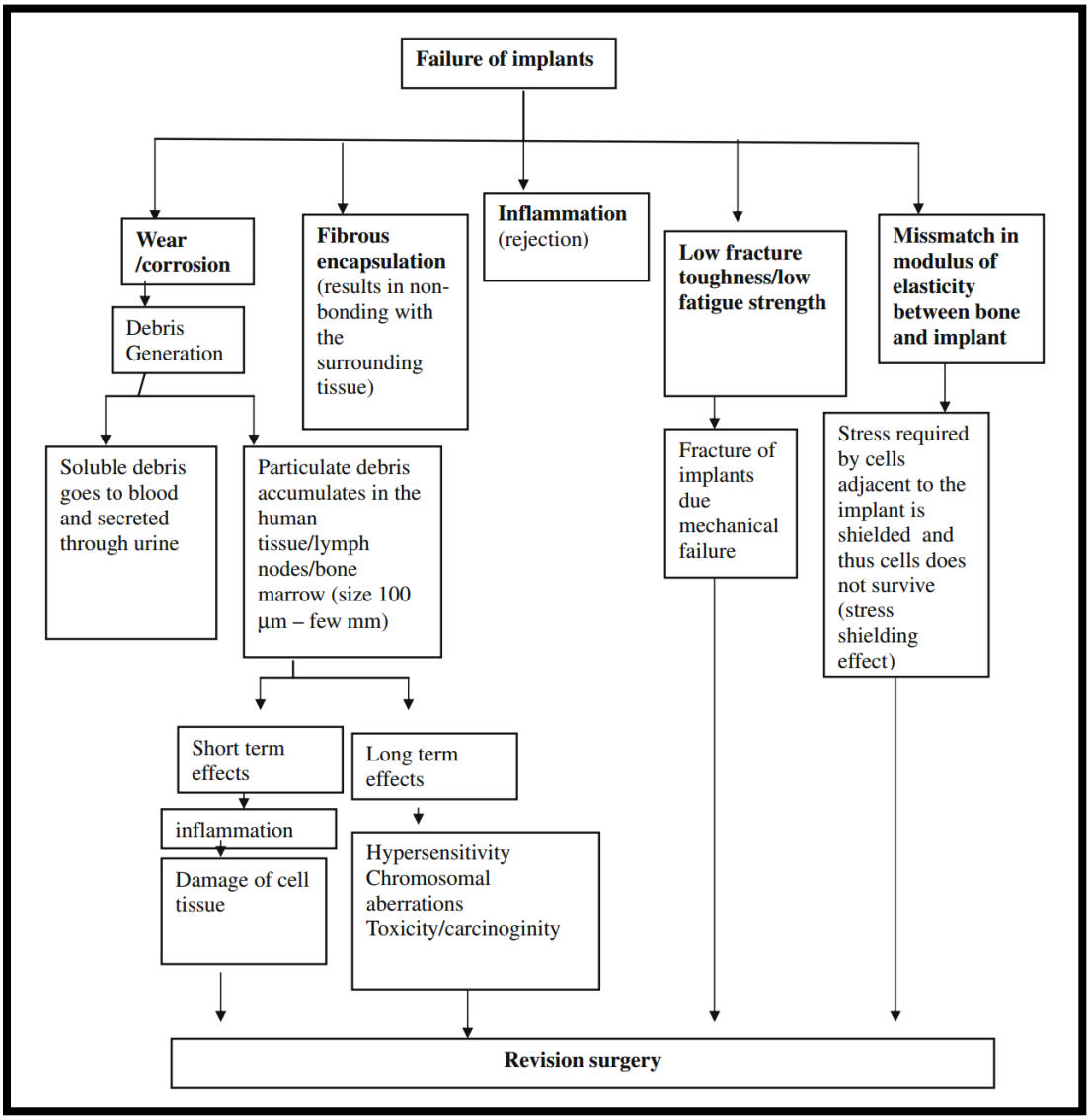

Figure 2.2. Various causes for failure of implants leading to revision surgery [27].

Recently, there has been increased recognition and activity of nanotechnology as an interdisciplinary field that merges nanoelectronics with biomaterials. Currently, there are three main areas of nanotechnology that are used in biomedicine: diagnostic techniques,

drugs, and prostheses and implants. However, there is a growing interest in developing and utilizing external biomedical applications. This is evident with developments such as diagnostic sensors and "lab-on-a-chip" techniques and their use in blood analysis and other body samples as well as continued growth in the number of analytical instruments used for R&D activities on medical drugs. Some applications of nanotechnology inside the human body include the development of anticancer drugs and insulin pump implants. This is complemented by the potential application of nanotechnology in tissue engineering and their associated benefits in securing reliable solutions for restoring functional health to people who have lost or compromised body parts [28, 29]. The list of nanotechnology application devices is extensive, but this study is limited to orthopedic joint prostheses and hip and knee arthroplasty.

Many factors impact the survivability or expected longevity of arthroplasty, and key among these is the age of the individual. To put this into perspective, the failure rate of arthroplasty within 10 years in patients over 65 years in around seven percent, but in patients below 65 years, the failure rate is estimated above 15 percent on average. This implies that continual increases in the number of replacement implants result in a subsequent increase in the number of revision surgeries, which makes the quality of implants a priority public health concern. Thus, R&D on more reliable implants and biomaterials is critical to improving societal health, as well as psychological and socioeconomic problems associated with revision surgeries. The widespread adoption and use of nanoscience and engineering is a promising development to increase the R&D of highly biocompatible biomaterials for use within humans [30-33]. In biomaterials R&D, emphasis should be placed on the

mechanical properties of the material such as it relates to the material-biological interface [34].

Furthermore, it is imperative that manipulation of the mechanical properties of biomaterials using technology should be informed by great care to mitigate undue effects on the response of body cells and associated effects on physiological responses [35]. Carbon nanotubes (CNTs) have been used in materials over the past several decades due to their high strength, making them ideal candidates for different applications. However, the successful adoption of these materials *in vivo* has been compromised by physiological issues. For example, the introduction of pristine nano-functionalized CNTs in polymer matrixes continues to be inhibited by this nanomaterial being insoluble, which allows it to accumulate in the body and cause adverse health effects [36]. The solution to this has been to chemically alter the surfaces of the CNTs to improve their solubility in common solvents and polymers [37].

However, the main issue of concern is that the expected life of joint implants is currently only 10 to 15 years, beyond which the risk of failure and the risk of seeking revision surgery is high. A core reason for these failures is the loosening of the implant aseptic from juxtaposed bone, which has seen increased use of polymethyl methacrylate (PMMA) in orthopedics as a better option to enhance the bonding of the implant-bone interface. Nevertheless, the use of PMMA cement has also been associated with disadvantages in terms of compromising the efficacy of implant replacements, including strong exothermic reactions and negated radiopacity and fatigue strength. Overall, as society expects to witness future increases in the demand for orthopedic implants, the expected lifespan of

current implants cannot be assumed to be reliable as they are increasingly subject to the pain and cost of revision surgeries. This requires increased R&D investments for more innovative biomaterials that are reliable, biocompatible, and durable, which calls for the informed usage of nanotechnology principles and capabilities in the development of biomaterials [38-40].

There are a variety of composite materials available that can be used to develop a biologically-informed composite system, including bone cement-like PMMA which continues to be extensively used in orthopedic surgeries. In particular, PMMA is used here as a biomaterial to enhance the fixing of an artificial joint to a bone, and also serves as filler material for bone defects [41]. There is also evidence that PMMA is used as a platform for facilitating drug delivery into and between joined areas. However, it is well documented that the ultimate efficacy of PMMA cement in fixing implants to bones depends on the primary mechanical properties of both the PMMA and the implant. The primary solution used to address this challenge is the use of hydroxyapatite (HA), a complementary material to PMMA used to improve the mechanical properties [42]. HA has many benefits such as being able to chemically bonding with bone which reduces the chances of joint loosening over time. However, this chemical bonding has been blamed for the intrinsic brittleness of the bone near the joint area which compromises the strength of the joint [43].

2.2 Requirements of a Biomaterial

It is important that the proper material is chosen for a certain application since different biomaterials have different physical and mechanical properties, and hence different suitability for different medical applications. To successfully develop new biomaterials, a

multidisciplinary effort and collaboration are required to ensure informed consideration of different concerns from different perspectives.

2.2.1 Mechanical properties

To ensure that a best-fit material is selected for a specific application, the consideration of a material's mechanical properties, including its hardness, tensile strength, modulus, and elongation, is critical. The fatigue strength of a material is important as it informs the response behavior of a material when exposed to repeated loading cycles. Implants should be made to specifications to ensure their biomechanical compatibility for use in a specific application. Concerning the modulus, the general rule is that the modulus of material should be the same or similar to that of the bone it will be used on, whose modulus values depend on the type of the bone and the measurement direction [44, 45]. Implants with a modulus higher than that of the bone are more vulnerable to failures due to biomechanical incompatibility and risks causing the death of bone cells [46]. Thus, an excellent implant material should have the highest possible strengths and a modulus as similar to that of the bone as possible.

2.2.2 Biocompatibility

Biocompatibility is critical to define the quality of biomaterials for implants. To be deemed high-quality, material should be non-toxic, nor should it cause any form of allergic reactions in the human body. This requires that the selection of the implant material is well informed to mitigate undue reactions with body cells and tissues [47]. Two of the core factors that impact the biocompatibility of a material are its degradation rate (or the risk of the material within the body environment) and the material-induced response by the body

or the host. Table 2.1 shows the general classification of biomaterials based on the body's response. An important point here is the fact that bioactive materials are generally preferred for use as biomaterials because they increase the chances of smooth integration into a body near the joint area. Some of the main issues of concern in determining biocompatibility include thrombosis and fibrous tissue encapsulation of biomaterials implanted in soft tissues.

Table 2.1: Classification of biomaterials based on interaction with surrounding tissues[47]

Classification	Response	Examples	Effect
Biotolerant materials	Formation of thin connective tissue capsules (0.1–10 μm) and the capsule does not adhere to the implant surface	Polymer-poly tetra fluorethylene (PTFE), polymethyl metha acralyte (PMMA), Ti, Co–Cr, etc.	Rejection of the implant leading to failure of the implant
Bioactive materials	Formation of bony tissue around the implant material and strongly integrates with the implant surface	Bioglass, synthetic calcium phosphate including hydroxyl apatite (HAP)	Acceptance of the implant leading to success of implantation
Bioreabsorbable materials	Replaced by the autologous tissue	Polylactic acid and polyglycolic polymers and processed bone grafts, composites of all tissue extracts or proteins and structural support system	Acceptance of the implant leading to success of implantation

2.2.3 High corrosion and wear resistance

Poor resistance to wear and corrosion when interacting bodily fluid prompts the release of non-compatible substances, especially metal ions from the implants into the body, which increases the risk that the implant will cause an inflammatory reaction in the body [48]. As a result, the expected lifespan of an implant depends to some extent on the resistance it has to abrasion and wear. Materials with low wear resistance are more vulnerable to loosening within a short duration after the procedure, and debris from the wear can have undue effects on body tissues [49]. Thus, ensuring high resistance to wear and corrosion is one of the best practices in enhancing the safety and longevity of implants.

2.2.4 Osseointegration

An implant's failure to integrate well with not only the target bone but also the adjacent bones and tissues is an indication of a poor-quality biomaterial or implant material because such risks subsequently loosen the implant [49]. This is an especially major concern given

that poor integration forms a fibrous tissue between the bone and the implant [50]. As a result, the selection of an implant material should consider the appropriateness of the surface of the implant to allow for integration with adjacent bones and tissues. Some factors to consider here include surface chemistry, surface roughness, and surface topography.

2.3 Currently Used Metallic Biomedical Materials and Their Limitations

The biomaterials in use include 316L stainless steel (316LSS), cobalt-chromium (Co–Cr) alloys, and titanium and its alloys. More details on the suitability of common elements in these materials are given in Table 2.1. Biotolerant materials are typically used to form thin connective tissue capsules (0.1–10 μm), but in general, the capsule does not adhere to the implant surface poly(tetrafluoroethylene) (PTFE), (PMMA), Ti, or Co–Cr or other biomaterials. This, in turn, leads the body to reject the implant, causing it to fail prematurely. Bioactive materials are particularly important as they enhance the formation of bony tissues around the implant in the body, and ensure strong integration of the implant into the body.

Bioglass, or synthetic calcium phosphate materials, is another common form of metallic biomedical materials currently used with hydroxylapatite (HAP). The acceptance of an implant using this group of biomaterials is generally associated with a high implantation success rate. On the other hand, there are also bioabsorbable materials which function by being replaced by minerals and tissues or being absorbed by bodily chemicals. The main advantage of these materials is that their acceptance by the body makes excellent integration of the implant into the body. M. Geetha et al. argued the need to negate the use of stainless steel and cobalt-chromium alloys because these metallic biomaterials suffered

from undue corrosion in the body [51]. Wapner, on the other hand, compared the toxic effects of metallic implants and non-metallic implants such as Ni, Co, and Cr [52]. An important point here is that the toxicity of Ni implants was found to cause skin-related diseases, especially dermatitis, and a close link was found between Co implants and the carcinogenicity [53].

The use of Zr as or in biomaterials is relatively a new concept. However, from the few research studies available, Zr implants have been shown to achieve an 86 percent bone-implant contact value (BICV) within 8 weeks after the procedure. Other research studies have, however, shown a BICV of between 45 and 65 percent. According to a research study by Stanic et al., the average BICV was 56 percent within 60 days after the implant. Using a rat model, Scerano et al. argued that there is an actual bone-implant contact for Zr implants, which secured a BICV of 68 percent within 4 weeks. Based on the same assumptions, Aldini et al. only found a BICV of 55 percent (± 27%) 60 days after the procedure. However, the BICV varied significantly depending on the implant location, implying a similarity between the osseointegration attributes of zirconium implants and those of titanium implants.

Sennerby et al. compared the osseointegration characteristics of different groups of Zr and Ti implants using different surface modifications and showed that both categories of implants had relatively good osseointegration. In terms of surface modification, it was challenging to modify the surface of zirconium implants to suit situational requirements, but it was comparatively easy for titanium implants using methods such as sand-blasting and acid-etching. To ensure the competitive use of zirconium implants, it is imperative to

identify reliable techniques to modify its surface, and the use of a thin film nanocomposite metal-ceramic coating is one possible technique [54-56]. Other attributes of Zr implant (treated with different techniques) such as their bioactivity and resistance to corrosion have been studied. These techniques include sol-gel processes, anodization and plasma electrolytic oxidation, as well as the use of physical vapor deposition and thermal oxidation [57, 58].

Another biomaterial currently in use is hydroxyapatite (HA) which is the main mineral component of human bones and teeth, making it a suitable material for use as a bioceramic [59]. It boasts excellent biocompatibility properties and can bond to the bone to form unions that are impossible to differentiate from natural bonds, allowing it to be readily integrated into the human body [60]. There are numerous studies exploring various human body systems based on graphene oxide, hydroxyapatite, and other composites as potential biomaterials [61-67].

Platinum is another commonly-used biomaterial which boasts high biocompatibility, electrochemical stability, and excellent mechanical attributes relative to the body tissue. Minev et al. argued that combining composite coatings and elastomer-based microelectrode arrays (MEAs) could enhance MEA compatibility with highly-deformable substrates [68]. Negrete et al., on the other hand, explored the use of magnesium- and platinum-doped hydroxyapatite nanoparticles as multifunctional biocompatible bactericidal composites [69]. Overall, they suggested the possible use of HA/Mg/Pt nanoparticles as antimicrobial agents.

Research on biomedical applications has attracted an increasing amount of attention among

scholars, a trend that is closely associated with the implication of this field to human health [70]. Of particular importance, R&D efforts on innovative solutions to the world of medical devices are becoming a priority research interest in this field. This is because medical devices interact and directly contact the human body, which requires precision in design and manufacturing to ensure safety and efficacy. In terms of materials currently used in medical devices, stainless steel 304 (SST 304) is the most common because it has excellent corrosion resistance and a native surface passive layer. However, SST 304 has been reported to corrode when exposed to fluids containing halide ions, which limits its application scope as a biomaterial [71-74].

On the other hand, calcium phosphate bioceramics such as those based on HA and β-tricalcium phosphate (β-TCP), have recently gained popularity in biomedical applications not only because of their competitive biocompatibility but also due to their excellent osteoconductivity. In particular, HA has been recognized for its excellent rapid integration with the body to form an indistinguishable union. However, when used in its pure form, the mechanical attributes of HA are quite poor, especially as they relate to the lack of toughness and its poor resistance to wear. The widespread suitability of HA in biomedical applications has also been limited by its intrinsic brittleness. There is continued interest in exploring the possibility of overcoming the mechanical limitations of HA using techniques such as synthesis of graphene-reinforced hydroxyapatite nanocomposites.

Another material with promising potential in biomedical applications is graphene, which has competitive mechanical and thermoelectric properties and a large specific surface area. As a result, graphene has found use in electrochemical sensors, [75], superabsorbents [76],

and interfacial catalysis [77]. Furthermore, graphene has increasingly become one of the most common materials used in modern energy technology [78] and has also found use as a reinforcement in composites, especially those using metals and polymers, as well as ceramics. Specific biomedical applications include the use of graphene as part of the materials in the design and manufacture of biomedical technologies like drug delivery and neural regeneration [79]. It is also a common component in bioimaging and bone tissue engineering applications [80].

Using spark plasma sintering, Liu et al. [81] explored the modulus, toughness, and related biological properties of composites with differing amounts of graphene by characterizing a hydroxyapatite–reduced graphene oxide (HA/rGO) composite. Li et al. [82] reported improved cytocompatibility in composites which had been enhanced or modified using graphene oxide. Zhao et al. explored and reported the effects of graphene nanostructures on the mechanical and biological properties and the biocompatibility of composites [83, 84, 85].

Implants in the human body are subjected to a variety of extracellular bodily fluids, which have chloride ions at concentrations sufficient to corrode any metallic materials they come into contact with [86]. This is the primary reason why corrosion resistance is a priority consideration in selecting materials for human body implants. Furthermore, bodily fluids contain substantial levels of amino acids and proteins, which are well-documented to quickly corrode metallic implants in the body [87, 88]. However, the effect of changes in body pH has been shown to be negligible. For example, when the pH decreased to 5.2 in hard tissues after implantation, the corrosive effect decreased because tissues recorded pH

values as high as 7.4 within few weeks [89].

However, regardless of the extent of corrosion caused by bodily fluids on metallic implants, it is important to note that corroded materials are a common cause of allergic reactions following an implant procedure. They can also lead to the release of metallic ions into bodily fluids, thus increasing the risk of inflammatory reactions. Overall, the need for having materials with high corrosion resistance in the design and manufacture of implants cannot be overemphasized. Due to the shortcomings in the corrosion resistance of most of the common biomaterials, palladium has been identified as a potential alternative to address the corrosion of biomaterials. In particular, this material is lauded for its excellent corrosion resistance rating in moist air, but more importantly, it has been found to have fewer risks to the human body compared with other biomaterials such as nickel and silver [90]. As such, the use of palladium can be an excellent choice for modifying surfaces of metallic implants to enhance their corrosion resistance.

Jiang et al. [91] showed that the presence of self-assembled monolayers (SAMs) on Pd enhanced its resistance to nonspecific adsorption of proteins, which can compromise adhesion efficacy in mammalian cells. Using ellipsometry and surface plasmon resonance spectroscopy, adsorption of any form of proteins in bovine serum was significantly inhibited by these SAMs. In addition, there is evidence that Pd(II) compounds are highly cytotoxic to a variety of cell lines [92-94], implying the potential value of Pd in enhancing the antibacterial activity of implants in the human body [95]. In particular, Pd(II) complexes exhibit excellent activity in fighting bacterial strains, and their antibacterial effects have been equated to that of standard drugs [96]. Polívková et al. [97] found that

increasing the thickness of the palladium film layer in biomaterials greatly improved the antibacterial effect of the materials relative to those with thin Pd film layers. Anselme et al. [98] used surface engineering to show that coating biomaterial with a nanometric gold-palladium film significantly improved the adhesion of the long-term osteoblast. This suggested that a gold-palladium film could improve both cell and tissue adhesion, especially in biomaterials with low inherent biocompatibility, including polished stainless steel and other metallic substrates [99].

2.4 Wear-In Biomedical Alloys

The loosening of joint placements is one of the biggest challenges in biomaterials, and it is estimated that this is the cause for revision surgery in 10–20 percent of patients with a metal head and polymer cup type total joint replacements [100–102]. This is a major concern given the number of people who undergo total joint replacements in the United States every year [103]. The longevity of replacement implants is increasingly becoming a major R&D interest as the number of youths in modern society diagnosed with osteoarthritis continues to increase. Thus, measures to improve the fixation and resistance to wear of replacement implants continue to be a priority focus of orthopedic research. The main reason for the failure of most implants is their corrosion and releasing of wear debris into the surrounding body tissues which prompt bone resorption, followed by the loosening of the implant as shown in Figure 2.3.

In addition to the cost and high risk of failure of revision surgeries, poor wear resistance properties of implants commonly expose the human body to toxic foreign particles, such as cement particles due to bone resorption of wear debris into the bodily fluids. Post-

mortem studies on patients who had received replacement implants have consistently and commonly shown the accumulation of wear debris, especially from the surface coatings of implants in the liver, as well as in the spleen or abdominal lymph nodes. The lack of wear resistance is a particular issue for implant replacements involving high-impact joints which are prone to dynamic load-bearing on a day-to-day base, such as knees and hips. The dynamic load-bearing, the functioning of these body joints implies that the implants are constantly subjected to high and dynamic frictional forces. For knee joints, implant materials usually have coefficients of friction ranging from 0.16 to 0.05. This variation is mainly due to differences in the materials that are in contact with the body and the type of testing lubricant used to determine the coefficients.

For hip joint replacements, implants include femoral head and ultra-high-molecular-weight polyethylene (UHMWPE) acetabular cup, and the femoral head ideally articulates against the UHMWPE acetabular cup. Based on numerous studies investigating the risk of failure of these implants due to aseptic loosening, femoral heads made from titanium alloys showed the greatest wear (at 74.3%) when compared with the UHMWPE acetabular cup component of the composite system. Femoral heads made from Co–Cr alloys showed less wear, while the wear resistance of stainless steel was found to be between those of Co–Cr and Ti alloys. This is complemented by the fact that higher levels of metallic particles accumulated on tissues surrounding the Ti alloy prostheses. Levels of wear debris were found to be the lowest on tissues surrounding the Co-Cr alloy and SS prostheses [104]. In a move to mitigate this wear-related problem and the risks associated with revision surgery, numerous efforts have been made to facilitate R&D focused on replacing the polymeric

material used in the cup with a metal or ceramic as a more reliable option for long-term fixation.

Of particular significance, replacing the cup material with metal is based on results that show that metal-to-metal prostheses can reduce the production of wear debris in hip replacements by 20–100 times in terms of volume compared with metal-to-polymer prostheses [105]. Furthermore, it has been established that metal debris has a lower risk of causing inflammatory reactions compared with UHMWPE debris [106]. Nevertheless, the perceived benefits of using a metal cup are limited by the fact that metal-to-metal prostheses have demonstrated higher frictional torques compared with metal-to-polymer prostheses [107]. There are also concerns over the so-claimed low wear volumes produced by the long-term presence of metal-on-metal prostheses in the body. Based on studies of *in vivo* and *in vitro* implants, it has been consistently shown that Co-Cr alloy particles have toxic effects on different body cells and tissues. Historical concerns over the wear problems of polymer-on-metal, and ceramic-on-ceramic (alumina) were voiced 20 years ago when it was noted they exhibited lower levels of wear compared with Co-Cr alloys, metal-on-polymer, and metal-on-metal.

However, the practical relevance of ceramic-to-ceramic implants has been lost by concern over the high risk of fracture of these implants and the health implications of the release of debris. In addition, however, when tested for its cytocompatibility, the toxicity of CoCr wear particles at the nanometer scale showed high toxicity compared with ceramic wear debris from an alumina implant [108]. Another common material used in making ceramic implants is zirconia, which is generally considered to have better biomechanical properties

compared with alumina, especially in relation to brittleness. Zirconia exhibits high crack propagation resistance and low levels of brittleness. Indeed, it is due to these properties that this ceramic material continues to command a significant share of the total number of replacement implants in society, with 6,00,000 zirconia head implants having been fixed, especially in the US and Europe. However, cases of early implant failure have been documented in the use of zirconia. These claims are, however, difficult to verify given the fact that the implantation of zirconia implants includes various techniques, and the effect of individual methods on the microstructure of the implant, and hence the mechanical properties, cannot be ignored.

There is a growing trend towards developing alumina-zirconia composites to exploit the toughness of alumina and the high crack propagation resistance and low levels of the brittleness of zirconia. Out of the various combinations that have been tested to date, a ratio of 4:1 for zirconia and alumina, respectively, and maintaining high bending strength (2000 MPa) has shown great promise. The same results have been found using a combination ratio of 3:1 for alumina and zirconia, respectively while controlling for high strength (1150 MPa) and toughness (8.5 $MPa.m^{1/2}$). Despite this success, however, the effectiveness of a new implant can only be quantified based on its effect on patients after long-term implantation. As a result, more research is needed before these implants can be commissioned for widespread application. There are also notable interests in the development of ceramic composites with low coefficients of friction and high wear rate resistance [109].

In addition to the challenge of material selection, implant surgery is also faced with the

challenge of *in vitro* tests on the wear resistance properties of materials. Of particular significance here, there remain wide variations between the wear rates determined *in vivo* (1–5 mm^3 per annum) and *in vitro* (0.01–0.1 mm^3 /million cycles) [110]. Various factors have been associated with causing or contributing to these differences, including differences in the type of lubrication used and kind of motion of concern to the mating pair. More importantly, the angle of inclination of the acetabular cup has been blamed for being a risk factor to the observed differences, and movements by patients involving very limited separation between the head and the cup during the swing phase of walking. When micro separation is introduced in *in-vitro* wear tests, it was shown that the wear rates observed clinically on *in vivo* tests could be observed *in-vitro* as well. By introducing harsh environments to induce the micro separation for *in-vitro* to wear testing of the ceramic-on-ceramic implants, Tipper et al. showed that these implants had very low wear rates relative to metal-to-polymer implants. Other studies have investigated the absence of lubrication for *in vivo* wear testing [111,112–114].

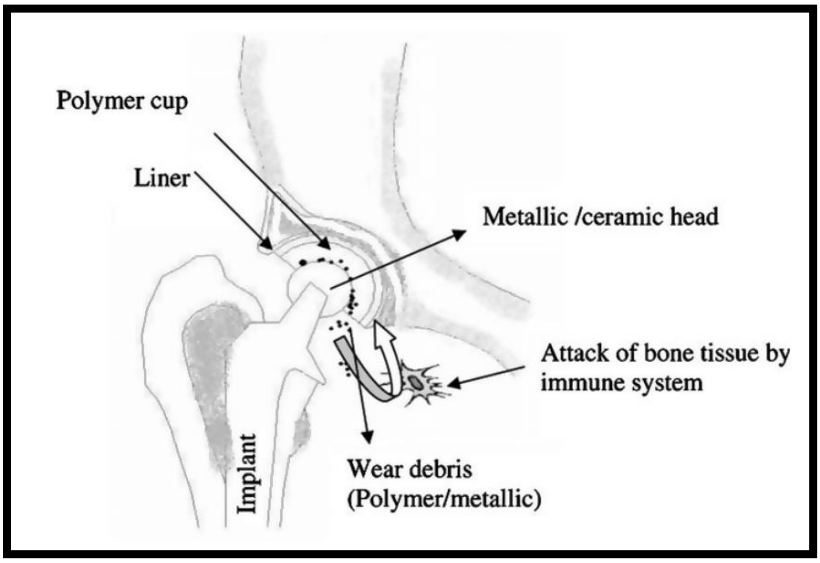

Figure 2.3. Wear of implant [113].

2.5 Corrosion Behavior of Biomedical Titanium Alloys

Regardless of the type of the metal or metal alloy, all metal-related materials are subject to some level of corrosion within the human body due to the inherently high presence of chloride ions, amino acids, and proteins in almost all bodily fluids. Once in the body, there are various chemical reactions that can occur on an implant. In particular, the metallic components of the alloy are subject to oxidation which then releases oxygen and forms their ionic components. The oxygen is dissolved into the bodily fluid where it is reduced to produce hydroxide ions. Although different forms of corrosion have been documented, it has been reported that the rate of corrosion is generally low due to the presence of passive surface films in most metal alloy implants in use. 316L stainless steel and other passive alloys in the presence of chlorides have been shown to suffer from high corrosive damage due to crevice attack or corrosion of shielded sites such as the screw-plate interface, as well

as corrosion under the washers. In practice, however, mechanically-assisted crevice corrosion has also been shown to exist and is mainly observed on modular total hip arthroplasty components and has been blamed on serum cobalt and urine chromium [114].

Another common problem is pitting corrosion, especially for 304 SS implants, which is mainly documented for implants of the oral cavity. This can be explained by the high levels of oxygen and acidic foodstuffs within oral cavity environments. In practice, this problem has been overcome by incorporating ultra-high clean grades such as 316LVM and nitrogen additions on the surface of the implants. On cobalt-based alloys, pitting corrosion has been associated with the release of carcinogens into the body [115–117]. Despite that titanium and its alloys are lauded for their high resistance to pitting corrosion under a variety of *in vivo* conditions, they are generally highly susceptible to corrosion in the presence of high fluoride solutions such as those involved in conventional dental cleaning procedures [118]. More commonly, fatigue corrosion occurs, which is generally associated with the majority of medical implants being exposed to low-frequency loads. As such, they are highly vulnerable to corrosion fatigue due to these poor levels of load frequency. For Ti, resistance to fatigue corrosion has been shown to be independent of the pH value to a larger extent. For stainless steel, however, fatigue corrosion resistance has been found to decline significantly at body pH levels below 4. Yu et al. suggested that pitting corrosion is a risk factor for the initiation of corrosion fatigue in stainless steel [119]. In particular, these authors reported a general improvement in the corrosion fatigue resistance properties when implants were treated through nitrogen implantation and heat treatment procedures, especially for a Ti64 alloy. The study found a direct relationship between the level of

resistance to corrosion fatigue and the size of plates, where large plates were more resistant than smaller ones. On a comparative basis, Ti64 has been shown to possess better resistance to corrosion fatigue compared with 316L SS alloys.

Fretting corrosion, on the other hand, is a form of corrosion that is predominant in all load-bearing metallic orthopedic implants that mainly occurs at the bone-stems interface or at the stem-cement interface. It is also common at the interfaces of modular connections between implant components and has been closely linked to the generation of both ionic and particulate wear debris into the surrounding bone tissues. This leads to continued fracturing and abrasion of the metal oxide protective layers, and hence continued deposition of wear debris into the surrounding tissues. As a result, fretting is a major clinical concern for the long-term use of implants. This can be explained by the fact there are several known potential toxins that have been associated with wear debris in bodily tissues, including the association of wear debris with inflammatory and/or allergic reactions. In total hip implants, despite the presence of a perfect interlocking mechanism between the head and stem, it is not uncommon for body fluids to penetrate the junction, which risks fretting corrosion. Cabrera and Mott [120] showed that fretting corrosion can be significantly reduced by pre-treating implants to form a protective oxide layer on the surface.

2.6 Surface Modification of Titanium Alloys for Biomedical Applications

2.6.1 Coatings for enhanced wear and corrosion resistance

One of the main obstacles to the long-term performance of surgical implants is the limitations posed by their surface properties. For example, the poor tribological properties

of titanium and its alloys negatively impact the durability of the resulting implants upon fixation. This includes poor resistance to wear which implies the vulnerability of the implants or the joints to loosening due to wear, and hence reducing the service life of the implants. A general measure to overcome this problem is coating the implant surface with a suitable material. In addition, surface engineering has also proven to be a promising solution to extend the service life, and hence the performance of orthopedic devices made of titanium and its related alloys. There are numerous surface treatment techniques that have been used to address the tribological properties of titanium and its alloys, including surface modification techniques such as dipping, spraying, electron-beams, and pulsed lasers, as well as chemical surface treatments [121, 122, 123]. Other techniques include carburization and boriding which have been used to improve the hardness of the surface of titanium alloys.

However, the physical deposition techniques are prone to interfacial separation, especially when subjected to repeated loading, and chemical methods suffer from requiring high temperatures and the associated risk of causing torsional or twist of the substrate. It has been shown that TiN-coated hip and knee implants have high wear resistance and extended compatibility [124]. In addition, *in vitro* studies by Sundarajan et al. reported that nitrogen ion-implanted Ti-Modified 316SS display excellent corrosion resistance characteristics when implanted with a dose of 11 017 ions/cm^2 [125]. The use of surface hardening methods such as PVD, CVD, or plasma nitriding and ion nitriding to form TiN may lead to the formation of various non-stoichiometric compounds with a high hardness on the surface [126, 127]. Although the corrosion resistance of ion-implanted surfaces is generally

very high, the layer of the ion implants has been shown to wear off with time [128]. This problem associated with nitriding is usually overcome by using high-energy electron-beam irradiation which enhances the hardness and wear-resistance by promoting the development of Ti-based surface composites [129]. The use of oxygen diffusion hardening (ODH) has also been shown to help improve the resistance of Ti alloys to abrasion wear.

2.6.2 Coatings for high osseointegration

In its most basic form, osseointegration can be defined as the process through which the bone heals after an implant. On the other hand, it is the primary goal of the implant surgery that this healing process will involve the successful formation of a new bone, and the process involves the initial adsorption of water molecules and proteins as its first step. This is followed by one of three possible processes:

- The adsorption of water molecules and proteins may lead to the formation of new bone cells around the implant joint or surface, followed by proliferation and differentiation of the cells and osseointegration. This sequence of events is indicative of the acceptance of the implant by the body.
- The human body might prompt an inflammatory response, an indication that the implant has been rejected.
- Micromotions of the implant can also occur, prompting fibrous tissue to form on the surface of the bone, as opposed to forming a bone-implant interface. The end effect of this is the inhibition of osseointegration.

The surface properties of the implant are the main factor of concern in determining the

process that will occur because these properties define the surface energy, the bone-implant reaction, and the integration process [130]. Details on the classification of the different biomaterials and associated tissue responses are shown in Table 2.1. In general, the success of implant surgery in orthopedic and trauma surgeries remains subject to the integration of the implant and the adjacent bones and tissues. A higher degree of osseointegration implies a higher level of mechanical stability of the bone-implant interface, and hence a reduction in the risk of failure. This can only be achieved if there is no fibrin adhesion and micromotions and blood vessels are not allowed to grow.

On one hand, the fundamental consideration in enhancing cell adhesion and mitigating micromotions is to ensure that the surface of the implant is tailored appropriately to fit with the bone and surrounding tissues. This dictates informed consideration of the surface chemistry, but more importantly, the topographies of the surface at the nanometer and micrometer scales. There are many strategies currently being examined to enhance the chances of bone integration with titanium-based implant biomaterials. In these strategies, surface roughness has a direct influence on cell morphology and growth, while changes in the topography of the surface are associated with altering the orientation and attachment of the cells [131,132, 133].

Numerous methodologies are available to increase the likelihood of biomechanical compatibility, including securing porous and coating surfaces with nano-ceramic particles, HAP, and oxides. Surface grit blasting and surface polishing enhances the growth of cells and increases the interlocking surface area to improve implant fixation [134,135–138]. More importantly, this type of surface treatment also improves the thickness of the oxide,

which in turn implies an improvement in the biocompatibility of titanium implants because of the general association of such properties with the thickness of oxide on the surface. Heat treating of biomaterials in oxygen or air appropriately enhances their biocompatibility by changing the oxygen composition in the biomaterial, especially on the surface. MacDonald et al. found heat-treating biomaterials at low temperatures to be effective in enriching the surface with Ti and Al, and hence enhancing cell attachment [139].

Moreover, bone integration has also been found to be significantly influenced by the waviness and porosity of the implant. In-growth of bone into a porous surface enhances interlocking of the implant with surrounding bone tissue, and hence improves the biomechanical compatibility and fatigue loading resistance [140–142]. There is also the practice of remodeling bone on a porous surface. In particular, available literature shows that porous-coated anatomic femoral components are more reliable and have a lower risk of failure due to loosening or osteolysis in the long-term than cemented stems [143]. In a study by Zinger et al., it was established that cavities of the same size or larger than the cell on the implant surface-enhanced cell attachment [144,145]. Wennberg et al. suggested that a grooved surface of 11.6 lm average wavelength and 1.4 lm provided an optimal implant surface for assured integration [146]. In addition, based on rat models, it was found that bone remodeling is more effective when using implants with more porous surfaces [147]. In their study, Hulbert et al. found a direct relationship between porous surfaces and increased osteons. Li et al. suggested 140 lm pore size as the best pore size for optimal bone growth [149], however, Gotz et al. claimed that the presence of different pore sizes on the surface was the best for enhancing bone remodeling [150].

However, Gotz et al. also found that the bone growth rate on 300 lm pores was significantly slower compared with the rate on a surface with 200 lm pores. This finding suggests differences between the rate of osseointegration and the size of pores on the surface. Accordingly, available literature reports seem to suggest that the best size of surface pores for optimal bone remodeling should be within the range of 100–200 lm. The use of porous biomaterials is expected to enhance osseointegration, and hence the prospects of long-term fixation of implants. Porous biomaterials are also helping to improve the modulus of implants, and hence their ability to overcome the stress shielding effect. Vamsi et al. found that varying the porosity can enhance the modulus of biomaterials by simply determining the number and sizes of pores necessary to achieve modulus value for a specific implantation scenario [151].

Based on the above reasons, the idea behind enhancing bone-implant integration is rooted in securing implant surfaces which are as close to the surface of the bone as possible, which continues to be a major challenge in the field of biomaterials. Furthermore, securing alloys that will guarantee chemical bonding between implants and bones is a major problem that must be solved to define the future prospects of biomaterials used to restore and/or enhance the quality of life of humans. At the core of the problem, there is a need to secure implants with a sufficiently thick layer of biocompatible calcium phosphate on the surface, which is currently accomplished by using dipping, spraying, electron-beam, and pulsed laser to deposit biocompatible calcium phosphate on the surface [152]. Synthetic hydroxyapatite is one of the biocompatible calcium phosphate constituents currently in use. Surface coatings with this material have been found to significantly enhance osteoconductivity [153–156].

In addition, these coatings have been linked with enhancing early fixation and associated bone-implant integration regardless of shortcomings in the biomechanical compatibility of the implant [157,158]. Using a micro-arc oxidation treatment to modify the surface of titanium implants has been shown to greatly improve osseointegration.

Improved osseointegration of treated titanium implants was associated with the effect of the treatment process in incorporating Ca and P in the surface to form a rough porous oxide layer. The activity of alkaline phosphate (ALP) has been shown to be directly related to the thickness of both the oxide and Ca and phosphor layers on the surface of the implant [159]. To enhance the deposition efficiency of Ca and phosphor layers, a variety of chemical methods are currently under investigation since chemical methods are more economical and provide a more efficient coating of implants with complex shapes. A method designed by Li et al. has been shown to enhance the osseointegration of materials that have been highly oxidized [160]. This was achieved by the initial heat treating of the alloys at low temperatures before treating them in an alkaline medium using a method devised by Kim et al. [161]. Following the alkaline treatment, the implant was immersed in protein-free body fluid mimicking the human body fluid for two weeks. This enhanced the thickness of the oxide layer while the alkali layer enhanced the formation of Ca-P on the surface. This method has been shown to greatly improve the wear resistance properties of implants by providing an oxide layer and enhancing bio-conductivity due to the alkali treatment.

In addition, there is ongoing research on the possible development of nano-surface topographies due to the general understanding that nano-surfaces closely mimic bones in the human body. In a study by Thomas et al., it was suggested that the possible use of

carbon fibers with nanometer dimensions in creating a novel surface topography to enhance the osteoblast adhesion properties of implants [162] by providing nanometer surface roughness properties. However, although nanocrystalline titanium surfaces have been found to improve cell growth and wear resistance, the effect of this corrosion resistance and the electrochemical behavior of these implants are yet to be investigated [163]. Studies on the cell compatibility of nano-sized ceramic particles have, however, been sown to improve osteoblast adhesion, and hence enhance Ca deposition [164]. Furthermore, wear debris from nanophase ceramics such as alumina and titania are less harmful to bone cells relative to wear particles from conventional ceramics [165]. This implies the great potential that nanotechnology promises in enhancing the biocompatibility and biomechanical compatibility of biomaterials.

2.7 Biocompatibility of Titanium and its Alloys

Upon implantation of artificial implants *in vivo*, there are numerous cascade reactions that take place within the human body when the implanted biomaterial starts interacting with body fluids, amino acids, and proteins as well as body tissues and cells in general [166].

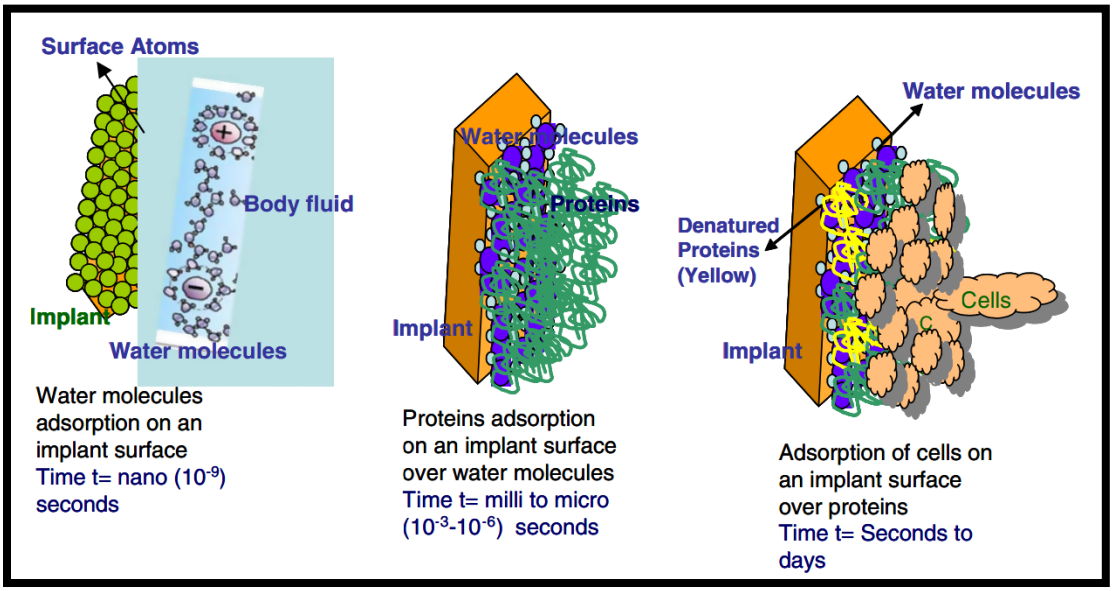

Figure 2.4. Various reactions occurring during cell attachment and the response of the human bone to an implant at different time intervals [167].

However, it is worth noting that the human body, particularly the bone response to an implant in different ways at different times. This results in different reactions on the surface of the bone as shown in Fig. 2.4. In general, this sequence of localized body responses to the implant or foreign materials in the body prompts the typical foreign body response mechanism, and which commonly prompts the formation of fibrous tissue capsule around the implant. One of the main factors behind this unfavorable body-implant reaction is the nature of the surface of the biomaterial used since the surface of a biomaterial is the first area of contact with the body. As a result, the nature of the contact surface determines the healing process following implantation, as well as the long-term integration of the implant into the body. This underpins the importance of both the chemical composition and

topology of the surface of the biomaterial in securing successful and long-lasting implantation by influencing the nature of the bone-implant interface. Regardless of the quality, however, no implant can be assumed to be completely free from adverse effects [167-170].

Chapter 3 : Methodology

3.1 Experimental Details

3.1.1 Materials

The stainless steel 304 (SST 304) and pure zirconium foils used in this project were purchased from Alfa Aesar (Korea). The chemical composition (wt %) of stainless steel 304 is 70% Fe, 19% Cr, and 11% Ni. Calcium chloride dihydrate ($CaCl_2 \cdot 2H_2O$, ≥99%), sodium chloride (NaCl, ≥99.5%), ammonium dihydrogen phosphate ($NH_4H_2PO_4$, 99.999%), sodium phosphate monobasic monohydrate ($NaH_2PO_4 \cdot H_2O$, ≥98%), and sodium phosphate dibasic (Na_2HPO_4) were all obtained from Sigma-Aldrich, while the graphite powder was purchased from Sinopharm Chemical Reagent Co. Ltd. Sodium hydroxide powder (NaOH) was purchased from Daejung Chemical Co. (Korea). Palladium-(II) nitrate hydrate ($Pd(NO_3)_2 \cdot xH_2O$, 99.8%) was purchased from Alfa Aesar. Distilled water was used to prepare all aqueous solutions.

3.2. Preparation of materials

3.2.1 Preparation of SST 304

SiC sandpapers (800-2000 grit) were used to polish SST 304 samples (with dimensions of 32 mm × 8 mm × 0.2 mm). Then, the samples were cleaned with acetone in an ultrasonic bath and rinsed with distilled water prior to electrodeposition. Afterward, the SST 304 substrates were etched by submerging them in an H_2SO_4 solution for 5 minutes.

3.2.2 Preparation of pure zirconium substrate

Commercially-available zirconium substrates (99.5% purity, Alfa Aesar, Heysham, England) with dimensions of 40×10×0.127 mm^3 were used as substrates for

electrodeposition. The zirconium foil surface was ground and polished with silicon carbide sandpapers (grit range of 800-1500) and etched in an HF solution (48%) for 1 h. Then, it was ultrasonically (Daihan Ultrasonic Bath Set WUC-A02H) cleaned in ethyl alcohol, acetone, and deionized water for 15 min, and lastly dried in a vacuum oven at 70 °C. To avoid an edge effect during electrochemical deposition (ECD), the zirconium substrates' edges were rounded.

3.2.3 GO fabrication

The Hummers' method was used to prepare graphene oxide (GO) by oxidizing natural graphite powder [171]. Graphite powder (10 g) was added to concentrated H_2SO_4 (230 ml) in an ice bath with stirring. $KMnO_4$ (40 g) was added slowly under strong agitation to prevent the suspension temperature from exceeding 20 ^oC. The reaction was then transferred to a 40 ℃ oil bath and vigorously stirred for approximately 30 minutes, after which time 150 ml distilled water was added to the solution, and the mixture was stirred for an additional 15 minutes at 95 °C. More deionized water (500 ml) was added to the mixture, followed by 15 ml H_2O_2 (5% solution), after which the solution turned yellow. To remove metal ions, the solution was filtered and HCl (1:10, 250 ml) was used to wash the solution. Then, the filtered product was dried and diluted to 600 ml to obtain an aqueous graphite oxide dispersion. To eliminate residual metal species, the solution was purified for one week using a dialysis membrane (molecular weight cut-off of 8,000−14,000 g/mol). The diluted graphite oxide aqueous dispersion (1.2 L) was stirred for 12 hours and then sonicated for 30 min to exfoliate it and obtain GO. Finally, to remove any un-exfoliated graphite, the GO dispersion was centrifuged (Avanti HP-301, Beckman Coulter, USA) at

12 000 rpm for 40 min.

The graphene oxide dispersion (20 ml) was mixed thoroughly with 100 ml deionized water. To stabilize the suspension and ensure that graphene oxide was well-dispersed in ultrapure water, the dispersion was subjected to ultrasonication at 570 W for 2 h, to finally obtain a transparent golden GO suspension.

3.2.4 Preparation of hydroxyapatite solution

First, 2.45 g $CaCl_2$ (Sigma-Aldrich, 223506-500G ACS reagent, ≥99%) and 0.58 g NaCl (Sigma-Aldrich Company, S7653-250G BioXtra, ≥99.5%) were added into 50 ml of distilled water and mixed using a magnetic stirrer (Daihan MSH-20D). Then, 1.150 g $NaH_2H_2PO_4$ (Sigma-Aldrich, 255793-10G 99.5% trace metals basis) and 50 ml of distilled water were separately mixed by a magnetic stirrer. Then, the two solutions were mixed and stirred to obtain the hydroxyapatite solution.

3.2.5 Preparation of HA/GO/Pd Electrolyte

$CaCl_2$ (0.167 mol L^{-1}), 0.1 mol L^{-1} $NH_4H_2PO_4$ with a Ca/P ratio of 1.67 were dissolved in 100 ml distilled water to prepare the electrolyte, and a NaCl solution (0.1 mol L^{-1}) was also added to the electrolyte to improve the conductivity. Later, 20 ml of an aqueous suspension of GO and 25 ml of an aqueous suspension of $Pd(NO_3)_2 \cdot xH_2O$ (0.001 mol L^{-1}) were added. A NaOH solution was used to adjust the pH of the electrolyte to 6.

3.2.6 Preparation of HA/GO/Pt Electrolyte

To prepare 0.001 mol/L Pt solution, 0.01 g K_2PtCl_4 powder was added to 25 ml distilled water in an opaque flask to obtain a 0.001 mol/L Pt solution. 40 ml hydroxyapatite,

40 ml graphene oxide, and 25 ml Pt solutions were mixed and stirred for 15 min. Then, the pH of the resulting solution was adjusted to 6 using 1 M NaOH in a water-bath at 80 °C.

3.2.7 Deposition Parameters for HA/GO/Pd

Figure 3.1 and Figure 3.2 show the electrochemical workstation equipped with a typical three-cell system that was used to perform deposition (PARSTAT 3000A, Princeton Applied Research). The working electrode consisted of polished and etched SST 304 sheets, while the platinum wire was used as the counter electrode, and silver chloride (Ag-AgCl) was used as the reference electrode. Chronoamperometry was used to perform the deposition whose process parameters were as follows: a constant voltage of -2 V vs. Ag-AgCl; an electrolyte temperature of 80 °C; a distance between the working electrode and the counter electrode of 2 cm; and a deposition time of 1500 s. Magnetic stirring was conducted at 115 rpm was used to ensure particles were homogeneously dispersed for the entire electrodeposition process. Finally, coated samples were carefully rinsed with water and dried in an oven at 60 °C.

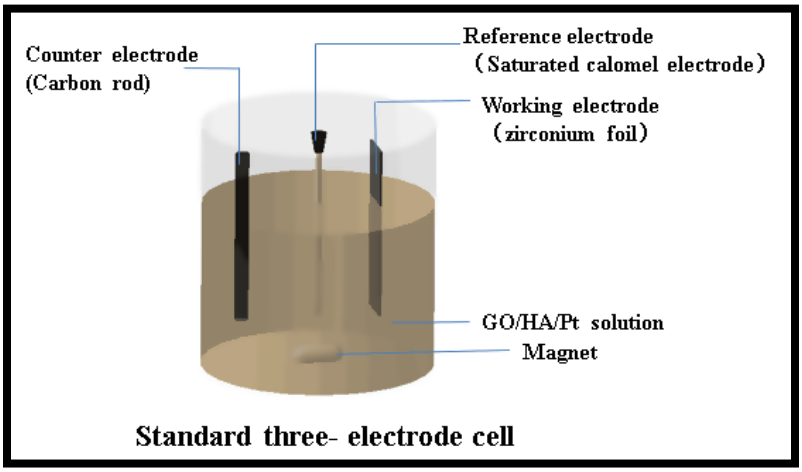

Figure 3.1. Schematic of 3-electrode cell

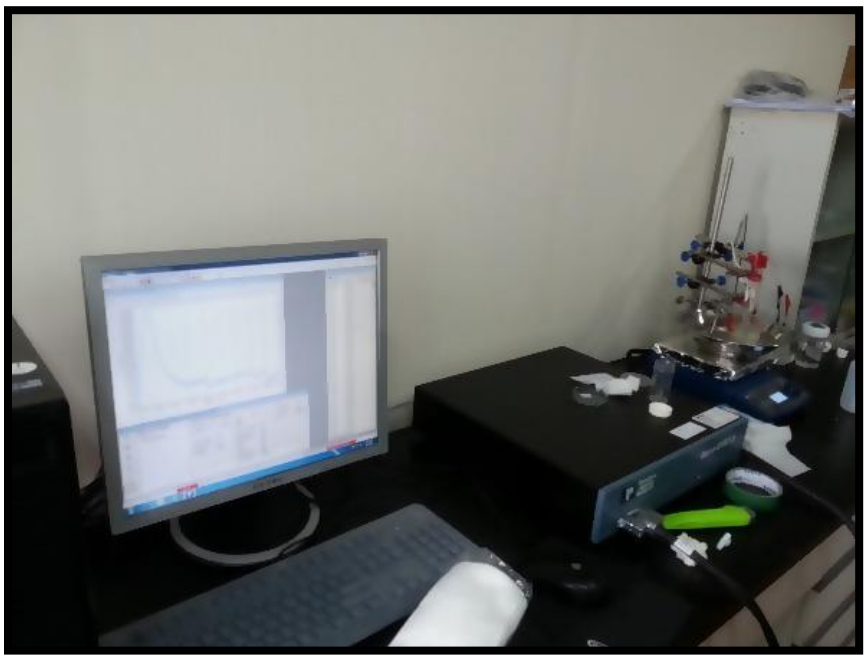

Figure 3.2. Electrodeposition workstation

3.2.8 Deposition Parameters for HA/GO/Pt

The electrodeposition (Potentiostat/Galvanostat/Impedance Analyzer, PARSTAT300) was performed in a standard three-electrode cell using a chronoamperometry cycle in which pure zirconium foil, a graphite rod, and a saturated calomel electrode SCE were the working electrode, counter electrode, and reference electrode, respectively. The electrolyte was stirred at 70 rpm during electrodeposition, and the applied potential was kept at −2 V for 7200 s (time per point was 2 s with 3600 total points). Finally, the electrodeposited samples were washed with deionized water and dried in an oven at 60 °C (Jeio Tech VO-10X).

3.3 Thermal Treatment of HA/rGO/Pd and HA/rGO/Pt Coating

The tube furnace shown in Figure 3.3 was used to perform thermal treatment at four annealing temperatures: 200, 300, 400, and 600 °C. The chamber was firstly pumped to $<1.0 \times 10^{-3}$ torr and then Ar (200 sccm) was used throughout the whole process. A heating rate of 5 °C min^{-1} was used to reach the target temperature, where the specimens were held for 1 hour (Figure 3.4). Finally, the samples were cooled naturally by leaving them on the surface.

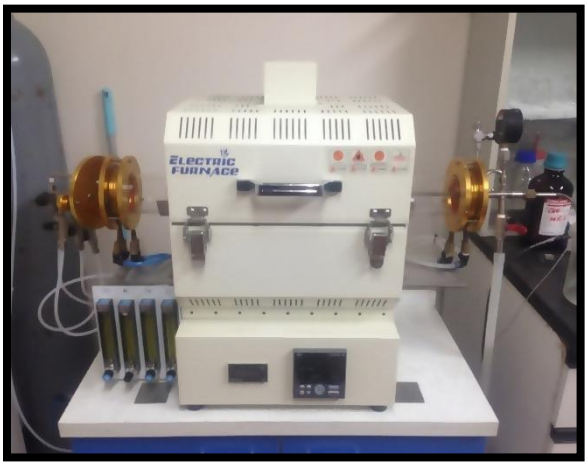

Figure 3.3. Tube furnace

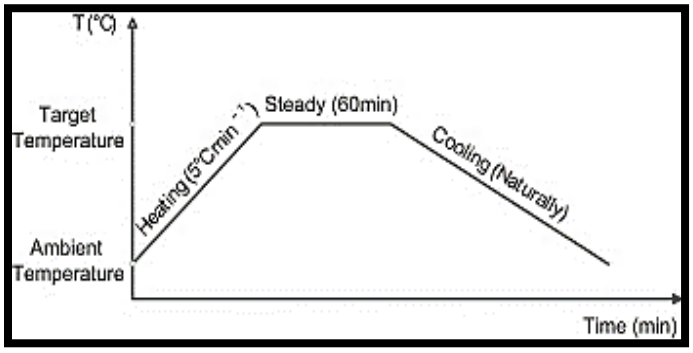

Figure 3.4. Heating and cooling process

3.4 Characterization

Field-emission scanning electron microscopy (FESEM) was used to examine the surface morphology of electrodeposited coatings using an FEI Nova NanoSEM 450 (FEI, USA) at a 15 kV acceleration voltage (Figure 3.5). The elemental composition and morphology of samples were examined by transmission electron microscopy (JEM-2010 TEM, JEOL,

Japan) (Figure 3.6). The elemental composition of the coated samples was studied using energy-dispersive X-ray spectroscopy (EDS). X-ray diffraction (XRD) spectra were measured using the scan-step technique (2θ = 5–90), with a step width of 0.02 and an exposure time of 50 s per step using a high-resolution XRD (HR-XRD, Figure 3.7) instrument (Smart Lab, Rigaku). EVA V.9.0 software was used to perform phase analysis. Functional groups present in the coated samples were identified by Fourier-transform infrared spectroscopy (FTIR, Figure 3.8), using KBr pellets in a Nicolet iS50 FT-IR Spectrometer (Nicolet, USA) with a 450–4000 cm^{-1} scan range and a 0.5 cm^{-1} spectral resolution.

Figure 3.5. FESEM

Figure 3.6. TEM

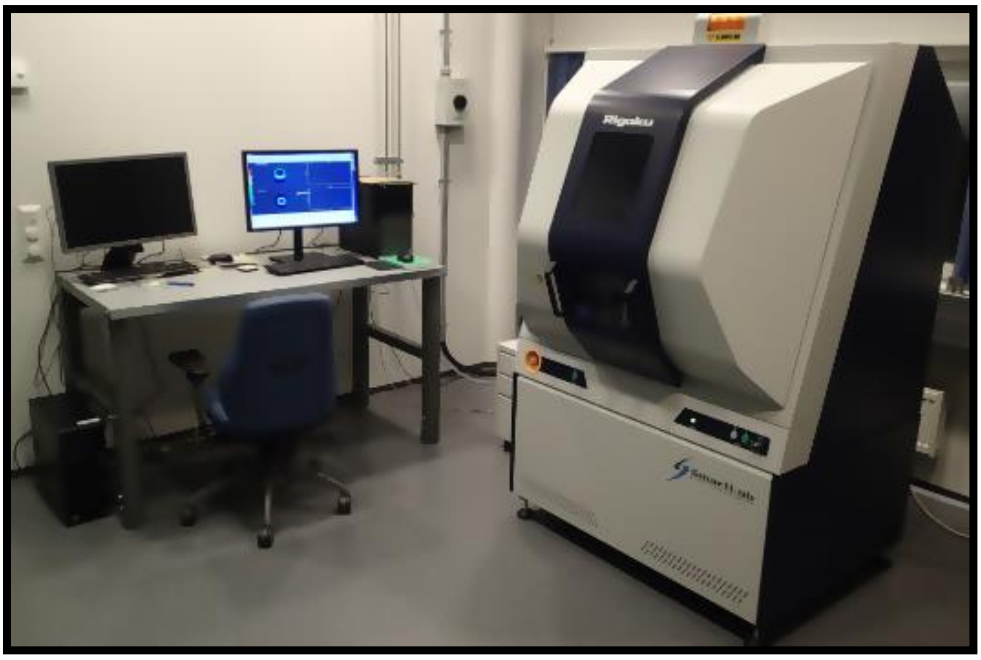

Figure 3.7. XRD

Figure 3.8. FTIR

3.5 Biocompatibility Tests

The biocompatibilities of uncoated SST 304 and pure zirconium, with different coatings including HA, HA/rGO, HA/rGO/Pd, and HA/rGO/Pt were investigated using the human cell line MDA-MB-231 equipped with a green fluorescent protein (GFP) to identify the presence of living cells. This method served to evaluate the surfaces' ability to support cell attachment and permit the growth and proliferation of cells. Dulbecco's Modified Eagle's Medium (DMEM) solution (Sigma-Aldrich), complemented with Newborn Calf Serum (NBCS) (Life Technologies, Thermo Fisher Scientific), 100 U mL^{-1} penicillin and 100 µg ml^{-1} streptomycin at 37 °C in a CO_2 incubator with a CO_2 concentration of 5% was used to grow the cells. A Nikon Eclipse Ti-E inverted fluorescence microscope (Nikon, Japan) was used to perform 1-day post-culture proliferation tests.

3.6 Electrochemical Tests for HA/GO/Pd

The anticorrosive characteristics of the coatings were evaluated via anodic polarization experiments conducted in $CaCl_2$ with a PARSTAT 3000A electrochemical workstation. Synthetic serum with the chemical composition listed in Table 3.1 was the medium in which all electrochemical tests were performed. The counter, working, and reference electrodes were a platinum wire, SST 304 samples, and a saturated calomel electrode (SCE), respectively. Samples were immersed in synthetic serum for 2 days to stabilize prior to testing. A 0.167 mV/s scan rate in a potential range between -0.25 and 0.25 V was used throughout all electrochemical measurements.

Table 3.1: The chemical composition of synthetic serum

Chemical compound	Concentration, g/dm^3
$CaCl_2$	1
Na_2HPO_4	22.98
NaH_2PO_4	13.78

R_p is the polarization resistance calculated using the following formula [172]:

$$Icorr = \frac{\beta}{Rp}$$

where β is a constant determined by the following equation:

$$\beta = \frac{\beta c \times \beta a}{2.3(\beta c + \beta a)}$$

where β_c and β_a are the Tafel slopes.

P.E. was also calculated to assess the effectiveness of corrosion protection using the following formula [173],

$$P.E.(\%) = \frac{Icorr^0 - Icorr^c}{Icorr^0}$$

where $I_{corr}{}^0$ and $I_{corr}{}^c$ are the corrosion currents of the SST 304 in the absence and presence of thin-film layers, respectively.

3.7 Electrochemical corrosion test for HA/GO Pt

The electrochemical behavior of the uncoated, HA-, rGO-, HA/rGO-, and HA/rGO/Pt-coated samples was studied in a $CaCl_2$ solution. A conventional three-electrode electrochemical cell using a platinum wire as the counter-electrode, a saturated calomel as the reference electrode was used, along with the specimen, which was used as the working electrode. To allow the open circuit potential (OCP) to stabilize, samples were kept in the solution for 2 h before electrochemical corrosion tests. Potentiodynamic polarization tests were carried out, starting at −250 mV with reference to the OCP at a sweep rate of 0.5 mV−1 to a final current density of 0.1 $mAcm^{-2}$. Electrochemical impedance spectroscopy (EIS) was conducted at the OCP with an AC amplitude of 10 mV over the frequency range of 10,000–0.01 Hz.

3.8 Wear Tests

A reciprocating ball-on-disc wear tester apparatus was used to evaluate the wear properties of annealed HA/rGO/Pd and HA/rGO/Pt coatings by sliding a stainless-steel ball (6 mm in

diameter) against the specimens at room temperature. The test was performed at a sliding speed of 1 cm/s on a track with a 5 mm diameter at a normal load of 4 N. The COF of coated substrates were determined by repeating this wear three times. Figure 3.9 shows the reciprocating wear test machine.

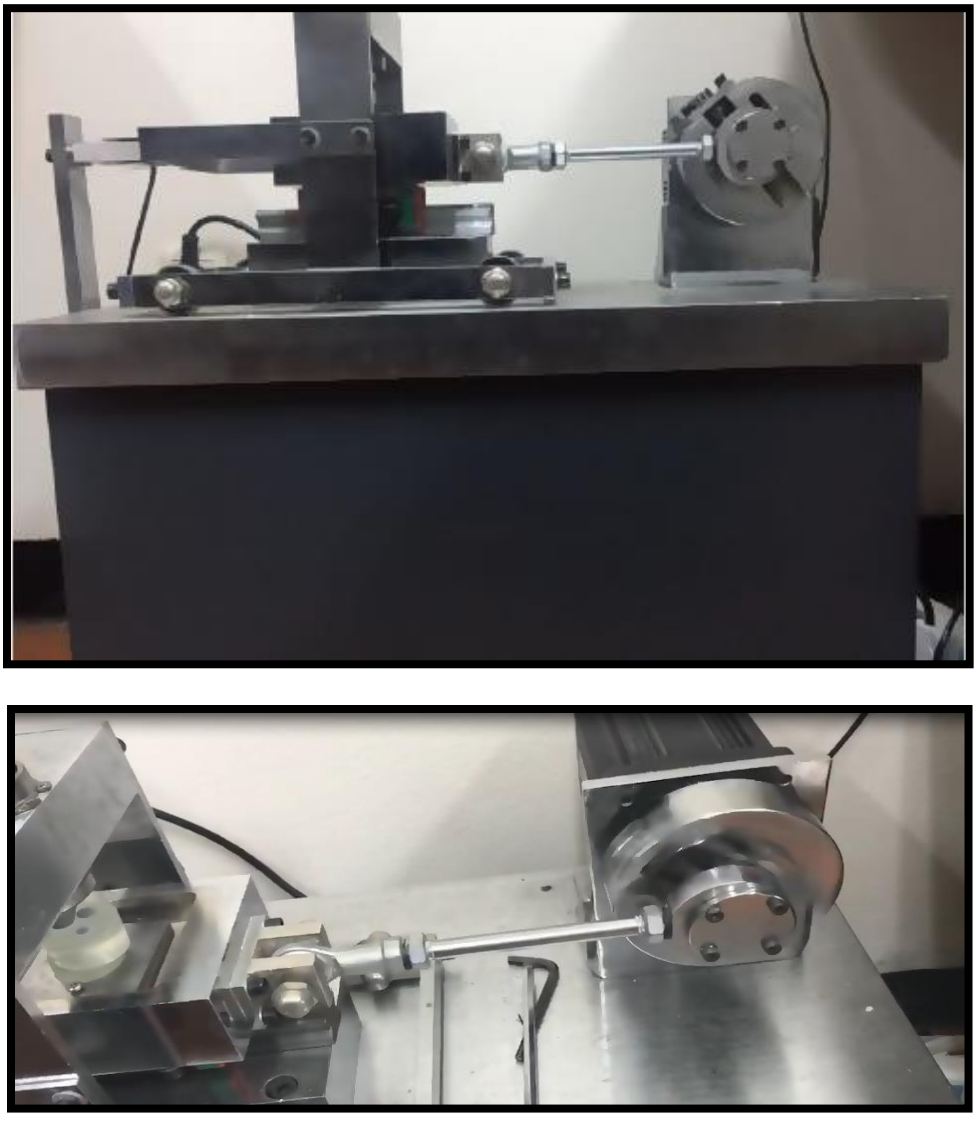

Figure 9.9. Reciprocating wear test machine.

Chapter 4 : Results and Discussion

4.1. Reaction Mechanism of Electrodeposition for HA/GO/Pd

Figure 4.1 is a chronoamperometry plot showing that the electrochemical reaction was initiated at 2 minutes by the electroactive species present in the electrolyte. Between 2 and 6 minutes, a gradual decrease in the current density was observed, indicating particle nucleation on the SST 304 surface and that this process was controlled by electron transfer. Between 6 and 10 minutes, a large decrease in the current density was observed because particles were deposited due to a mixture of mass transport and electron transfer. Between 10 to 30 minutes, the current density plateaued due to mass transport-controlled processes. After 30 minutes, the hydrogen evolution reaction formed many bubbles on the SST 304 surface during scanning. Accordingly, to ensure that hydrogen evolution did not interfere with the formation of coatings on the SST 304 substrate, a 25-minute deposition time was used for electrodeposition on the SST 304 substrate.

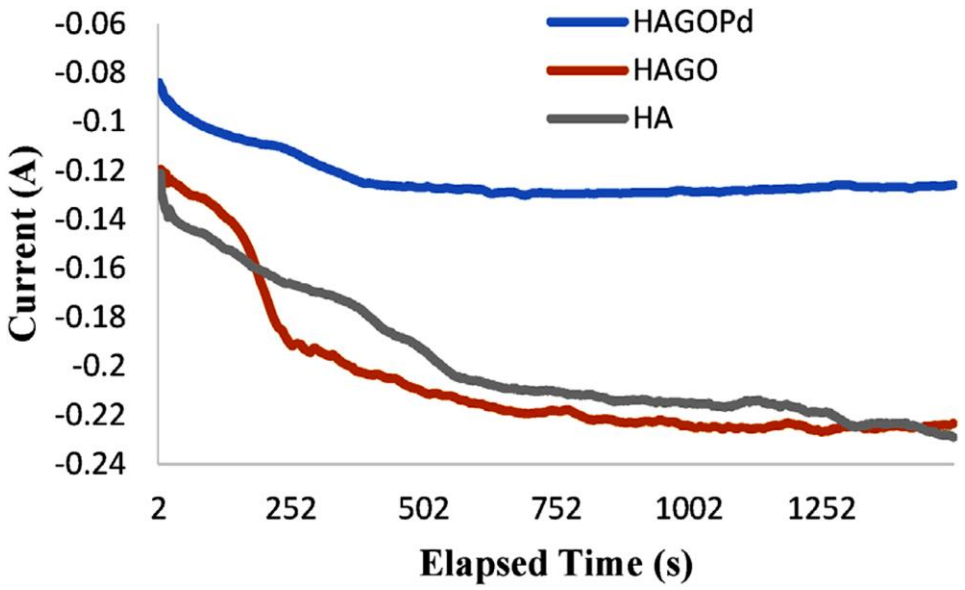

Figure 4.1. Chronoamperometry plot of electrodeposition coatings.

4.2. Reaction Mechanism of Electrodeposition of HA/GO/Pt

Figure 4.2 shows how the current varies with time during the coating process. It can be seen from the figure that the electrolyte within the active material began to participate in electrochemical reactions within 2 minutes. Between 2 and 4 min, the current density was slightly reduced, indicating that particles nucleated on the zirconium surface, and that process is controlled by electron transfer. Note that the current density was reduced between 4 minutes to 10 minutes, indicating that the deposited particles coated the zirconium surface by both mass transfer and electron transfer processes. From 10 to 30 minutes, due to a good transportation process, the current density remained stable. After 30 minutes, many bubbles were observed on the zirconium surface, due to the hydrogen ions in the solution. Hydrogen spills in the electrodeposition synthesis would affect the

adhesion of the coating and the substrate, causing an uneven coating. Therefore, to synthesize an excellent coating that is not disturbed by hydrogen on the zirconium surface, the deposition time should be between 10 to 30 minutes, and so an 18-minute deposition time was selected as an optimum time for getting a coating with good quality.

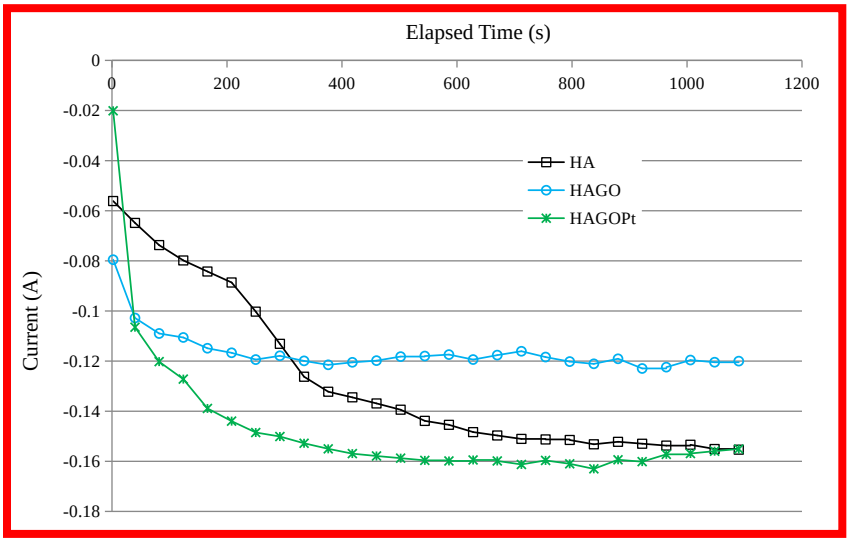

Figure 4.2. Chronoamperometry plot of the electrodeposition of three different coatings

4.3. Coating Morphology and Microstructure Analysis for HA/rGO/Pd

The HA/rGO/Pd thin film nanocomposite electrodeposited on SST 304 was characterized by TEM, SEM, and EDS elemental analysis, whose results are shown in Figure 4.3. SEM images of the morphology and structure at different magnifications of the HA/rGO/Pd nanocomposite in Figures 4.3a and b show that nanoneedle- and nanoplate-like structures of HA and Pd are observed. The surface of the whole substrate was covered with HA nano-

flowers (as a group of needles), and graphene oxide nanosheets that cover the HA nanoneedles and Pd nanoplates are represented by the darker areas of the images. Graphene oxide was expected to behave as a nano-reinforcement filler which inhibited the formation and propagation of cracks via crack deflection at the matrix-GO interface, as well as crack bridging by GO nanosheets [174]. These observations indicate that a continuous and homogeneous coating covered the entire SST 304 surface.

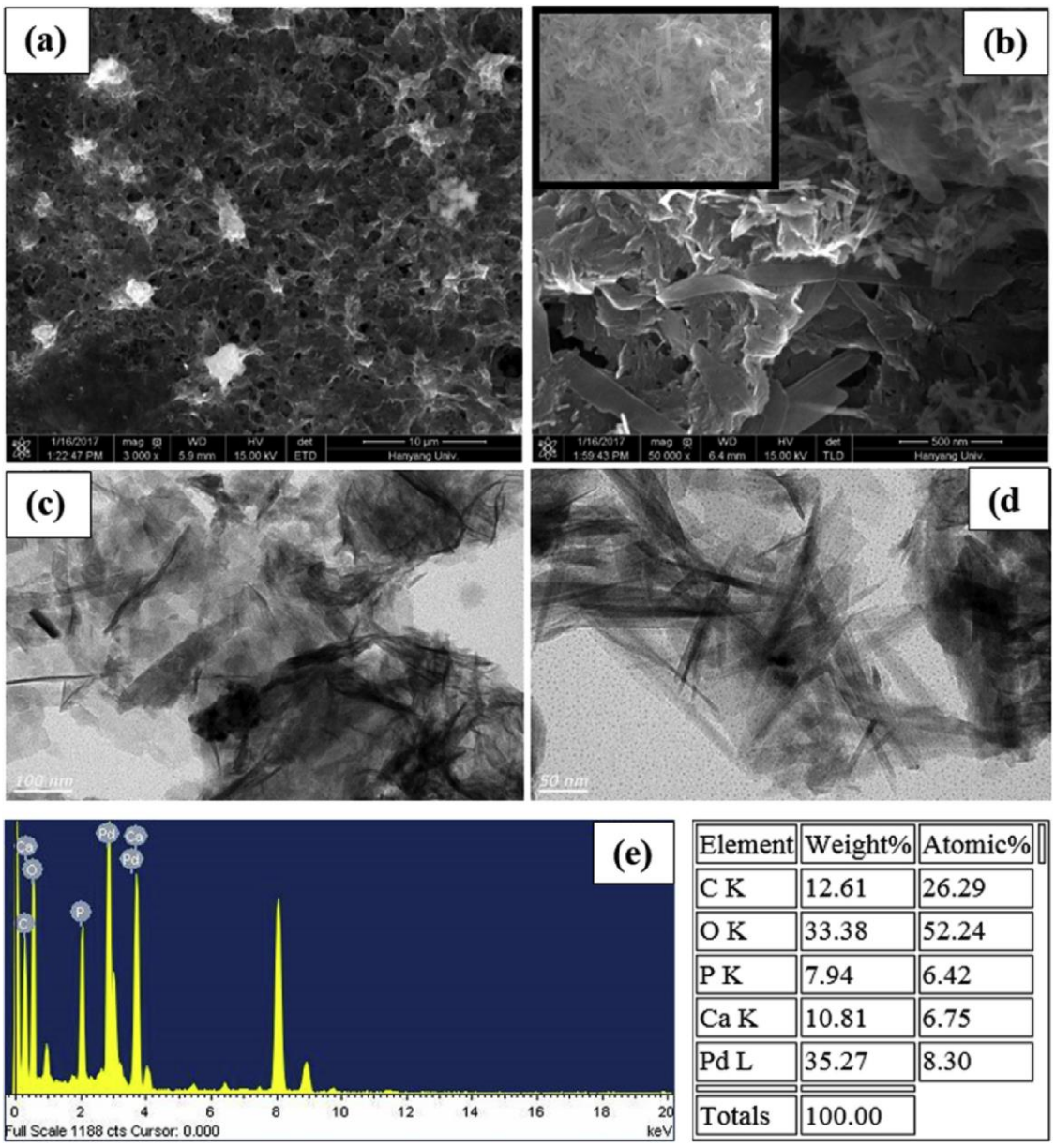

Element	Weight%	Atomic%
C K	12.61	26.29
O K	33.38	52.24
P K	7.94	6.42
Ca K	10.81	6.75
Pd L	35.27	8.30
Totals	100.00	

Figure 4.3. HA/rGO/Pd thin film nanocomposite electrodeposited on SST 304 analyzed by SEM (a,b), TEM (c,d), and EDS elemental analysis (e).

The TEM images of the morphology and structure of HA/rGO/Pd in Figures 4.3c and d show that the synthesized HA/rGO/Pd particles aggregated to form isolated sheets (Figure

4.3c). Needlelike shapes with lengths of 150 ± 25 nm and diameters of 25 ± 5 nm were formed by the HA particles on the GO sheets (Figure 4.3d). Prior to TEM analysis, ultrasonication was performed on an HA/rGO/Pd sample, and nearly no HA or Pd particles were scattered out of the matrix. These results suggest that the HA and Pd particles had strong interactions with the GO.

EDS (Figure 4.3e) was performed to determine the elemental composition to provide further evidence that the HA and Pd particles had been successfully formed. The spectra showed two distinct Pd and Ca peaks, C and O peaks, as well as a large percentage of C and Cu due to the GO sheets and the TEM copper grid. EDS showed that the Ca/P ratio of HA formed in HA/rGO/Pd was about 1.65. While this value is slightly less than the stoichiometric ratio of Ca/P in HA (~1.67), it is similar to the ratio in natural bone [175].

The HA/rGO/Pd nanocomposite coating had an average thickness of around 1 μm, as measured by the cross-sectional FESEM image in Figure 4.4a, and no three-dimensional macroscopic or bulk defects were detected in the dense and uniform film. The EDS cross-sectional line scan and overlaid elemental profile plot in Figure 4.4b show that the HA/rGO/Pd nanocomposite coating was successfully formed on the SST 304 substrate.

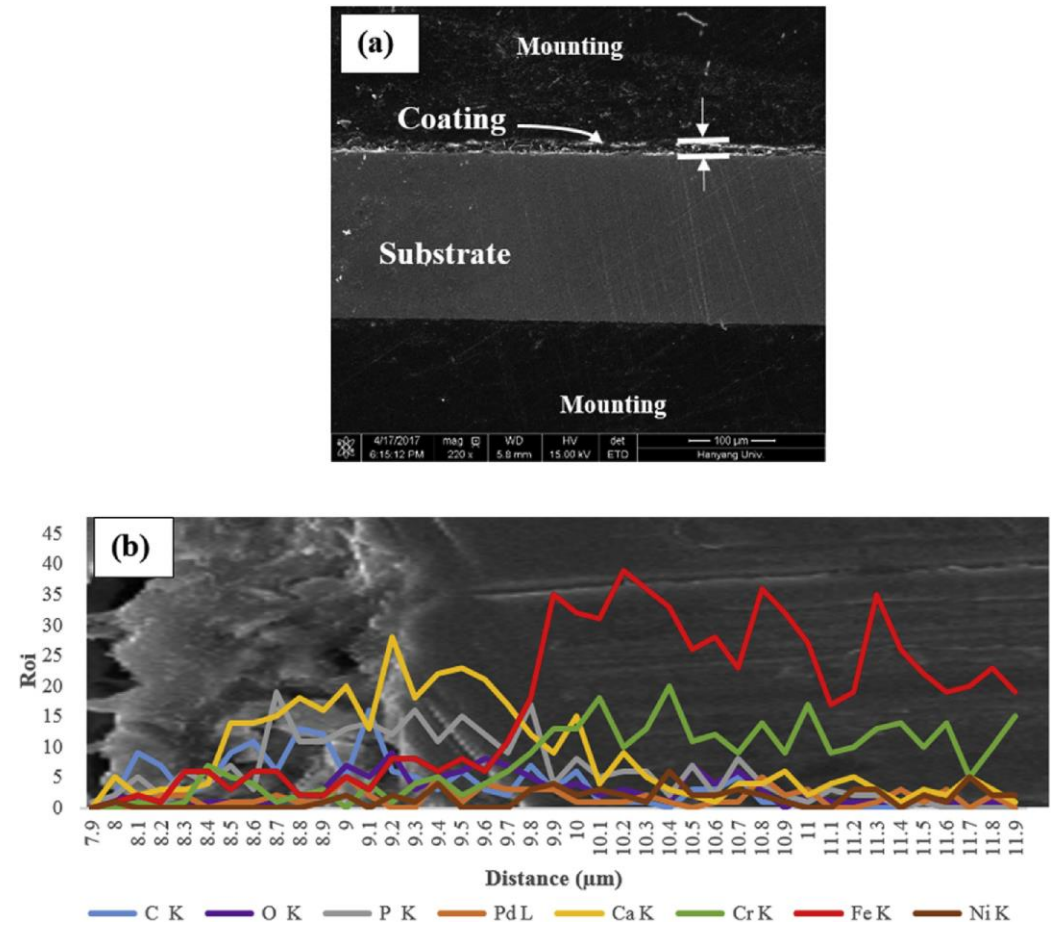

Figure 4.4. HA/rGO/Pd coating analysis: cross-sectional FESEM micrographs (a) and elemental profile plot (b).

HA/GO and HA/GO/Pd coatings were analyzed by XRD (Figure 4.5a) to obtain their phase analysis. The obtained spectra perfectly matched the pure synthesized HA (PDF# 09-0432) at 2θ values of 25.9°, 31.8°, 39.8°,46.7°, 49.5°, and 53.2°, which were indexed to be (002), (211), (310), (222), (213), and (004) planes, respectively. Nanocrystallites of the HA particles were indicated by the presence of broad diffraction peaks. Such structures have been reported to have superior osseointegration properties towards micro HA [176].

Furthermore, the crystallite size and the interplanar distance of (002), (211), (310), (222), (213), and (004) planes were 54.78, 45.42, 37.31, 32.85, 31.45, and 29.875 nm, and 0.1453, 0.1777, 0.2210, 0.2573, 0.2716, and 0.2904 nm, respectively. Due to its ability to act as a reinforcing filler in biomaterial-based composites, graphene is an ideal material when used to modify biomaterials [177-180], and it also forms van der Waals interactions with HA, further strengthening the composites [178,181,182].

The successful reduction of GO is indicated by the broad (002) peak at 24.85°. Although the FESEM and TEM images in Figure 4.3 confirm their presence, no other traces of graphite peaks were observed due to the strong HA peaks in the vicinity and their low GO content. The absence of rGO peaks is probably due to the layered structure of rGO which contains three-dimensional irregular arrays of atoms [183]. New diffraction peaks of the (111) plane at 2θ = 40.12°, (200) plane at 2θ=46.66°, and (220) plane at 2q ¼ 68.12 appeared in the XRD spectra of HA/GO/Pd compared with HA/rGO. These peaks were attributed to the face-centered cubic (fcc) structure (Fm3m) of palladium with a preferred orientation of (111). Additionally, the (111), (200), and (220) planes had interplanar distances and crystallite sizes of 0.2226, 0.2571, and 0.3635 nm, and 37.99, 33.65, and 26.38 nm, respectively.

The results of the FTIR analysis of HA, HA/rGO, and HA/rGO/Pd are shown in Figure 4.5b. The peak due to the P-(OH) stretching vibration in HPO_4^{2-} was observed at 875 cm^{-1} [184,185]. The peaks at 962, 1022, and 1085 cm^{-1} were attributed to the PO_4^{3-} group due to the O-P-O phosphate ions present at hydroxyl locations [186,187], while the C=O group stretch in the amide I band was located at 1642 cm^{-1}.

The stretch of the structural OH^- groups in the hydroxyapatite lattice were located at 3567 cm^{-1} [188]. The presence of a majority of B-type hydroxyapatite was suggested by the presence of bands at 1420 and 1456 cm^{-1}, which were attributed to the v_3 asymmetrical stretching vibrations of CO_3^{2-} ions [184,189,190]. Due to its good bioactivity and osteoconductivity, this material is an ideal substitute in human bone [189]. The skeletal vibration of graphene nanosheets was observed as a band located at 1577 cm^{-1} in the spectrum of HA/rGO FT-IR [191,192]. The presence of graphene oxide sheets was further verified by the appearance of absorption bands of methylene groups (CH_2) near 2855 and 2924 cm^{-1} in the spectrum of the HA/rGO/Pd coating [174,175,186]. These spectral results indicate that the HA/rGO/Pd nanocomposite coatings were successfully co-deposited.

Due to the use of different annealing temperatures, the presence of rGO in the composites needs to be determined. To this end, changes in the crystallinity and structure of rGO in the coatings were examined using Raman spectroscopy, and the results confirmed that rGO was present (Figure 4.5c 1 and 2). In the HA/rGO/Pd sample annealed at 600^oC, the rGO characteristic peaks were successfully detected both before and after annealing. The G band at 1580 cm^{-1} and the D band at 1330 cm^{-1} suggest the first-order spectrum of graphene, while the 2D band refers to the second-order (two-photon) spectrum at 2647 cm^{-1} [193]. Raman spectra are often employed when it is necessary to measure the quality of graphene and the number of graphene sheets by the position of the 2D peak [194]. If the 2D peak shifts to lower wavenumbers, there is most likely a thinner rGO layer on the coating, and the rGO features were retained.

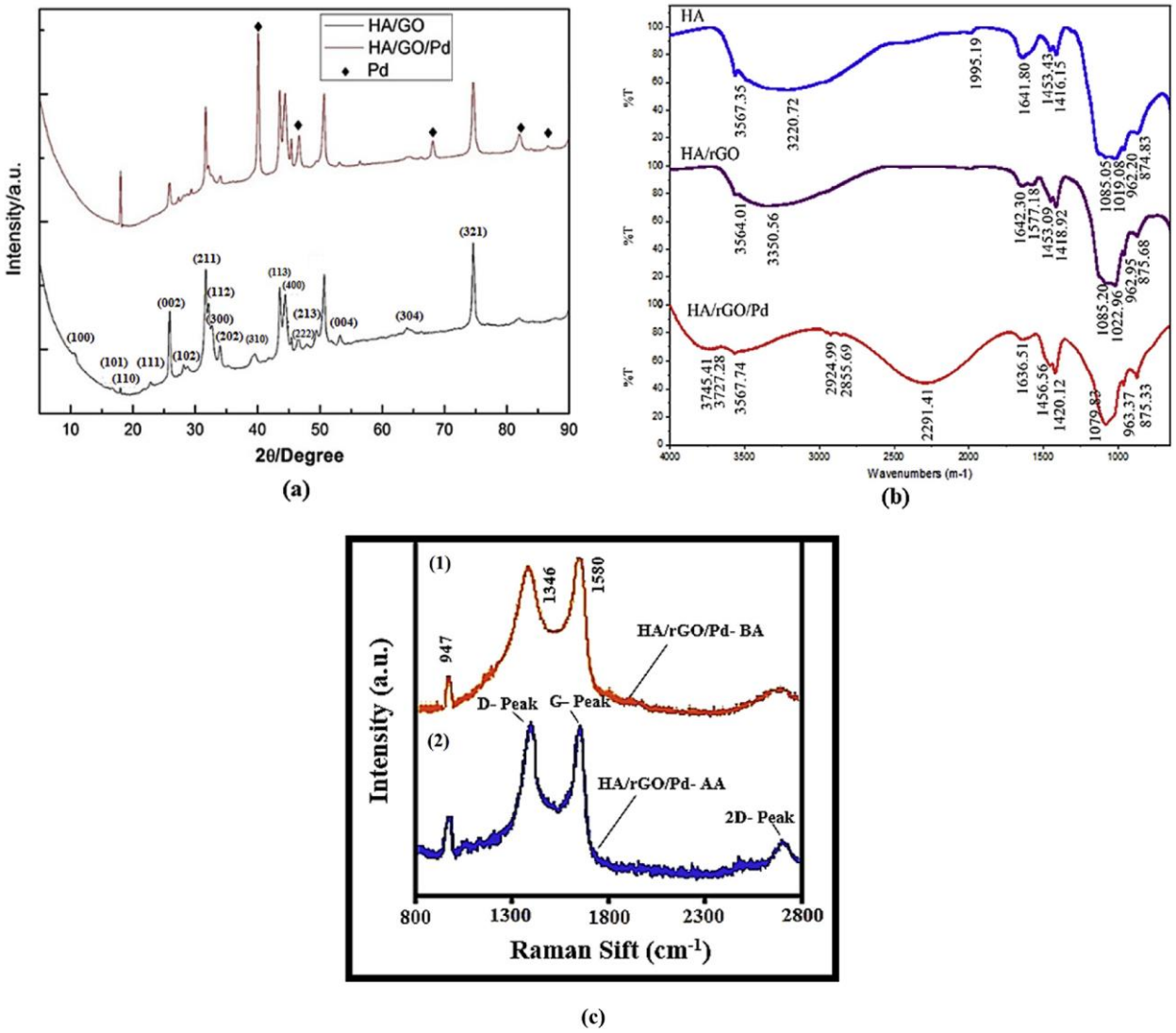

Figure 4.5. HA/GO and HA/GO/Pd coatings phase analysis (a), HA, HA/rGO, and HA/rGO/Pd FTIR spectra (b), HA/rGO/Pd-BA (1), and HA/rGO/Pd-AA 600 °C (c) Raman spectra. BA and AA represent before annealing and after annealing, respectively.

4.4 Coating Morphology and Microstructure Analysis (HA/GO/Pt)

HA, HA/GO, and HA/GO/Pt composite coating XRD patterns are presented in Figure 4.6.

The XRD diffraction peaks of the three samples were located at (002), (211), (103), (401), and (213) which represent the typical structure of hydroxyapatite (JCPDS 09-0432). The (111), (220), and (200) diffraction peaks in the HA/GO/Pt sample indicate that the HA/GO/Pt composite was successfully synthesized (JCPDS 04-0802). In addition, the diffraction peaks of HA decreased after the addition of GO and GO/Pt. The three most intense peaks of (300), (103), and (401) between 30° and 45° (2θ) in the standard diffraction curve were not obvious, possibly due to the low crystallinity or nanometer scale distribution. Clearly, the crystal size of hydroxyapatite is small from the sharp diffraction peaks [195, 196].

The FT-IR spectra of GO, HA/GO, and HA/GO/Pt coatings are shown in Figure 4.7, and the characteristic absorption bands and corresponding wavenumbers are labeled. A hydroxyl group stretch appeared in the form of mutual absorbance bands near 3285 cm^{-1}. Phosphate bending and stretching appeared as bands at 1018.42, 981.17, and 560.48 cm^{-1} [197]. The band at 601.55 cm^{-1} is attributed to the vibrational mode of the OH^- group in the HA structure [198,199]. The band at 871.42 cm^{-1} is assigned to the P-(OH) stretching vibration in the HPO_4^{2-} phosphate group [200, 201]. The bands at 1653 cm^{-1} and 1456 cm^{-1} are assigned to the stretching vibrations of the carboxyl group ($COOH^-$) on the edge of the basal planes or in conjugated carbonyl groups (C=O) and the sp^2 hybridized C=C vibration stretching, respectively [202]. The methylene groups (CH_2) absorption bands, which are inherent in the GO, appeared at approximately 2959 cm^{-1} and 2928 cm^{-1}. The O-H deformation indicated by the peak at 1425 cm^{-1} [174]. In contrast, the peaks at 1750 cm^{-1} and 1425 m^{-1} in the FT-IR spectrum of the HA/GO composite are no longer visible, which

indicates the reduction of GO.

Structural analysis and surface morphology of electrodeposited thin films of HA/GO/Pt over a zirconium substrate were performed using SEM and TEM. Figure 4.8a-f show SEM micrographs of HA/GO/Pt coatings at different magnifications. The entire surface of the pure zirconium substrate is covered by hydroxyapatite particles, Pt nanowalls, and graphene nanosheets, and the surface of the coating is porous. An SEM micrograph of the composite coating (Figure 4.8a) shows the characteristic morphology for HA agglomerates with different sizes. The SEM micrograph of the HA/GO/Pt composite coating (Figure 4.8c) shows HA particles and nanowalls wrapped by reduced graphene oxide nanosheets. The composite coating's morphology was significantly changed after graphene was incorporated. Figure 4.8e shows wave-like graphene sheets, well-dispersed in a broccoli-looking HA/Pt. In addition, HA/GO/Pt showed a distribution of HA particles in the Pt/graphene matrix. HA and graphene are bound by Van der Waals interactions [181]. Therefore, the nucleation of HA crystals perhaps occurs on either the cross-section of graphene multi-sheets or the graphene wall, followed by crystal growth perpendicular or along the graphene sheet's surface. Figures 4.8g and h show the TEM at different magnifications, and Figure 4.8i shows the EDS elemental analysis of HA/GO/Pt composite. According to the EDX results, the composite coating consists of Ca, P, Pt, and C, indicating the presence of Pt, HA nanowalls, and graphene oxide nanosheets.

Figure 4.9 shows a cross-sectional FESEM micrograph of the HA/GO/Pt coating on the zirconium substrate which had a thickness of around 1.1 µm. A uniform coating was formed, without the presence of three-dimensional macroscopic or bulk defects.

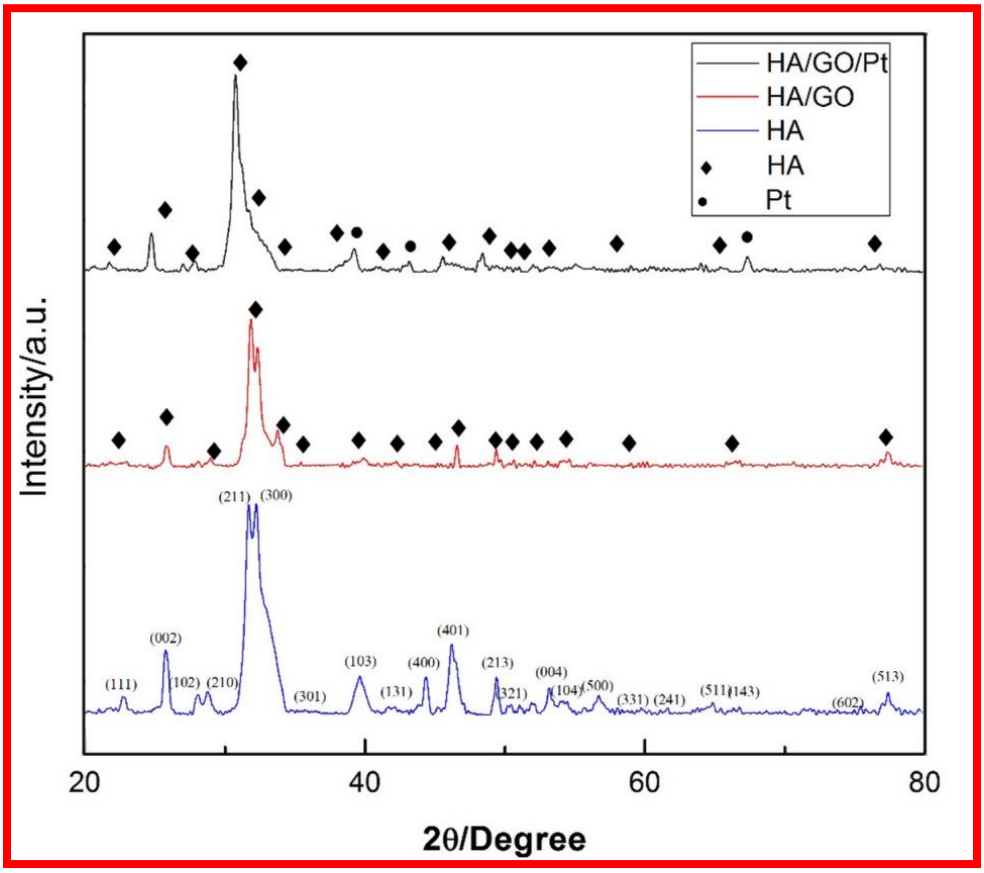

Figure 4.6. X-ray diffraction patterns of the synthesized HA, HA/GO, and HA/GO/Pt.

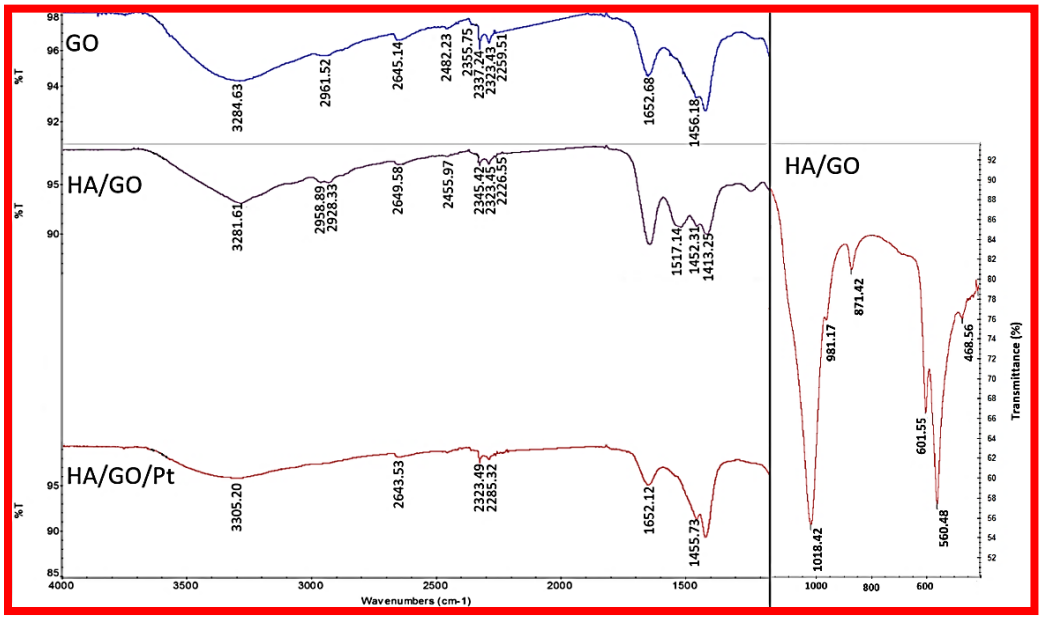

Figure 4.7. FT-IR spectra of GO, HA/GO, and HA/GO/Pt coatings on zirconium.

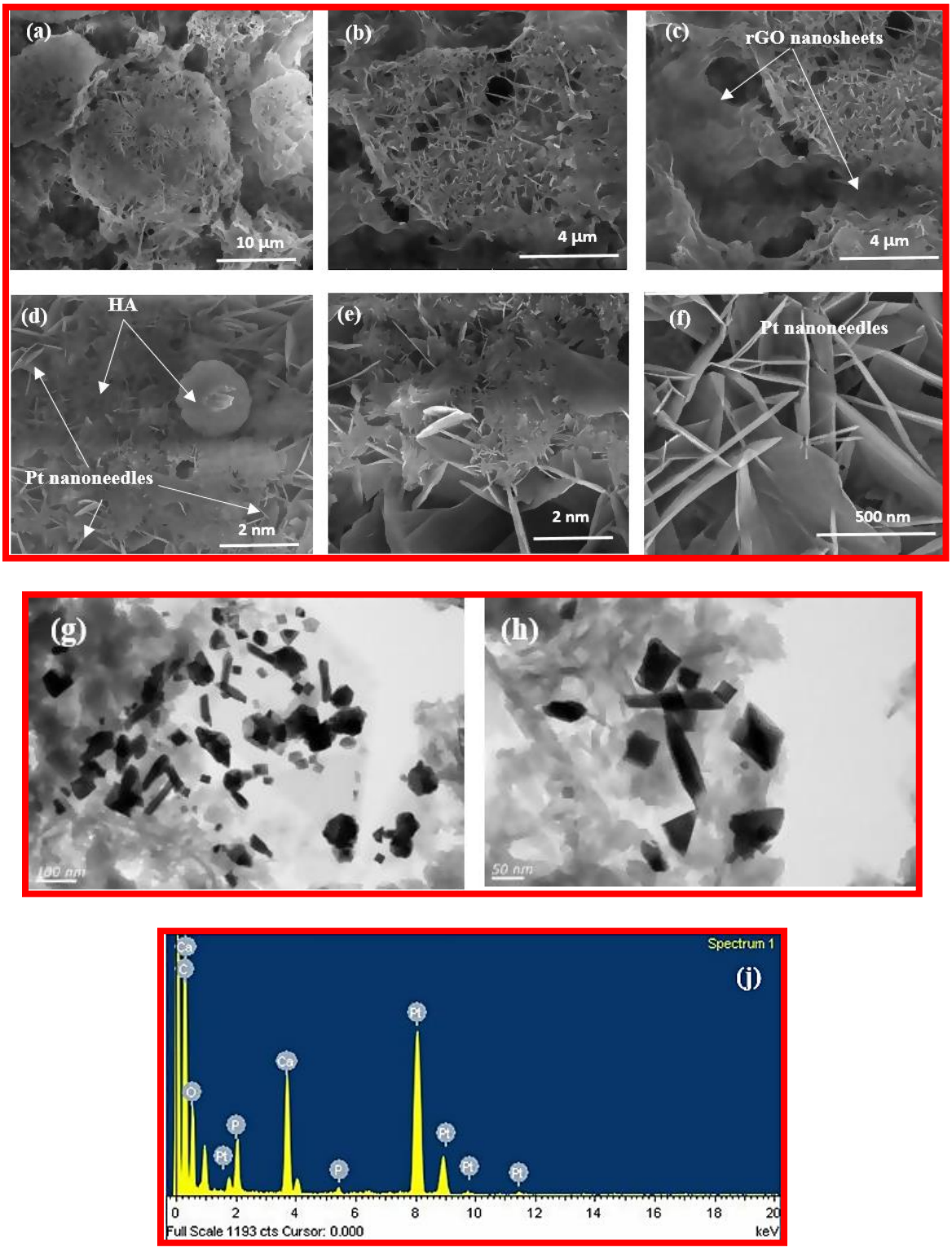

Figure 4.8. Top-down FESEM images (a-f), TEM (g and h), and EDS (i) of HA/GO/Pt.

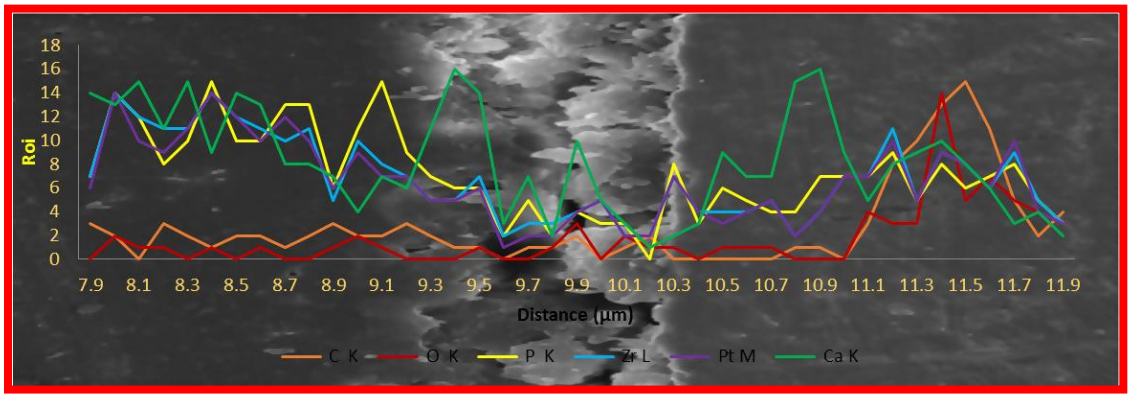

Figure 4.9. Cross-sectional FESEM micrographs overlaid with the elemental profile plot of HA/GO/Pt.

4.5 Biocompatibility Tests (HA/GO/Pd)

In order for it to proliferate and form mineral deposits, and osteoblast must adequately adhere to the surface of an implant [203,204], and this phenomenon also plays an important role in osseointegration which ultimately determines the lifetime of biomedical implants [205]. The cell viability results in Figure 4.10 show that the uncoated SST 304 surface provided insufficient cell attachment and growth. However, the bright fluorescent signal from the green fluorescent protein (GFP) produced within the viable MDA-MB-231 cells indicated good cell attachment and proliferation on the surface of the HA-coated SST 304. A characteristic epithelial morphology was observed as cells continued to spread over surfaces, indicating the cells strongly adhered to the surface and that it was biocompatible. Previous reports have indicated that the presence of GO fillers promotes a more optimal surface for osteoblast adhesion than a pure HA coating [206,207]. Similarly, a bioactivity increase was observed in the HA/rGO coating in this study in Figure 4.10c and the

biocompatibility of the SST 304 surface improved the spreading of cells and proliferation with HA/rGO/Pd even further. Thus, the HA/rGO/Pd nanocomposite coating demonstrated excellent biocompatibility and has potentially promising applications in biomedical devices.

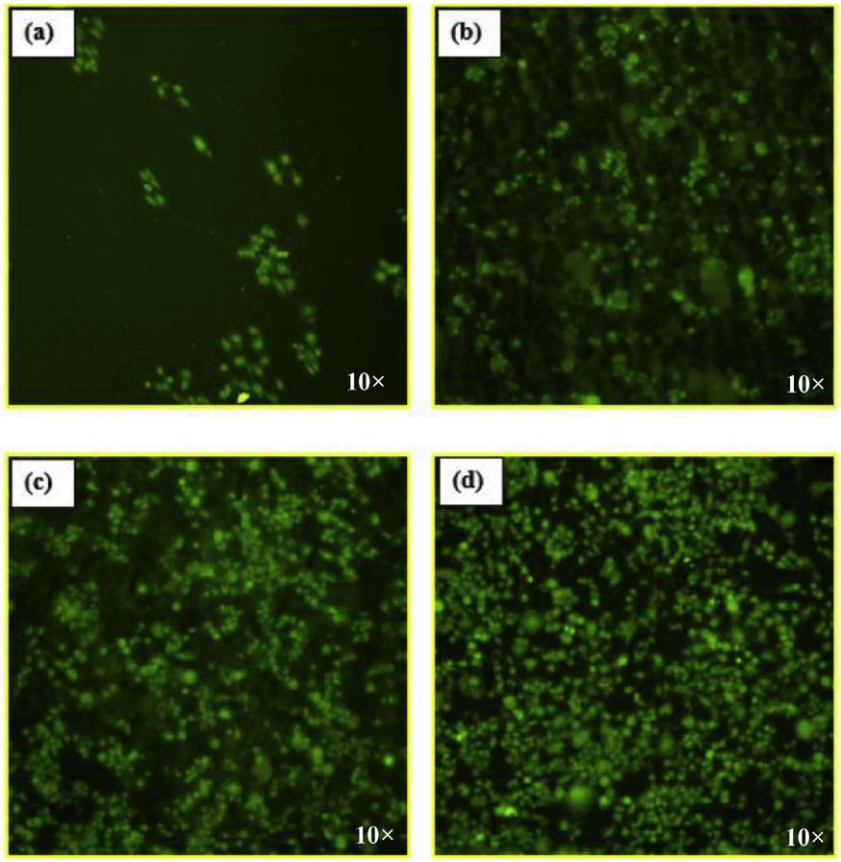

Figure 4.10. Confocal microscopy images of the uncoated (a), HA-coated (b), HA/rGO-coated (c), and HA/rGO/Pd coated (d) SST 304 substrate using MDA-MB-231 cells with GPF to indicate living cells. (The Web version of this image contains an interpretation of the references to color in this figure legend.)

4.6. hMSC in vitro Biocompatibility Assessment

4.6.1 Enhanced proliferation of hMSC on the surface of the St/HA-rGOPd composites

An MTT assay revealed that significantly higher cell viability was observed on cells located on the control grid or St/HA-rGO-Pd composite surfaces compared with cells on the 24-well plates (Figure 4.11; $P < .001$). These results indicated that the new surface grids exhibited had excellent biocompatibility. More importantly, the hMSC proliferation on the St/HA-rGO-Pd-coated surface was higher than on the control grid which also indicates that the synthesized powder's crystallinity can be used to improve the proliferation and viability of hMSC.

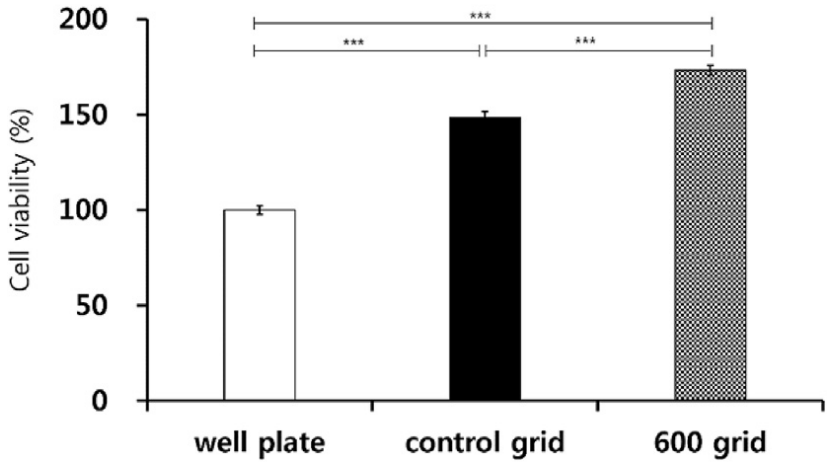

Figure 4.11. The proliferation of the hMSC on the surface of the St/HA-rGO-Pd and HG-3 after 4 days.

4.6.2 Enhanced expression of hMSC marker on the surface of the St/ HA-rGO-Pd composites

Compared with the hMSC in the well plate, the mRNA levels of MSC markers (CD44, CD90, and CD 105) in Figure 4.12 show a notable increase in the hMSC seeded on the surface of the St/HA-rGO-Pd composites or the control grid. None of the test groups displayed the negative MSC marker, indicating that the crystallinity of the powder synthesized in this study may enhance the viability and proliferation of hMSC.

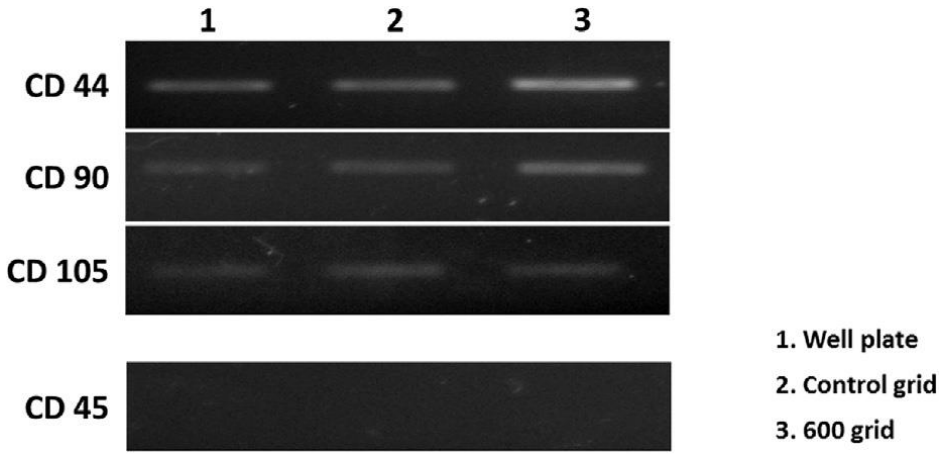

Figure 4.12. hMSC marker expression on the St/HA-rGO-Pd and HG-3 surfaces after 4 days.

4.7 Biocompatibility Tests (HA/GO/Pt)

Figures 4.13a-d show the biocompatibility tests of uncoated and HA-, HA/GO-, and HA/GO/Pt- coated zirconium. When examining biocompatibility, the uncoated zirconium

surface did not provide extensive attachment and growth of adenocarcinoma cells. In stark contrast, the bright fluorescent signal from the GFP produced within the viable MDA-MB-231 cells indicated that the HA and HA/GO-coated substrates enabled cell attachment and proliferation. Moreover, the coating's strong adhesion and biocompatibility were indicated by the cell spreading on the surface which was indicative of a characteristic epithelial morphology. The biocompatibility of the HA/GO/Pt surface also permitted the spreading and proliferation of cells. Figures 4.13a-d show that the cell proliferation and distribution on the HA/GO/Pt coating was lower than on the HA and HA/GO coatings but higher than the bare Zr. It can be concluded that Pt may have significantly affected the biocompatibility and cell proliferation in the HA/GO/Pt composite.

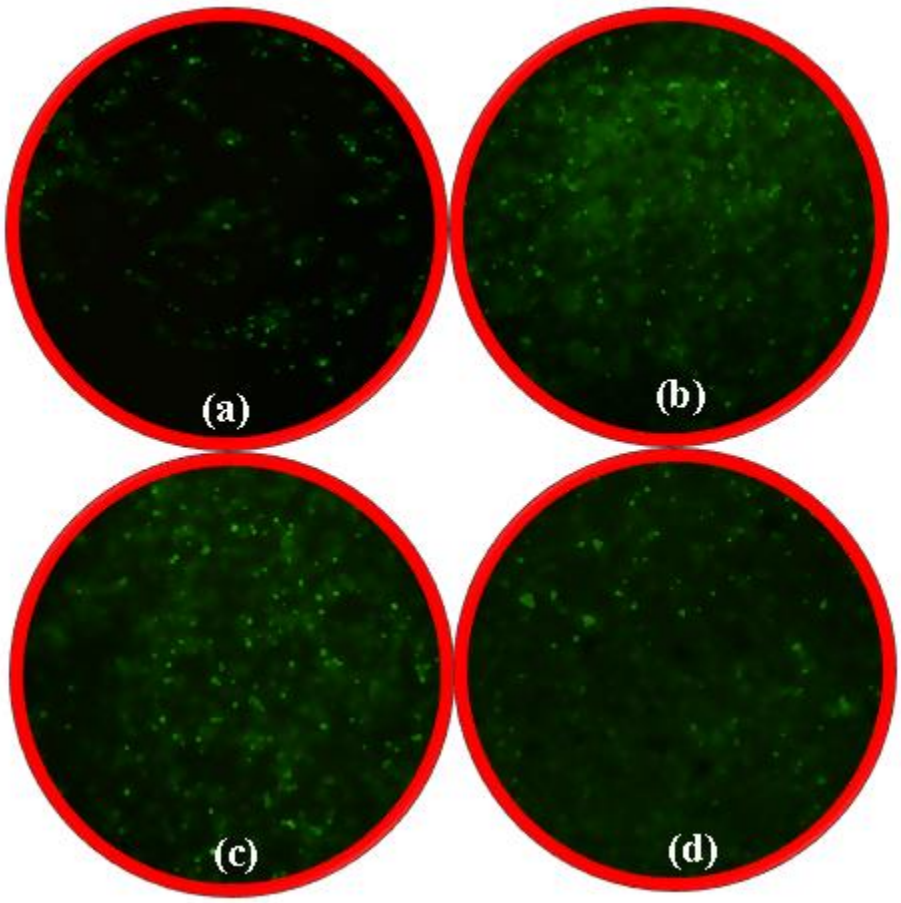

Figure 4.13. Biocompatibility of the (a) uncoated and (b) HA, (c) HA/GO, and (d) HA/GO/Pt coated substrate using the human cell line MDA-MB-231 tagged with a green fluorescent protein as an indicator of living cells.

4.8 Electrochemical Tests and Surface Characterization

4.8.1 Electrochemical tests for HA, HA/ rGO, and HA/rGO/Pd

Potentiodynamic polarization tests in synthetic serum were used to analyze the corrosion

behaviors of the uncoated SST 304, and HA, HA/ rGO, and HA/rGO/Pd coated samples, as shown in Figure 4.14. The corrosion current density (I_{corr}), corrosion potential (E_{corr}), polarization resistance (R_p; calculated from the Stern-Geary equation), and the anodic/cathodic Tafel slopes (β_c and β_a) are summarized in Table 4.1. The corrosion potential of the uncoated SST 304 was calculated to be 0.129 V_{SCE}, with a very high current density (3.83×10^{-6} Acm^{-2}). The coated specimens had a smaller I_{corr} value and a higher R_p than the uncoated SST 304, as indicated by the polarization plot, suggesting that the SST 304 substrates were successfully protected from corrosion in synthetic serum. The addition of GO sheets into the suspensions may have lowered the I_{corr} by increasing the deposition rate which thickened the composite coatings [206]. Its low reactivity and molecular impermeability allow graphene to act as a natural diffusion barrier, giving it great potential for use as a highly corrosion-resistant coating on metal substrates. The corrosion behavior of the obtained samples was also affected by the morphology and microstructure of the coatings. The SEM and TEM images in Figure 4.3 indicate that GO sheets had a parallel orientation with respect to the surface. The synthetic serum could have been inhibited from penetrating the composite coatings, which would further improve the coating's corrosion resistance. The corrosion of the substrate was further inhibited by the addition of Pd into HA/rGO, which improved the corrosion resistance when it was located at grain boundaries [208-210].

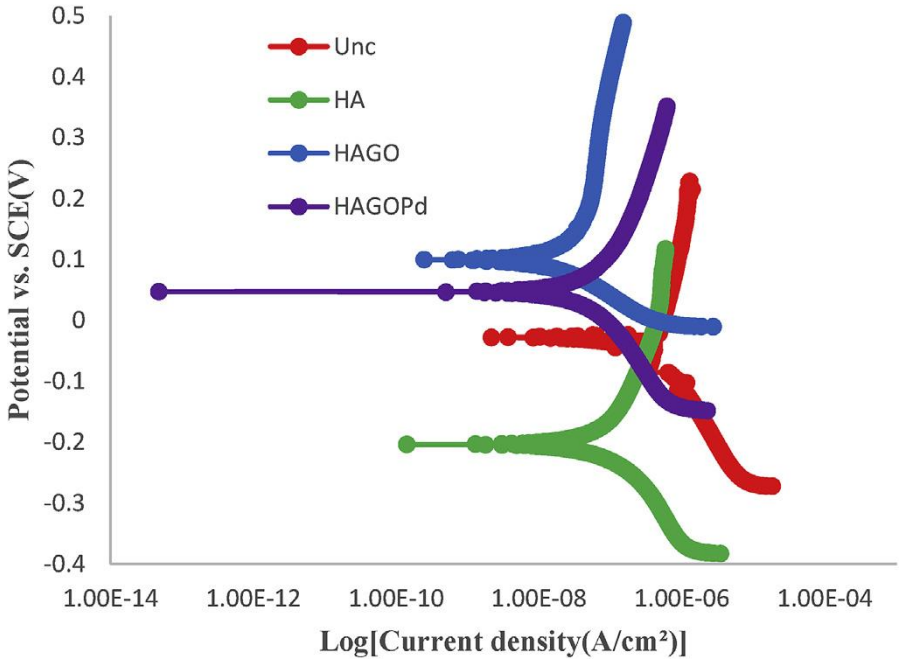

Figure 4.14. The corrosion behaviors of the uncoated SST 304, HA, HA/rGO, and HA/rGO/Pd coated samples.

Table 4.1: Electrochemical parameters during corrosion test.

Sample	E_{corr} (V)	βc (V)	βa (V)	I_{corr} (A/cm^2)	Rp (Ωcm^2)
Uncoated	1.29E-01	2.716	−1.45E+08	3.83E-06	308160.122
HA	−2.02E-01	2.22E-01	6.59E-01	2.11E-07	342158.4047
HA/rGO	9.93E-02	8.29E-03	2.98E-01	2.39E-08	515043.4342
HA/rGO/Pd	4.54E-02	2.36E-01	3.85E-01	1.05E-07	603754.5279

The polarization curves of thermal-treated HA/rGO/Pd nanocomposite coatings at 200, 300, 400, and 600 °C are shown in Figure 4.15, and Table 4.1 shows the E_{corr}, I_{corr}, β_c, β_a,

and R_p values. The value of the corrosion potential and current density of the untreated HA/rGO/Pd was determined to be near 0.045 V_{SCE}, and 1.05E-07 Acm^{-2}, respectively. In contrast, the HA/rGO/Pd-coated sample annealed at 200 ^oC had a more positive corrosion potential (around 0.33 V_{SCE}) than the untreated coating. Moreover, the samples annealed at 200 °C and 300 °C had lower anodic current densities compared with the untreated HA/rGO/Pd coating of 2.48E-08 and 9.18E-08 Acm^{-2}, respectively. These values suggest that the protection provided by the HA/rGO/Pd coating was improved by thermally treating the coating at reduced temperatures, and the hyperbolic plot shifted to a lower current density. The increased annealing temperature introduced coating defects which allowed penetration of the electrolyte since this can severely degrade the coating's electrochemical performance.

Table 4.2: Electrochemical parameters for annealed HA/rGO/Pd specimens at different temperatures.

Sample	Ecorr (V)	βc (V)	βa (V)	Icorr (A/cm^2)	Rp (Ωcm^2)
HT200	3.33E-01	1.19E-01	5.65E-01	2.48E-08	1721545.962
HT300	2.45E-01	1.51E-01	1.36E+00	9.18E-08	642027.8397
HT400	1.57E-01	4.67E-01	1.70E+00	2.56E-06	62250.7107
HT600	−4.97E-02	2.74E-01	1.01E+00	1.92E-06	48896.43981

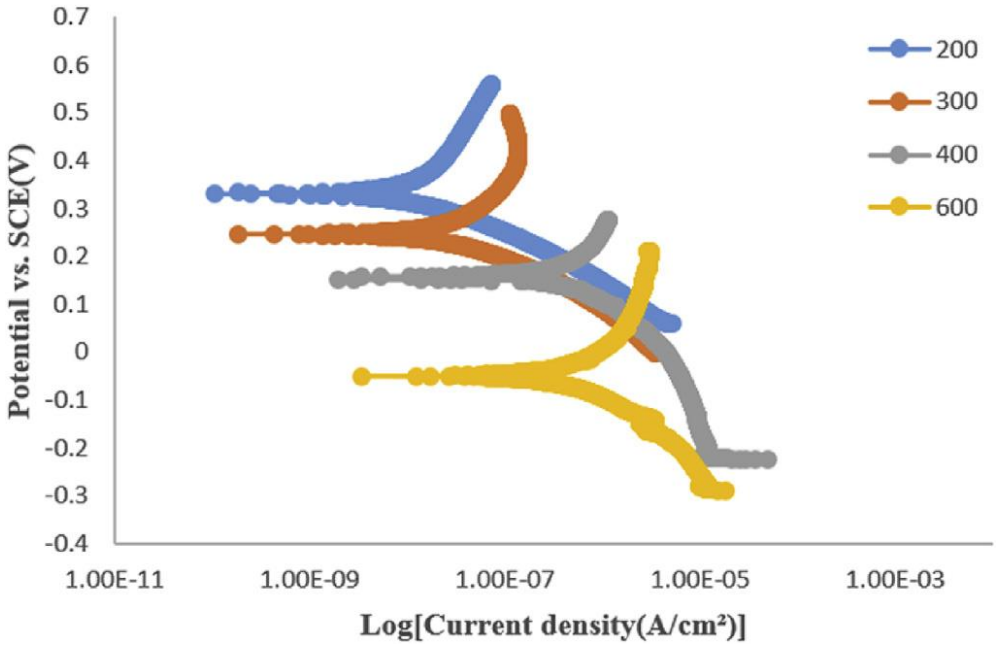

Figure 4.15. The corrosion behaviors of the annealed HA/rGO/Pd coated SST 304.

The HA/rGO/Pd coatings were found to significantly enhance the P.E. in all samples compared with the bare substrate, even in the untreated HA/rGO/Pd coating, which had P.E. of 97.26%. The coating annealed at 200 °C showed the highest protection efficiency at 99.35% (Table 4.3).

Table 4.3 Evaluation of corrosion protection efficiencies (P.E.) of different HA/rGO/Pd coatings compared to uncoated SST 304

Sample	P.E (%)
Untreated	97.25849
HT200	99.35248
HT300	97.60313
HT400	33.15927
HT600	49.86945

4.8.2 HA/rGO/Pd Surface Characterization

The SEM images of the surface of annealed coatings before and after corrosion tests in Figure 4.16 show that both the annealed coatings have good corrosion resistance because no significant changes to its surfaces were observed after being immersed in synthetic serum. Thus, annealing the HA/rGO/Pd coating notably affects its electrochemical behavior.

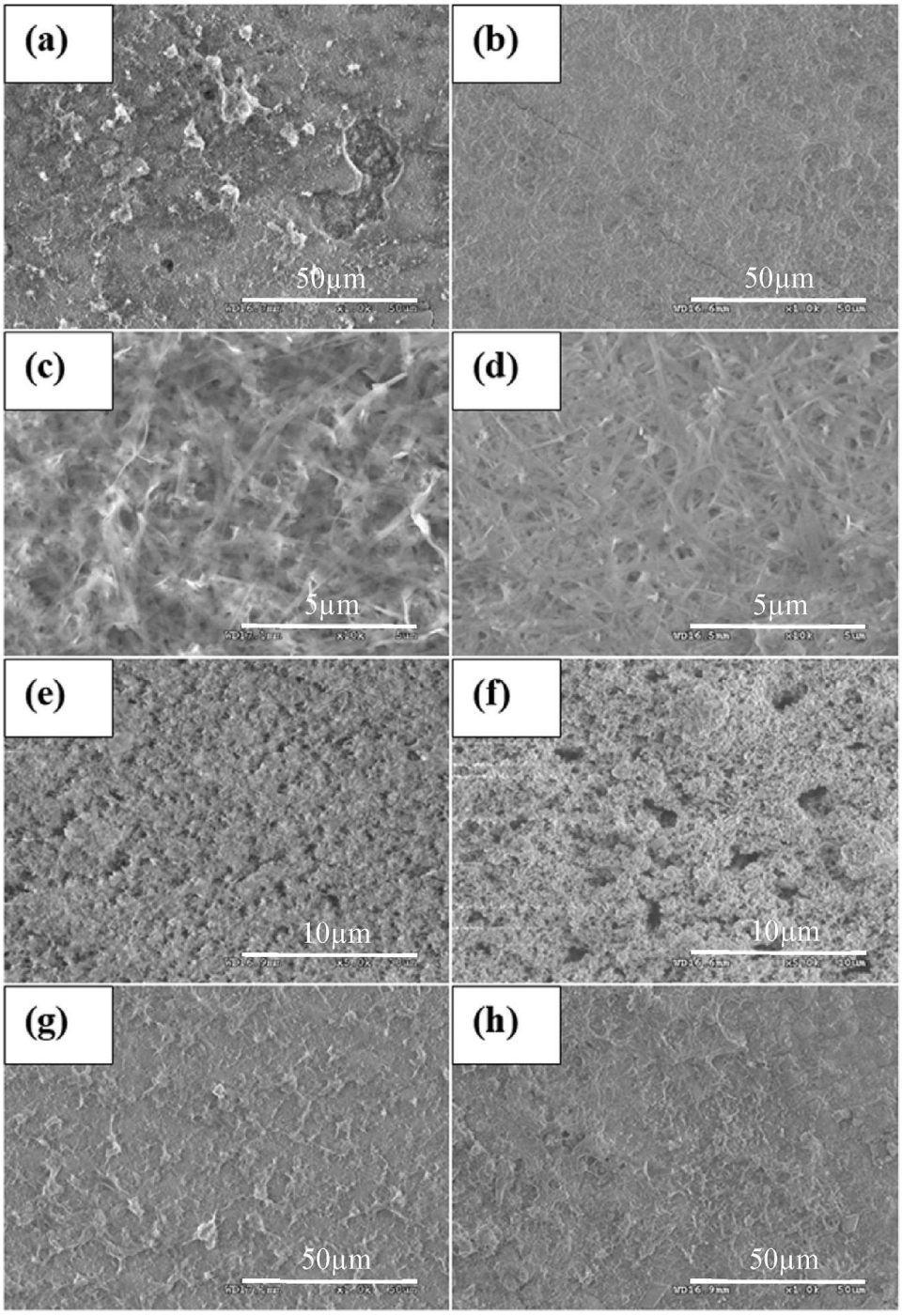

Figure 4.16. SEM micrographs of the surface of the heat-treated HA/rGO/Pd coatings before and after corrosion testing; (a,b) 200, (c,d) 300, (e,f) 400, and (g,h) 600 °C.

The high-intensity HA peaks in the XRD spectrum of annealed HA/rGO/Pd coatings in Figure 4.17 show that the crystal planes (002) and (211) (2θ = 25.8° and 32.0°) closely match the HA pattern (PDF# 09e0432). The (002) and (211) crystal plane diffraction angles shifted in samples subjected to a 2-day immersion in synthetic serum, suggesting that carbonated HA had formed, which should increase the biocompatibility since this is found in bone. Previous literature [211] has shown that growing HA on a coating surface after it is immersed in a biomimetic system (such as synthetic serum) is influenced by the availability of certain functional groups. For example, when the hydroxyl and phosphate ions in HA are exposed to the synthetic serum, the surface of the HA becomes negatively charged. Afterward, Ca^{2+} ions are attracted and consumed, which precipitated calcium phosphate. HA simultaneously dissolves, which increases the solution's phosphate and calcium ion concentrations, causing HA to precipitate, which is a reversible process [209]. The deposition of HA is further promoted by graphene, which attracts calcium ions with its negative surface charge because of the abundant p electrons located in its sp^2 hybrid orbitals [212]. These results show that coating the substrate with HA/rGO/Pd encouraged the nucleation and growth of HA, suggesting that such a coating can be used to promote the adhesion between bone and implants.

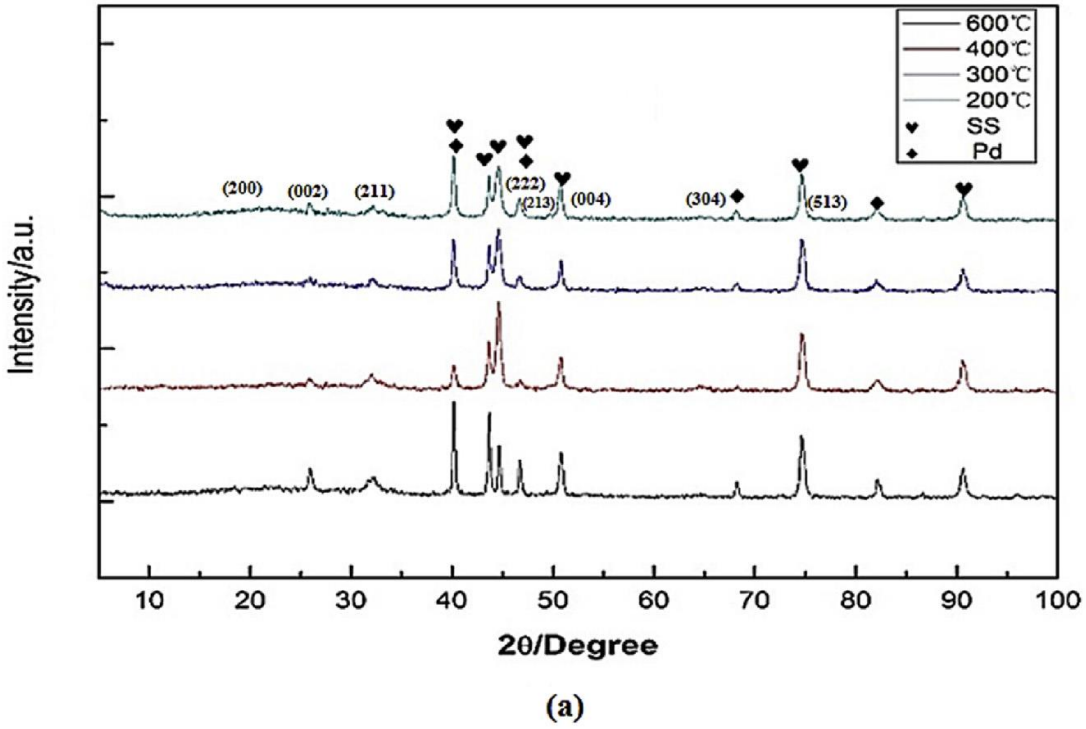

(a)

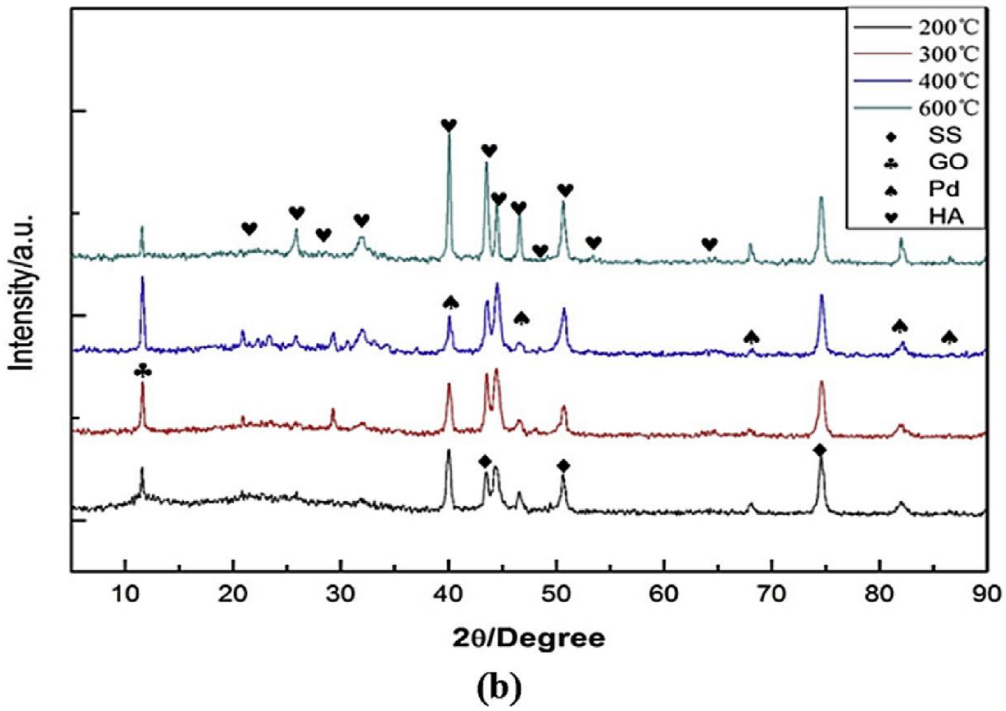

(b)

Figure 4.17. Heat-treated HA/RGO/Pd coatings phase analysis before (a) and after (b) corrosion tests.

4.9 Electrochemical Measurements and Surface Characterization for HA, HA/GO, and HA/GO/Pt

4.9.1 Electrochemical measurements in $CaCl_2$ solution

EIS and PDS measurements were performed in a $CaCl_2$ solution to evaluate the corrosion resistance of the materials in a simulated physiological medium.

Nyquist plots of pure zirconium, zirconium coated with HA, HA/GO, and HA/GO/Pt after different immersion times in $CaCl_2$ solution are shown in Figure 4.18a–e, respectively. The coating is generally responsible for the high-frequency range of the Nyquist plots, while the electrochemical processes on the metal surface beneath the coating are described by the low-frequency range. The EEC contains information about the coating pore resistance R_c, the electrolyte resistance R_s, and constant phase elements CPE_{ox} and CPE_c, which are all frequency-dependent electrochemical phenomena. In addition, information is provided about the capacitance of the passive oxide layer just beneath the coating on the Zr surface C_{ox}, and the coating capacitance C_c [213].

To characterize the corrosion properties of the uncoated, HA-, HA/GO-, and HA/GO/Pt-coated substrates, potentiodynamic sweep measurements were performed in $CaCl_2$, since the current density and corrosion rate are proportional to one another. Potentiodynamic polarization curves of the uncoated, HA-, HA/GO-, and HA/GO/Pt-coated substrates after 7 days in $CaCl_2$ solution are plotted in Figure 4.18. The corrosion current density I_{corr} and corrosion potential E_{corr} were evaluated according to Tafel extrapolation and are listed in Table 4.4. The E_{corr} of pure zirconium (-21.699 mV) and HA coating (164.574 mV) are less-positive than the E_{corr} of HA/GO (267.02 mV) and HA/GO/Pt (499.325 mV).

However, the values for I_{corr} of bare pure zirconium, HA, HA/GO, and HA/GO/Pt are 279.602, 72.1, 50.044, and 27.227 nA, respectively. The I_{corr} of HA/GO and HA/GO/Pt were lower than the I_{corr} of HA and uncoated substrate, implying that graphene and Pt improved the corrosion resistance of the Zr substrate in $CaCl_2$ solution due to the bioactivity of the apatite layer that formed on the HA/GO- and HA/GO/Pt-coated surfaces. The polarization measurement results agree with those obtained from impedance spectroscopy, indicating that the HA/GO and HA/GO/Pt coatings have better corrosion resistance. It also confirmed that the lowest corrosion rate was obtained due to the thick biomimetic apatite layer on the composites' surfaces, showing that the use of graphene-based HA/GO and HA/GO/Pt composite coatings may improve the corrosion resistance, decreasing the metal ion release.

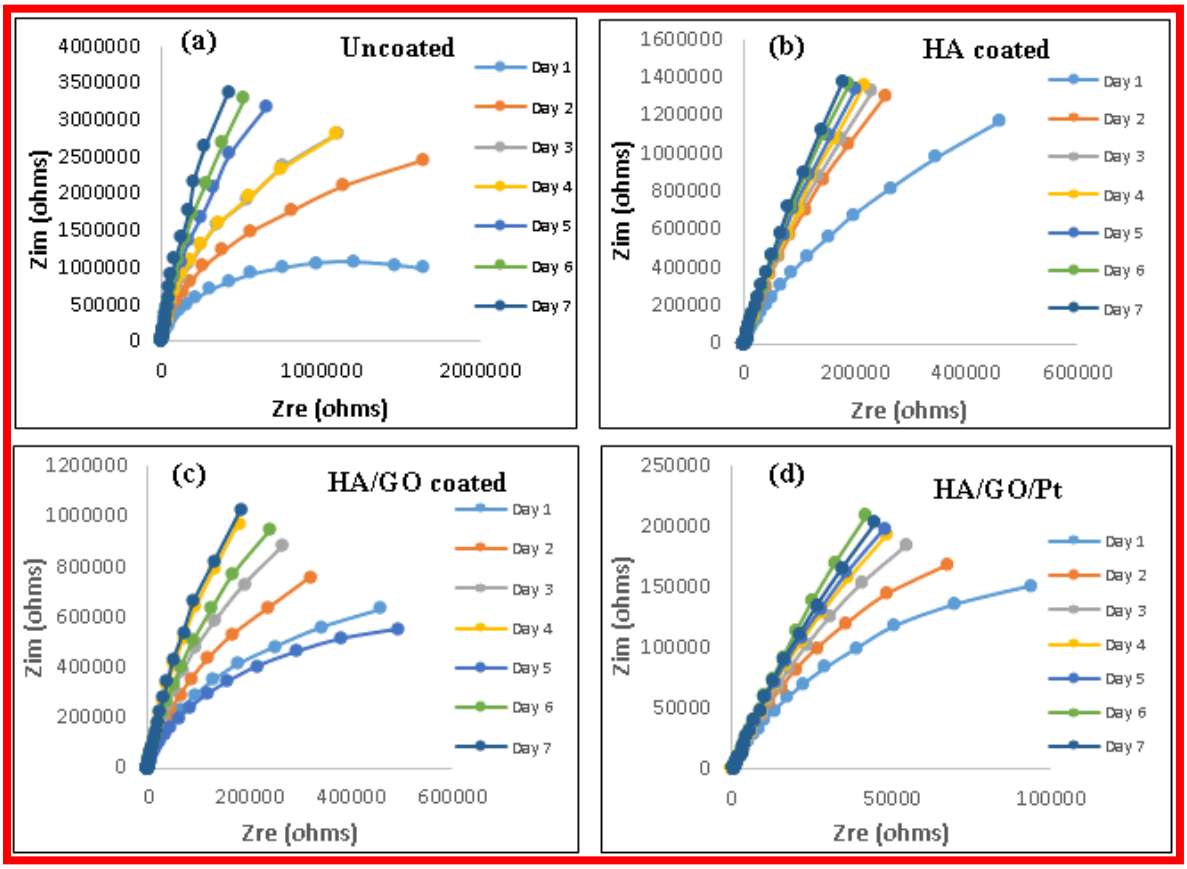

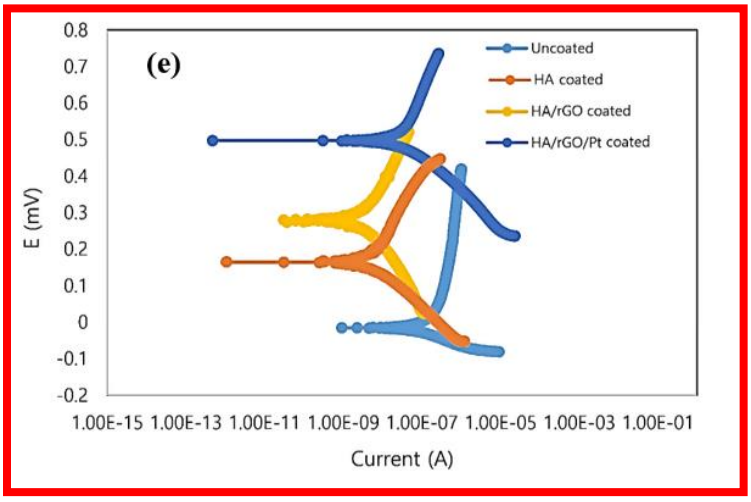

Figure 4.18. EIS spectra of (a) pure zirconium, (b) HA, (c) HA/GO, and (d) HA/GO/Pt coatings on Zr substrate during a prolonged time (7 days). (e) Potentiodynamic polarization curves of uncoated and coated zirconium after 7 days in $CaCl_2$ solution.

Table 4.4: Current density, I_{corr}, and corrosion potential, E_{corr}, obtained from PDS measurements for an uncoated substrate and HA, HA/rGO, HA/rGO/Pt coatings on zirconium after 7 days.

Time/day	**Uncoated substrate**	**HA coating**	**HA/rGO coating**	**HA/rGO/Pt coating**
I_{corr}/nA				
7	279.602	72.1	50.044	27.227
E_{corr}/mV				
7	-21.699	164.574	267.02	499.325

4.9.2 Corrosion behavior and surface morphology of the thermal-treated HA/GO/Pt coated zirconium

Figure 4.19 shows the polarization curves of HA/GO/Pt nanocomposites heat-treated at 200, 300, 400, and 600 ℃. Table 4.5 summarizes their respective E_{corr} and I_{corr}. The corrosion potential, E_{corr}, of HA/GO/Pt-coated samples annealed at 200, 300, 400, and 600 °C were 1.731, 232.858, 379.096, and 309.423 mV, respectively. The results showed that the HA/GO/Pt-coated substrates annealed at different temperatures have lower E_{corr} compared to the untreated HA/GO/Pt coating, indicating that the heat treatment significantly affects the corrosion potential of composite coatings. The current densities of the HA/GO/Pt coatings heat-treated at 200 and 300 ℃ were 16.269 nA and 17.035 nA, respectively, which were also lower than the current density of the untreated HA/GO/Pt coatings (27.227 nA). This indicated that the corrosion resistance of HA/GO/Pt coatings was enhanced by the annealing. The higher corrosion potential (E_{corr}) and the lower corrosion current density (I_{corr}) indicate that the material has better corrosion resistance.

The sample heat-treated at 400 °C (E_{corr} 379.096 mV and I_{corr} 1.521 nA) achieved the best corrosion resistance. As the annealing temperature was increased from 200 to 400 °C, I_{corr} decreased, indicating a superior corrosion resistance, which was caused by the diffusion of coatings into the substrate and integration of the composite materials during heat treatment. Further increasing the temperature to 600 °C increased I_{corr} to 14.15, indicating a decrease in the corrosion resistance due to cracks in the coatings or coating detachment because of the different modulus of elasticity between the coating and the substrate. This can be explained in the way that as the temperature increases the metal substrate expands more than the ceramic layer due to their different expansion coefficient and as the coating cannot expand as much as the substrate then nano/micro cracks will be created.

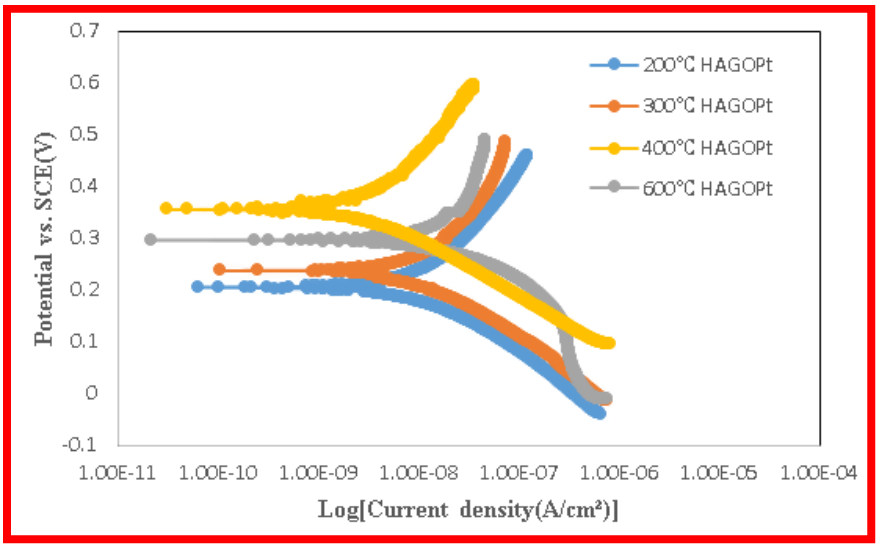

Figure 4.19. The corrosion behaviors of the thermal-treated HA/GO/Pt coated zirconium.

Table 4.5: Corrosion current density, I_{corr}, and corrosion potential, E_{corr}, obtained from PDS measurements for corrosion behaviors of the thermal-treated HA/rGO/Pt coated zirconium.

Time/day	**HT200**	**HT300**	**HT400**	**HT600**
I_{corr}/nA				
2	16.269	17.035	1.521	14.15
E_{corr}/mV				
2	1.731	232.858	379.096	309.423

Figures 4.20a and b present the SEM micrographs of the surface of the non-annealed bare and HA/GO/Pt-coated zirconium substrates immersed in $CaCl_2$ solution for 7 days. The coated samples contained fewer corrosion spots than the bare samples, indicating that the coating effectively improved the corrosion resistance. The SEM morphologies of the HA/GO/Pt coating annealed at 200 and 600 °C before and after corrosion tests are shown in Figure 4.21a-d. As shown in Figure 4.21c, when the annealing temperature was increased to 600 °C, cracks formed over the entire coating due to the elastic moduli mismatch between the coatings and the substrate. This decreased the corrosion resistance as the corrosion solution penetrated the substrate through the cracks. Thus, it can be concluded that a high annealing temperature such as 400 °C may be a better option to improve the corrosion resistance of the HA/GO/Pt composite.

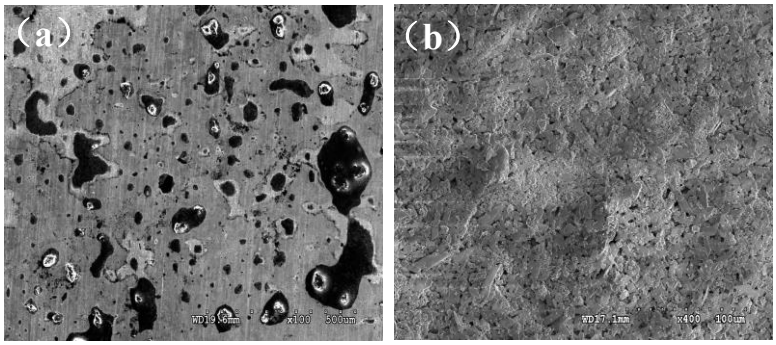

Figure 4.20. SEM micrographs of (a) bare and (b) HA/GO/Pt-coated samples before and after corrosion tests.

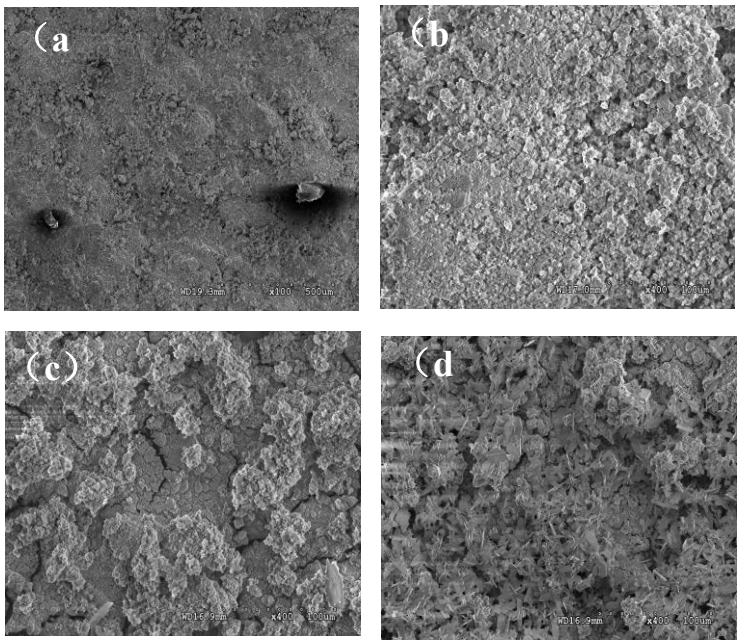

Figure 4.21. SEM micrographs of HA/GO/Pt coatings before and after corrosion tests (a, b) annealed at 200 °C and (c, d) annealed at 600 °C.

Figure 4.22 shows the XRD spectrum of annealed HA/GO/Pt coatings, both before and after corrosion tests. High-intensity HA peaks at crystal planes (002) and (211), $2\theta = 25.8°$ and 32.0°, match the HA pattern of PDF# 09-0432. After being immersed in synthetic serum for 7 days, a shift was observed in the diffraction angles of (002) and (211) crystal planes, which suggested that carbonated HA had formed, which is a promising result since this substance is present in bone. The growth of hydroxyapatite on top of the deposited layer surface after being soaked in a biomimetic system (synthetic serum) depends on how accessible the surface's functional groups are [214]. Exposure of the HA's hydroxyl and phosphate ions to the synthetic serum made the HA surface to become negatively-charged and attract and consume Ca^{2+} ions, which ultimately resulted in the precipitation of calcium phosphates. When hydroxyapatite dissolves, the concentration of calcium and phosphate ions is increased in solution, which causes HA to precipitate. This process of the dissolution and precipitation of calcium phosphates in serum is reversible [215]. The deposition of HA is further promoted by graphene, which attracts calcium ions with its negative surface charge because of the abundant p electrons located in its sp^2 hybrid orbitals [209].

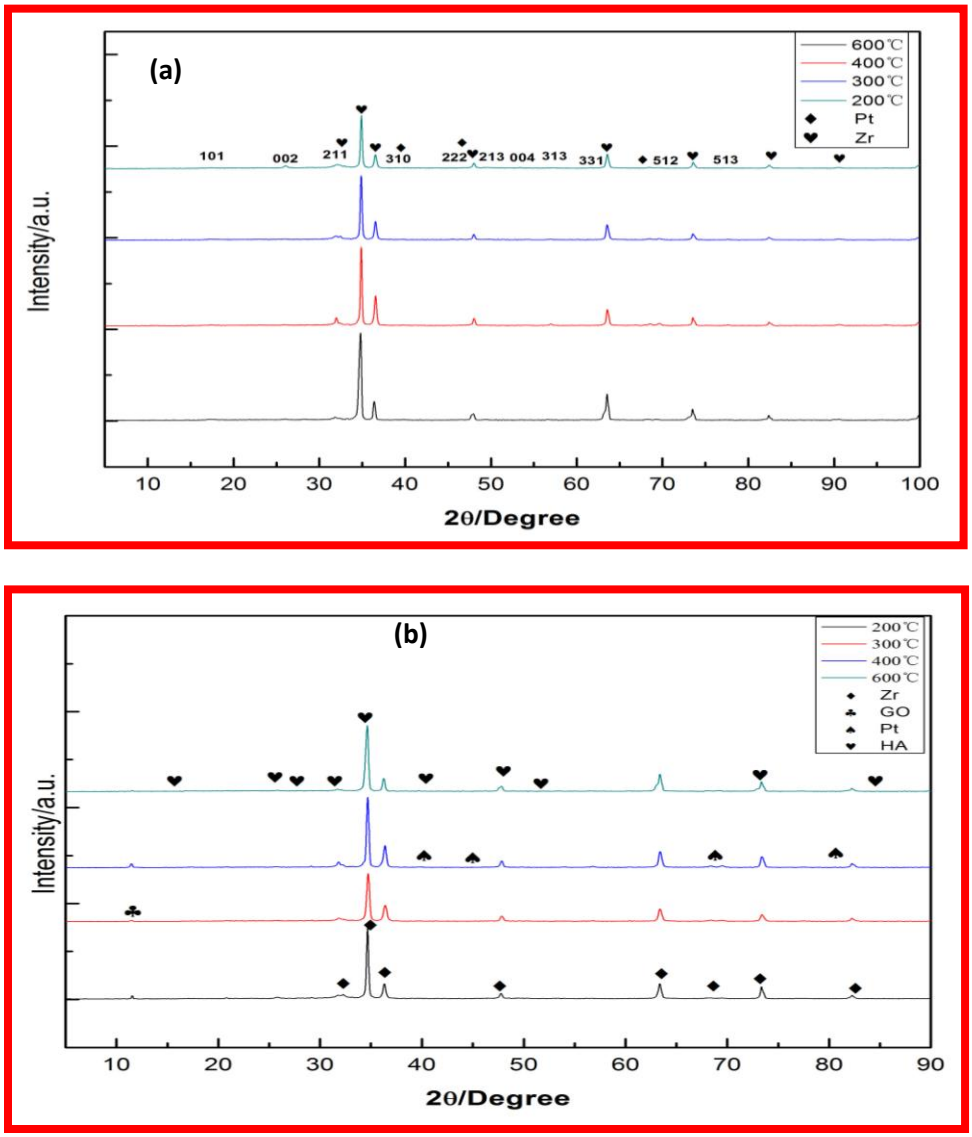

Figure 4.22. Phase analysis via XRD of the heat-treated HA/GO/Pt coatings before (a) and after (b) corrosion tests.

4.10 Wear Test

4.10.1 Wear test for HA/rGO/Pd

Figure 4.23 shows the friction coefficient of annealed HA/rGO/Pd-coated substrates as a

function of their annealing temperature, which significantly affected the coefficient of friction in these materials. For coatings annealed at 200, 300, 400, and 600 °C, the coefficients of friction were 0.702, 0.82, 0.846, and 0.581, respectively. The average coefficient of friction of the coating annealed at 600 °C was much lower than all other samples. When the annealing temperature was increased from 200 to 400 ^{o}C, as shown in Figure 4.23, the COF increased but began to decrease when the annealing temperature was further increased to 600 °C. These results are because the composites have a higher surface hardness, which increased the resistance to mass removal, increasing in the lateral (transverse) force. As the lateral force increased at a constant normal force, the COF of the composites increased as well [216].

Figure 4.24 shows the top-down optical micrographs after wear tests were conducted on the Ha/rGO/Pd-coated substrate annealed at different temperatures. Large aggregated particles generated from the coating particles or chipping flakes accounted for most of the debris. Figure 4.24 a-d shows that increasing the annealing temperature from 200 to 600 °C increased the composite's wear resistance because the thin film adhered more strongly to the substrate. Ar in the tube furnace during sintering (heat treatment) allowed the coating to diffuse to the substrate, improving the coating's adhesion. According to the literature, under physiological conditions, the HA could form a lubricating film with sufficient wear resistance on the surface because the phosphate anions in the coating were hydrated. This formed a large hydration layer, which essentially became molecular ball-bearings capable of lubricating contact and increasing the coating's antifriction properties [217]. The uniform dispersion and high surface area of GO have been suggested to impart uniform sites that contribute to the energy release and high fracture toughness of the coating, which

increases its wear resistance [218]. Kvetkova et al. also reported that the crack deflection was increased by using graphene, which reduced the rate of crack propagation, crack bridging, and dissipated crack energy [219]. These results suggest that a continuous GO layer significantly increases the wear resistance of HA/rGO/Pd coatings.

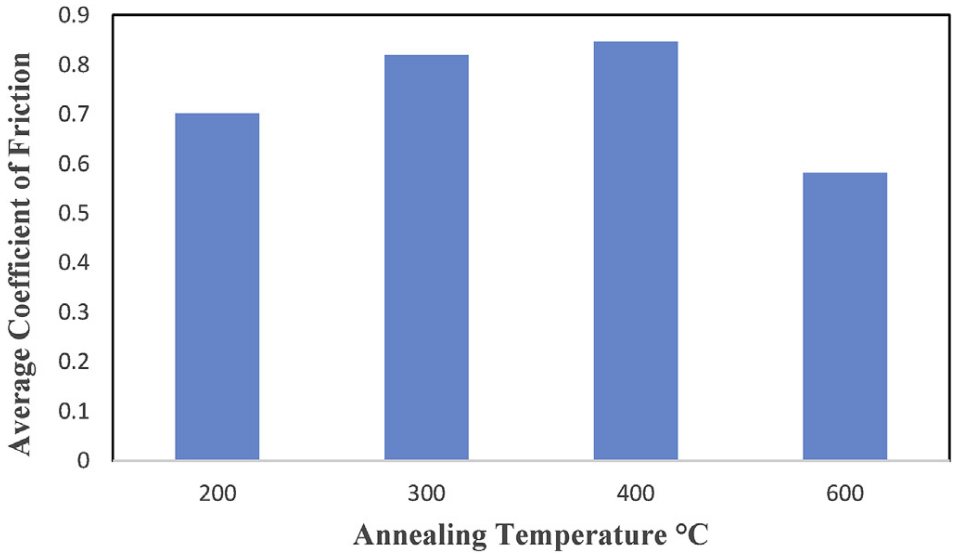

Figure 4.23. The friction coefficient of HA/rGO/Pd coatings vs. annealing temperature.

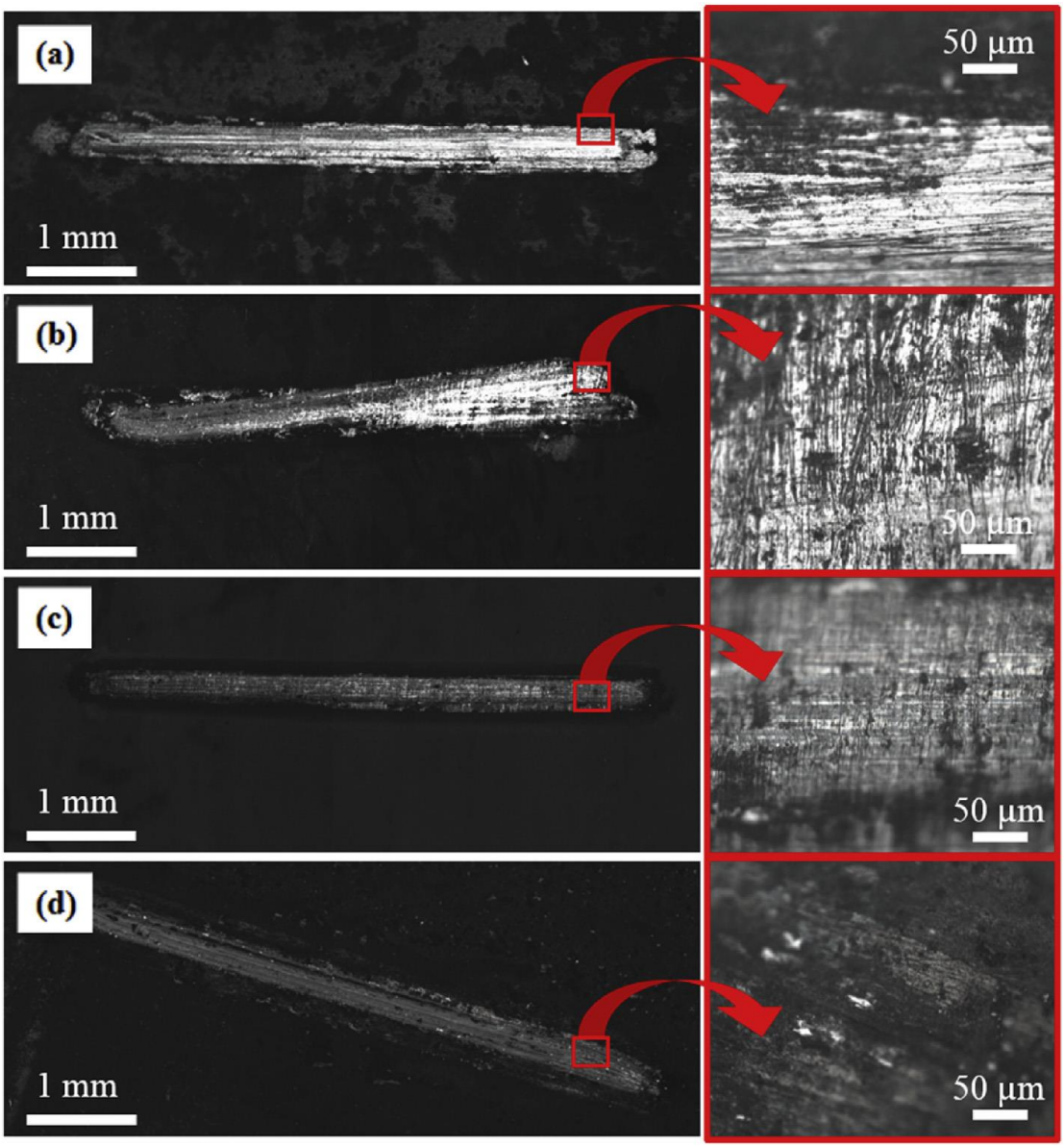

Figure 4.24. Optical micrographs of HA/rGO/Pd coatings thermal treated at 200 (a), 300 (b), 400 (c) and 600 (d) after wear test.

4.10.2 Wear test for HA/GO/Pt

Figure 4.25 showed the friction coefficient and wear loss of the bare substrate, HA/GO/Pt

(before annealing), and annealed HA/GO/Pt coated substrates with respect to annealing temperature. The coefficient of friction is significantly affected by the thermal treatment of HA/GO/Pt coatings. The average COFs of the bare substrate, HA/GO/Pt (before annealing), and annealed HA/GO/Pt coated substrates at 200, 300, 400, and 600 °C were 0.84, 0.75, 0.66, 0.54, 0.57, and 0.59, respectively. By far, the coating annealed at 300 ºC showed a much lower average friction coefficient than the other samples.

The wear rates of the pure substrate, HA/GO/Pt (before annealing), and heat-treated HA/GO/Pt coated substrate at 200, 300, 400, and 600 °C were 3.45, 3.12, 2.23, 2.02, 2.68, and 2.73 mm^3/m, respectively (Figure 4.25). The zirconium substrate had a higher wear rate than the composite coatings, indicating that the composite coatings significantly improved the wear resistance of the Zr substrate. HA/GO/Pt annealed at 300 °C showed a better wear resistance compared with the other samples.

Figure 4.25 (embedded pictures) shows top-down optical micrographs of the Ha/GO/Pt-coated substrate annealed at different temperatures after wear tests. The majority of the debris generated from the coatings were large aggregated particles or chipped flakes. When the annealing temperature was increased from 200 to 300 °C, the composite's wear resistance increased due to an improvement in the adhesion between the substrate and the thin coating. During annealing, the thin film was able to diffuse into the substrate which enhanced the adhesion of the composite coating [220]. The presence of HA in the deposited layer forms a lubricating film with adequate wear resistance on the surface under physiological conditions, due to the hydration of the phosphate anions in the coating, which turn into a large hydration layer. This forms molecular ball-bearings which act as a lubricating layer that enhances the antifriction property of the deposited layer. Other studies

have suggested that GO's uniform dispersion and high surface area ensures that the coating has uniform energy release sites and high fracture toughness, both of which improve its wear resistance. Another study reported that using graphene improved crack deflection, which slowed crack propagation, cracks bridging, and dissipated crack energy. Thus, the formation of a continuous GO layer significantly contributed to the high wear resistance of HA/GO/Pt coatings.

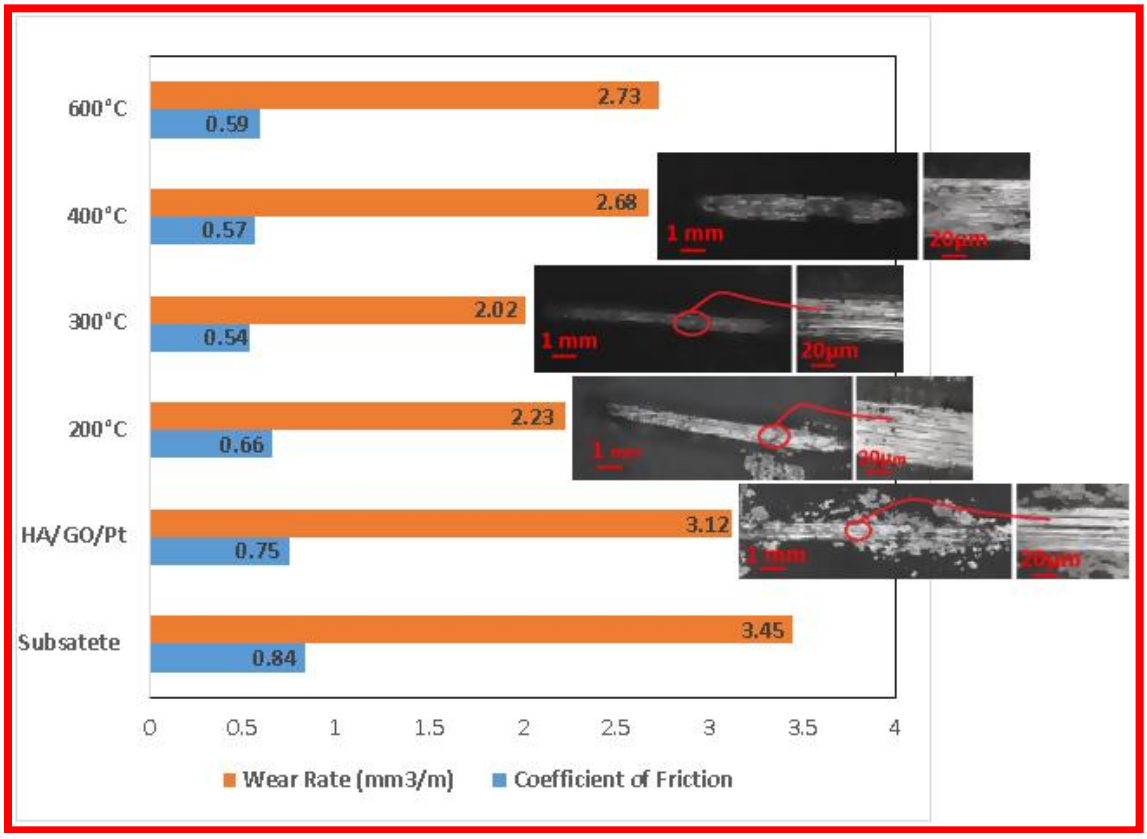

Figure 4.25. The friction coefficients and wear loss of substrate, HA/GO/Pt coating (before annealing), and HA/GO/Pt coatings after heat treatment at different temperatures along with their wear scars microstructure appearance.

Chapter 5 : Conclusion and future work

The tribo-mechanical properties, electrochemical behavior, and biocompatibility of SST/HA/rGO/Pd and Zr/HA/rGO/Pt were investigated in this study. To evaluate the effect of annealing on properties of the composite coatings, the HA/GO/Pt and HA/GO/Pt coated zirconium and SST were heated at different annealing temperatures.

These surface coatings were shown to improve cell attachment and proliferation in biocompatibility experiments, which the HA/rGO/Pd-coated SST 304 showing the highest proliferation, cell attachment, and spreading as indicated by the fluorescence and morphology of the GFP-labelled adenocarcinoma cells. The surface of the uncoated SST 304 surface showed only a small number of cells with the poor spread. The biocompatibility result showed that only a small number of cells with poor distribution was observed on the uncoated zirconium surface and HA/rGO coated Zr substrate showed to have better biocompatibility compared to HA/rGO/Pt. This indicates that Pt may not be a suitable element in the composite for biocompatibility enhancement, although its presence improved the corrosion behavior of the substrate.

The corrosion resistance of the Zr and SST substrates coated with an HA/rGO/Pd and HA/rGO/Pt nanocomposite thin films were higher compared with other samples after being immersed in synthetic serum. These results indicated that the HA/rGO/Pd-coated SST 304 surface notably enhanced the corrosion resistance of the substrate. Moreover, specimens annealed at 200 oC and 300 oC had lower anodic current densities compared with the untreated HA/rGO/Pd coating. A P.E. increase of 99.35% was observed in the coating annealed at 200 oC compared with that of the bare substrate, which suggests that the

HA/rGO/Pd coating could lower the risk of corrosion-induced implant failure. Moreover, the best corrosion result was achieved at 400 °C with Icorr and Ecorr values of 1.521 Na and 379.096 mV, clearly suggesting that using HA/GO/Pt and heat treatment reduces the risk of corrosion-induced failure.

At a normal loading of 4 N, the wear resistance of the HA/rGO/Pd coating annealed at 600 °C had superior performance. The coefficient of friction and wear rate of the HA/GO/Pt-coated substrate annealed at 300 °C were 0.54 and 2.02 mm3/m, respectively, which were greater than the other samples heated at 200, 400, and 600 °C.

Future work

In this thesis, different composite coatings were deposited on Zr and SST substrates. The surface characterization depicted the existence of the coating in the mechanical and electrochemical properties. Further research on the mechanical (nanoindentation and fracture toughness) and surface properties (surface tension and wettability) and the long-term stability of the coatings (adhesion) should be performed in order to evaluate the appropriate performance of the thin film composite coatings in clinical applications. The in vitro characterization performed in this study presented the good performance of the thin film coatings. Although the cell culture test performed in this thesis is considered a good approach to mimic the clinical conditions, an in vivo study would be determining to achieve an insight into the performance of the coating in a complex biological environment. Further in vitro studies would also be helpful, such as dynamic bacterial adhesion assays or dynamic protein adsorption assays and cytotoxicity.

References

[1] Ramakrishna S, Mayer J, Wintermantel E, Leong Kam W. Biomedical applications of polymer-composite materials: a review. Compos Sci Technol 2001; 61:1189–224.

[2] Wise DL. Biomaterials engineering and devices. Berlin: Humana Press; 2000. p. 205–319.

[3] Park JB, Bronzino JD, editors. Biomaterials: principles and applications. Boca Rator, FL: CRC Press; 2003. p. 1–241.

[4] http://www.datamonitor.com, May 2017.

[5] http://www.orthoinfo.aaos.org, April 2017.

[6] Kurtz S, Ong K, Lau E, Mowat F, Halpern M. Projections of primary and revision hip and knee arthroplasty in the United States from 2005 to 2030. J Bone Joint Surg Am 2007; 89:780–5.

[7] Long M, Rack HJ. Titanium alloys in total joint replacement--a materials science perspective. Biomaterials 1998; 19:1621–39.

[8] Wang K. The use of titanium for medical applications in the USA. Mater Sci Eng, A Struct Mater: Prop Microstruct Process 1996; 213:134–7.

[9] Data obtained from http://www.aaos.org/wordhtml/press/arthropl.htm [accessed 1.08.03].

[10] Lawrence Katz J. Anisotropy of Young's modulus of bone. Nature 1980; 283:106–7.

[11] Black J, Hastings GW. Handbook of biomaterials properties. London UK: Chapman and Hall; 1998.

[12] Sumner DR, Turner TM, Igloria R, Urban RM, Galante JO. Functional adaptation

and ingrowth of bone vary as a function of hip implant stiffness. J Biomech 1998; 1:909–17.

[13] Williams DF. On the mechanisms of biocompatibility. Biomaterials 2008; 29:2941–53.

[14] Hallab NJ, Anderson S, Stafford T, Glant T, Jacobs JJ. Lymphocyte responses in patients with total hip arthroplasty. J Orthop Res 2005; 23(2):384–91.

[15] Sargeant A, Goswami T. Hip implants: Paper V. Physiological effects. Mater Des 2006; 27:287–307.

[16] Viceconti M, Muccini R, Bernakiewicz M, Baleani M, Cristofolini L. Large-sliding contact elements accurately predict levels of bone-implant micromotion relevant to osseointegration. J Biomech 2000; 33:1611–8.

[17] Okazaki Yoshimitsu, Gotoh Emiko. Comparison of metal release from various metallic biomaterials in vitro. Biomaterials 2005; 26:11–21.

[18] Wapner KL. Implications of metallic corrosion in total knee arthroplasty. Clin Orthop Relat Res 1991; 271:12–20.

[19] McGregor DB, Baan RA, Partensky C, Rice JM, Wibourn. Evaluation of the carcinogenic risks to humans associated with surgical implants and other foreign bodies - a report of an IARC Monographs Programme Meeting. Eur J Cancer 2000; 307: 13.

[20] Teoh SH. Fatigue of biomaterials: a review. Int J fatigue 2000; 22:825–37.

[21] Niinomi M. Recent metallic materials for biomedical applications. Met Mater Trans 2001; 32A:477–86.

[22] Niinomi M. Recent research and development in titanium alloys for

biomedical applications and healthcare goods. Sci Technol Adv Mater 2003; 4:445–54.

[23] Machara K, Doi K, Matsushita T, Susaki Y. Attenuation of ischemia/reperfusion injury in rats by a caspase inhibitor. Mater Trans 2002; 43:2936–42.

[24] Boehlert C, Niinomi M, Ikedu M. Introduction. Mat Sci Eng C 2005; 25(3):247–52.

[25] Kirby RS, Heard SR, Miller P, Eardley I, Holmes S, Valve J, et al. J Urol 1992; 148(4):1192–5.

[26] Nag S, Banerjee R, Fraser HL. Microstructural evolution and strengthening mechanisms in Ti–Nb–Zr–Ta, Ti–Mo–Zr–Fe and Ti–15Mo biocompatible alloys. Mater Sci Eng C 2005; 25:357–62.

[27] Eisenbarth E, Velten D, Muller M, Thull R, Breme J. Biocompatibility of beta-stabilizing elements of titanium alloys. Biomaterials 2004; 25:5705–13.

[28] Miller PD, Holladay JW. Friction and wear properties of titanium. Wear 1958/59; 2:133–40.

[29] Liang Jr PG, Ferguson Jr ES, Hodge ES. Tissue reaction in rabbit muscle exposed to metallic implants. J Biomed Mater Res 1967; 1:135–49.

[30] Geetha M, Singh AK, Muraleedharan K, Gogia AK, Asokamani R. Effect of thermomechanical processing on microstructure of a Ti-13Nb-13Zr alloy. J Alloys Compd 2001; 329:214–23.

[31] Tang X, Ahmed T, Rack HJ. Phase transformations in Ti-Nb-Ta and Ti-Nb-Ta-Zr alloys. J Mater Sci 2000; 35:1805–11.

[32] Geetha M, Singh AK, Gogia AK, Asokamani R. Effect of thermomechanical processing on evolution of various phases in Ti-Nb-Zr alloys. J. Alloys Compd. 2004; 384:131–51.

[33] Sakaguchi N, Niinomi M, Akahori T, Takeda J, Toda H. Relationships between tensile deformation behavior and microstructure in Ti–Nb–Ta–Zr system alloys. Mater Sci Eng C 2005; 25:363–9.

[34] Kuroda D, Kawasaki H, Hiromoto S, Hanawa, Kuroda S, Kobayashi M, et al. Titanium 2003 science and technology. Wenham, Germany: Wiley-VCH Verlag, GMBH and Co. K GaA; 2003. p. 3174.

[35] Sakaguchi Nobuhito, Niinomi Mitsuo, Akahori Toshikazu, Takeda Junji, Toda Hiroyuki. Effect of Ta content on mechanical properties of Ti-30Nb-XTa-5Zr. Mater Sci Eng C 2005; 25:370–6.

[36] Qazi J, Marquart B, Allard LF, Rack HJ. Phase transformations in Ti–35Nb–7Zr–5Ta–(0.06–0.68) O alloys. Mater Sci Eng C 2005; 25:389–97.

[37] Qazi J, Rack HJ. Titanium 2003 science and technology, vol. 1. Weinhem, Germany: Wiley-VCH Verlag, GMBH and Co. KGaA; 2003. p. 651. 422 M. Geetha et al. / Progress in Materials Science 54 (2009) 397–425

[38] Song Y, Xu DS, Yang R, Li D, Wu WT, Guo ZX, et al. Theoretical study of the effects of alloying elements on the strength and modulus of β-type bio-titanium alloys. Mater Sci Eng A 1999; 260:269–74.

[39] Hanada S, Ozaki T, Watanabe Takahashi S, Yoshimi K, Abumiya T, et al. Composition dependence of Young's modulus in beta titanium binary alloys. Mater Sci Forum 2003; 426–432:3103–8.

[40] Li SJ, Yang R, Li S, Hao YL, Cui YY, Niinomi M, et al. Wear characteristics of Ti–Nb–Ta–Zr and Ti–6Al–4V alloys for biomedical applications. Wear 2004; 257:869–76.

[41] Niinomi M. Mechanical properties of biomedical titanium alloys. Mater Sci Eng A 1998; 243:231–6.

[42] Mishra K, Davidson JA, Poggie RA, Kovacs P, Fitzgerald TJ. In: Lemons JE, editor. The material and biological issues ASTM STP, vol. 1272. West Conshohocken, PA: ASTM; 1996. p. 96–105.

[43] Wang K, Gustavson L, Dumbleton J. Beta titanium in the 1990s. Warrendale, Pennsylvania: The Mineral, Metals and Materials Society; 1993. p. 2697–704.

[44] Steinemann SG, Mausli PA, Szmukler-Moncler S, Semlitsch M, Pohler O, Hintermann HE, et al. Beta titanium in the 1990s. Warrendale, Pennsylvania: The Mineral, Metals and Materials Society; 1993. p. 2689–96.

[45] Fanning JC. TIMETAL21SRx. Titanium 95' science and technology; 1996. p. 1800–7.

[46] Mishra AK, Davidson JA, Kovacs P, Poggie RA. Beta titanium in the 1990s. Warrendale, Pennsylvania: The Mineral, Metals and Materials Society; 1993. p. 61–6.

[47] Kuroda D, Niinomi M, Akahori T, Fukui H, Suzuki A, Hasegawa T, et al. Structural biomaterials for the 21st century. In: Niinomi M, Okabe T, Taleff EM, Lesuer DR, Lippard HE, editors. TMS, The Minerals Metals and Materials Society; 2001.

[48] Akahori T, Niinomi M, Fukui H, Suzuki A, Hattori Y, Niwa S, et al. Titanium 2003 science and technology. Weinhem, Germany: Wiley VCH Verlag, GMBH and Co. KGaA; 2003.

[49] Ahmed T, Long M, Silverstri, Ruiz C, Rack HJ. In: Bania PJ, Evans WJ, Flower HM, editors. Titanium 95: science and technology. London, UK: IoM; 1995. p.

1760–7.

[50] Qazi JI, Tsakiris V, Marquardt B, Rack HJ. Titanium 2003 science and technology. Weinhem, Germany: Wiley VCH Verlag, GMBH and Co. KGaA; 2003.

[51] Taneich K, Taira M, Sukedai E, Narushima T, Iguchi Y, Ouchi C, et al. Alloy design and property evaluation of new β type titanium alloy with excellent cold workability and biocompatibility. ISIJ Int 2006; 46:292–301.

[52] Guillemot F, Prima F, Barellie R, Gordin D, Gloriant, Ansel D, et al. Titanium 2003 science and technology. Weinheim, Germany: Weiley-VCH Verlag, GMBH and Co. KGaA; 2003.

[53] Rack HJ, Qazi JI. Titanium Alloys for Biomedical Applications. Mater Sci Eng C 2006; 26:1269–77.

[54] Ramakrishna, S., et al., Biomedical applications of polymer-composite materials: a review. Composites science and technology, 2001. 61(9): p. 1189-1224.

[55] Pompe, W., et al., Functionally graded materials for biomedical applications. Materials Science and Engineering: A, 2003. 362(1): p. 40-60.

[56] Williams, D.F., On the mechanisms of biocompatibility. Biomaterials, 2008. 29(20): p. 2941-2953.

[57] Williams, R.L., S.A. Brown, and K. Merritt, Electrochemical studies on the influence of proteins on the corrosion of implant alloys. Biomaterials, 1988. 9(2): p. 181-186.

[58] Blac, J., Systemic effects of biomaterials. Biomaterials, 1984. 5(1): p. 11-18.

[59] Liu, Y., et al., Tailoring of the dopamine coated surface with VEGF loaded heparin/poly-l-lysine particles for anticoagulation and accelerate in situ

endothelialization. Journal of Biomedical Materials Research Part A, 2015. 103(6): p. 2024-2034.

[60] Wang, H., et al., Biofunctionalization of titanium surface with multilayer films modified by heparin-VEGF-fibronectin complex to improve endothelial cell proliferation and blood compatibility. Journal of Biomedical Materials Research Part A, 2013. 101(2): p. 413-420.

[61] Leng, Y., et al., Fabrication of Ti–O/Ti–N duplex coatings on biomedical titanium alloys by metal plasma immersion ion implantation and reactive plasma nitriding/oxidation. Surface and Coatings Technology, 2001. 138(2): p. 296-300.

[62] Finley, M.J., et al., Diminished adhesion and activation of platelets and neutrophils with CD47 functionalized blood contacting surfaces. Biomaterials, 2012. 33(24): p. 5803-5811.

[63] P. K. Ross, M Dominiak, T. Gedrange, U. U. Botzenhart, Zirconium: The material of the future in modern implantology, Adv Clin Exp Med. 2017;26(3):533–537.

[64] Dubruille JH, Viguier E, Le Naour G, Dubruille MT, Auriol M, Le Charpentier Y., Evaluation of combinations of titanium, zirconia, and alumina implants with 2 bone fillers in the dog. Int J Oral Maxillofac Implants. 1999;14:271–277.

[65] Stanic V, Aldini NN, Fini M, et al. Osteointegration of bioactive glass-coated zirconia in healthy bone: An in vivo evaluation. Biomaterials. 2002;23:3833–3841.

[66] Zhang, D., et al., Materials Chemistry B. 2014.

[67] Cengiz, S. and Y. Gencer, The characterization of the oxide based coating synthesized on pure zirconium by plasma electrolytic oxidation. Surface and Coatings Technology, 2014. 242: p. 132-140.

[68] Lin, K., C. Wu, and J. Chang, Advances in synthesis of calcium phosphate crystals with controlled size and shape. Acta biomaterialia, 2014. 10(10): p. 4071-4102.

[69] Novoselov, K.S., et al., Electric field effect in atomically thin carbon films. Science, 2004. 306(5696): p. 666-669.

[70] Moussy, F. Biomaterials for the developing world. J Biomed Mater Res A 94.4 (2010): 1001-1003.

[71] Cui, C. Y., et al. Microstructure and corrosion behavior of the AISI 304 stainless steel after Nd: YAG pulsed laser surface melting. Surf Coat Tech 206.6 (2011): 1146-1154.

[72] Fu, T., et al. Mechanical properties of DLC coating sputter deposited on surface nanocrystallized 304 stainless steel. Surf Coat Tech 207 (2012): 555-564.

[73] Gonçalves, Paulo RG, et al. Sn (1− x) LaxO_2 thin films deposited on AISI 304 stainless steel substrates. Ceram Int 40.8 (2014): 12359-12366.

[74] Chen, CC, Wern-Dare J, and Chung-Kwei L. Large-area TiO_2 nanotube dye-sensitized solar cells using thermal-sprayed Ti layers on stainless steel. Ceram Int 40.2 (2014): 3221-3226.

[75] Lawal, Abdulazeez T. Synthesis and utilisation of graphene for fabrication of electrochemical sensors. Talanta 131 (2015): 424-443.

[76] Li, J. H., et al. Ultra-light, compressible and fire-resistant graphene aerogel as a highly efficient and recyclable absorbent for organic liquids. (2014).

[77] Kong, X-K, Chang-Le C, and Qian-Wang C. Doped graphene for metal-free catalysis. Chem Soc Rev 43.8 (2014): 2841-2857.

[78] Bonaccorso, F, et al. Graphene, related two-dimensional crystals, and hybrid systems

for energy conversion and storage. Science 347.6217 (2015): 1246501.

[79] Yang, Yuqi, et al. Graphene based materials for biomedical applications. Mater Today 16.10 (2013): 365-373.

[80] Han, Z J, et al. Carbon nanostructures for hard tissue engineering. RSC Adv 3.28 (2013): 11058-11072.

[81] Liu Y, Jing H, and Hua L. Nanostructural characteristics of vacuum cold-sprayed hydroxyapatite/graphene-nanosheet coatings for biomedical applications. J Therm Spray Techn 23.7 (2014): 1149-1156.

[82] Li, M, et al. In situ synthesis and biocompatibility of nano hydroxyapatite on pristine and chitosan functionalized graphene oxide. J Mater Chem B 1.4 (2013): 475-484.

[83] Zhao, Y, et al. Microstructure and anisotropic mechanical properties of graphene nanoplatelet toughened biphasic calcium phosphate composite. Ceram Inter 39.7 (2013): 7627-7634.

[84] Zhang, L, et al. A tough graphene nanosheet/hydroxyapatite composite with improved in vitro biocompatibility. Carbon 61 (2013): 105-115.

[85] Zhu, J, et al. Spark plasma sintered hydroxyapatite/graphite nanosheet and hydroxyapatite/multiwalled carbon nanotube composites: mechanical and in vitro cellular properties. Adv Eng Mater 13.4 (2011): 336-341.

[86] Sekine, H. Illustrated encyclopedia and dictionary of dental science. 1989: 1701.

[87] Merritt, K, Brown, S. Effect of proteins and pH on fretting corrosion and metal ion release. J Biomed Mater Res A 22.2 (1988): 111-120.

[88] Williams, RL., Brown, SA, Merritt, K. Electrochemical studies on the influence of proteins on the corrosion of implant alloys. Biomaterials 9.2 (1988): 181-186.

[89] Hench, L. L., E. C. Ethridge. Biomaterials: the interfacial problem. Adv Biomed Eng 5 (1975): 35-150.

[90] Wataha, JC., Shor, K. Palladium alloys for biomedical devices. Expert review of medical devices 7.4 (2010): 489-501.

[91] Jiang, X, et al. Palladium as a substrate for self-assembled monolayers used in biotechnology. Anal Chem 76.20 (2004): 6116-6121.

[92] Abu-Surrah, AS., et al. ew palladium (II) complexes bearing pyrazole-based Schiff base ligands: Synthesis, characterization and cytotoxicity. Eur J Med Chem 45.2 (2010): 471-475.

[93] Divsalar, A., et al. Spectroscopic and cytotoxic studies of the novel designed palladium (II) complexes: β-Lactoglobulin and K562 as the targets. Int J Bio Macromol 40.4 (2007): 381-386.

[94] Gao, En-jun, et al. Synthesis, characterization, interaction with DNA and cytotoxicity in vitro of the complexes [M(dmphen)(CO3)]·H2O [M= Pt (II), Pd (II)]. Eur J Med Chem 45.1 (2010): 311-316.

[95] Geeta, B., et al. Binuclear cobalt(II), nickel(II), copper(II), and palladium(II) complexes of a new Schiff-base as ligand: Synthesis, structural characterization, and antibacterial activity. Spectrochim Acta A 77.4 (2010): 911-915.

[96] Guerra, Wendell, et al. Synthesis, characterization, and antibacterial activity of three palladium (II) complexes of tetracyclines. J Inorg Biochem 99.12 (2005): 2348-2354.

[97] Polivkova, M., et al. Antibacterial properties of palladium nanostructures sputtered on polyethylene naphthalate. RSC Adv 5.90 (2015): 73767-73774.

[98] Anselme, K, Bigerelle, M. Effect of a gold–palladium coating on the long-term adhesion of human osteoblasts on biocompatible metallic materials. Surf Coat Tech 200.22 (2006): 6325-6330.

[99] Tang, J, Zuo, Y. Study on corrosion resistance of palladium films on 316L stainless steel by electroplating and electroless plating. Corros Sci 50.10 (2008): 2873-2878.

[100] He G, Hagiwara M. Ti alloy design strategy for biomedical applications. Mater Sci Eng C 2006; 26:14–9.

[101] Charnley J, Cupic Z. The nine and ten year results of the low-friction arthroplasty of the hip. Clin Orthop 1973; 95:9–25.

[102] Malchau H, Herberts P. Revision and re-revision rate n THR: a revision-risk study of 1,48,359 primary operations. In: Scientific exhibition presented at the 65th annual meeting of the American academy of orthopaedic surgeons, New Orleans, USA; February 1998. p. 19–23.

[103] Harty M. Symposium on surface replacement arthroplasty of the hip: anatomic considerations. Orthop Clin North Am 1982; 13:667–79.

[104] Scholes SC, Unswrth A, Goldsmith AAJ. A frictional study of total hip joint replacements. Phys Med Biol 2000; 45:3721–35.

[105] Margaret A, McGee Donald W, Howie, Costi Kerry, Haynes David R, Corinna I, et al. Wear 2000; 241:158–65.

[106] Adrese M Kandahari, XinLin Yang, Kevin A Laroche, Abhijit S Dighe, Dongfeng Pan, Quanjun Cui, A review of UHMWPE wear-induced Osteolysis: the role for early detection of the immune response, 16014 (2016).

[107] Tipper JL, Firkins PJ, Ingham E, Fischer J, Stone MH, Farrar R. Quantitative

analysis of the wear and wear debris from low and high carbon content cobalt chrome alloys used in metal on metal total hip replacements. J Mater Sci: Mater Med 1999; 10:353–62.

[108] Germain MA, Hzyyon A, Williams S, Mathews JB, Stone MH, Fisher J, et al. Comparison of the cytotoxicity of clinically relevant cobalt–chromium and alumina ceramic wear particles in vitro. Biomaterials 2003; 24:469–79.

[109] Chevalier J. What future for zirconia as a biomaterial?. Biomaterials 2006; 27:535–43.

[110] Watters EPJ, Spedding PL, Duffy JM, Spedding RL. Wear of artificial hip joint material. Chem Eng J 2005; 112:137–44.

[111] OH, J.C., Yun, E. & Lee, S. Correlation of microstructure with the hardness and wear resistance of (TiC,SiC)/Ti-6Al-4V surface composites fabricated by high-energy electron-beam irradiation. Metall and Mat Trans A (2004) 35: 525. [112] Long Marc, Rack HJ. Mater Sci Eng C 2005; 25:382–8.

[113] Choubey A, Basu B, Balasubramaniam R. Tribological behaviour of Ti-based alloys in simulated body fluid solution at fretting contacts. Mater Sci Eng A 2004; 379:234–9.

[114] Long M, Qazi JI, Rack HJ. Titanium 2003 science and technology. Weinhem, Germany: Wiley VCH Verlag, GMBH and Co. KGaA; 2003. p. 1691–8.

[115] Peterson MB, Calabrese SJ, Stup B. NTIS ADA 124248. US, Department of Commerce; 1992.

[116] Peterson MB, Li SZ, Jiang XX, Calabrese SJ. In: Proceedings 16th Leeds-Lyon symposium, Villeurbanne, France; 1989.

[117] Peterson MB, Li SZ, Jiang XX. China Program. NSF Grant INT. 8617231; 1989.

[118] Jones DA. Principles and prevention of corrosion, 2nd Ed., vol. 5. New Jersey: Prentice Hall; 1996. p. 75–115.

[1193] Clerc CO, Jedwab DW, Mayer PJ, Thompson, Stinson JS. Assessment of wrought ASTM F1058 cobalt alloy properties for permanent surgical implants. J Biomed Mater Res 1997; 38:229–34.

[120] Mueller HJ, Greener EH. Polarization studies of surgical materials in Ringer's solution. J Biomed Mater Res 1970; 4:29–41.

[121] Fukumoto S, Tsubakino H, Inoue S, Liu L, Terasawa M, Mitamura T. Surface modification of titanium by nitrogen ion implantation. Mater Sci Eng 1999; A263:205–9.

[122] Liu X, Chu PK, Ding CX. Surface modification of titanium, titanium alloys, and related materials for biomedical applications. Mater Sci Eng R 2004; 47:49–121. M. Geetha et al. / Progress in Materials Science 54 (2009) 397–425 423.

[123] American Academy of Orthopaedic surgeons. In: Survey presented at the orthopaedic research society annual meeting, Orlando, Fl; February 1995.

[124] Alves Jr, Neto Guerra, Morais GHS, da Silva CF, Hajek V. Nitriding of titanium disks and industrial dental implants using hollow cathode discharge. Surf Coat Technol 2005; 194:196–204.

[125] Sundararajan T, Kamachi Mudali U, Rajeswari S, Subbaiyan M. Electrochemical studies on nitrogen ion implanted Ti6Al4V alloy. Anti Corros Meth Mater 1998; 45:162–6.

[126] Hintermann. US Patent, No. 4, 6,87,487; August 1987.

[127] Thair L, Kamachi Mudali U, Bhuvaneswaran N, Nair KGM, Asokamani R, Raj Baldev. Nitrogen ion implantation and in vitro corrosion behavior of as-cast Ti–6Al–7Nb alloy. Corros Sci 2002; 44:2439–57.

[128] Thair L, Kamachi Mudali U, Rajagopalan S, Asokamani R, Raj Baldev. Surface characterization of passive film formed on nitrogen ion implanted Ti–6Al–4V and Ti–6Al–7Nb alloys using SIMS. Corros Sci 2003; 45:1951–67.

[129] Robert SM, Heinz W, Rolf S, Manfred S. New surface modification for Ti-6Al-7Nb alloy: oxygen diffusion hardening (ODH). Biomaterials 1991; 12(2):125.

[130] Manivasagam G, Kamachi Mudali U, Asokamani R, Baldev Raj. In: First Asia Pacific conference and sixth national convention on corrosion, organized by NACE, India, November, vol. 145; 2001.

[131] Geetha M, Kamachi MU, Asokamani R, Raj B. Microstructural and corrosion evaluation of laser surface nitrided Ti-13Nb-13Zr alloy. Surf Eng 2004; 20(7):68–74.

[132] Prevey PS, Loftus EF, Hornbach DJ. Application of low plasticity burnishing (LPB) to improve the fatigue performance of Ti-6Al-4V femoral hip stems. J ASTM Int 2006:3.

[133] Wen MJ, Ma, Andrew RJ, Mason MS, Phil MJ, Avi B, et al. DLC coatings: effects of physical and chemical properties on biological response. Biomaterials 2007; 28(9):1620–8.

[134] Kim S, Lee JB, Koak JY, Heo SJ, Lee KR, Cho LR, et al. An abutment screw loosening study of a Diamond Like Carbon-coated CP titanium implant. J Oral Rehab 2005; 32:346–50.

[135] Roy RK, Lee KR. Biomedical applications of diamond-like carbon coatings: A review. J Biomed Mater Res B Appl Biomater 2007.

[136] Mohanty M, Anilkumar TV, Mohanan PV, Muraleedharan CV, Bhuvanashewar GS, Derangere F, et al. Long term tissue response to titanium coated with diamond like carbon. Biomol Eng 2002; 19:125.

[137] Dowling DP, Kola PV, Donnelly K, Kelly TC, Brumitt K, Lloyd L, et al. Evaluation of diamond-like carbon-coated orthopaedic implants. Diam Relat Mater 1997; 6:390–3.

[138] Brizuela M, Garcia Luis A, Viviente JL, Braceras I, Onate JL. Tribological study of lubricious DLC biocompatible coatings. J Mat Sci–Mat Med 2002; 13:1129–33.

[139] Zinger O, Anselme K, Denzer A, Habersetzer P, Wieland M, Jeanfils J, et al. Time-dependent morphology and adhesion of osteoblastic cells on titanium model surfaces featuring scale-resolved topography. Biomaterials 2004; 25:2695–711.

[140] Brunette DM, Ratkay J, Chehroudi B. The bone-biomaterial interface. Toronto: University of Toronto Press; 1991. p. 49–61.

[141] Boyan B, Hummert T, Kieswetter K, Schraub D, Dean D, Schwartz Z. Effect of titanium surface characteristics on chondrocytes and osteoblasts in vitro. Cells Mater 1995; 5:323–35.

[142] Jayaraman M, Meyer U, Buhner M, Joos U, Wiesmann H-P. Influence of titanium surfaces on attachment of osteoblast-like cells in vitro. Biomaterials 2004; 25:625–31.

[143] Pilliar RM. Overview of surface variability of metallic endosseous dental implants: textured and porous surface-structured designs. Implant Dent 1998; 7:305–14.

[144] Wennerberg A, Hallgren C, Johansson C, Daneli S. A histomorphometric evaluation of screw-shaped implants each prepared with two surface roughnesses. Clin Oral Implant Res 1998; 9:11–9.

[145] Martin JY, Schwartz Z, Hummert TW, et al. Effect of titanium surface roughness on proliferation, differentiation, and protein synthesis of human osteoblast-like cells (MG63). Clin Oral Implant Res 1995; 29:389–93.

[146] Buser D, Schenk RK, Stienemann S, Fiorelini JP, Fox CH, Stich H. Influence of surface characteristics on bone integration of titanium implants. A histomorphometric study in miniature pigs. J Biomed Mater Res 1991; 25:889–902.

[147] Mac Donald DE, Rapuano BE, Deo N, Stranick M, Somasundaram P, Boskey AL, et al. Thermal and chemical modification of titanium-aluminum-vanadium implant materials: effects on surface properties, glycoprotein adsorption, and MG63 cell attachment. Biomaterials 2004; 25:3135–46.

[148] Hulbert SF, Cooke FW, Klawitter JJ, Rub Leonard, Saver BW, Moyle DD, et al. Attachment of prostheses to the musculoskeletal system by tissue ingrowth and mechanical interlocking. J Biomed Mater Res 1973; 7:1–23.

[149] Sauer BW, Weinstein AM, Klawitter JJ, Hulbert SF, Leonard RB, Bagwell JG. The role of porous polymeric materials in prosthesis attachment. J Biomed Mater Res 1974; 8:145–53.

[150] Roderic L. Composite biomaterials. In: Bronzino JD, editor. The biomedical engineering handbook. Boca Raton, FL: CRC Press; 1995. p. 309–14.

[151] Bojescul JA, Xenos JS, Callaghan JJ, Savory CG. Results of porous-coated

anatomic total hip arthroplasty without cement at fifteen years: a concise follow-up of a previous report. J Bone Joint Surg A 2003; 85:1079–83.

[152] Stangl R, Pries A, Loos B, Muller M, Erben RG. Influence of pores created by laser superfinishing on osseointegration of titanium alloy implants. J Biomed Mater Res 2004; 69A:444–53.

[153] Hulbert SF, Young FA, Mathews RS, Klawitter JJ, Talbert CD, Stelling FH. Potential of ceramic materials as permanently implantable skeletal prostheses. J Biomed Mater Res 1970; 4:433–56.

[154] Li J, Liao H, Fartash B, Hermansson L, Johnsson. Surface-dimpled commercially pure titanium implant and bone ingrowth. Biomaterials 1997; 18:691–6.

[155] Gotz HE, Muller M, Emmel A, Holzwarth U, Erben RG, Stangl R. Effect of surface finish on the osseointegration of laser-treated titanium alloy implants. Biomaterials 2005; 25:4057–64.

[156] Vamsikrishna B, Bose S, Bandoyopadhyay A. Laser processing of bioactive tricalcium phosphate coating on titanium for load-bearing implants. Actabiomater 2007.

[157] Li SJ, Yang R, Ninomi M, Hao YL, Cui YY. Formation and growth of calcium phosphate on the surface of oxidized Ti-29Nb-13Ta-4.6Zr alloy. Biomaterials 2004; 25:2525–32.

[158] Soballe K, Hanse ES, Brockstedt-Ramussen H, Bunger C. Hydroxyapatite coating converts fibrous tissue to bone around loaded implants. J Bone Joint Surg Am 1993; 75-B:270–8.

[159] Greesink RGT, Hoefnagels NHM. Six-year results of hydroxyapatite-coated total

hip replacement. J Bone Joint Surg Am 1995; 77-B:534–47.

[160] Dhert WJA, Klein CPAT, Jansen JA. A histological and histomorphometrical investigation of fluorapatite, magnesiumwhitlockite, and hydroxylapatite plasma‐sprayed coatings in goats. J Biomed Mater Res 1993; 27:127–38.

[161] Dhert WJA, Thomsen P, Blomgren AK, Esposito M, Ericson LE, Verbout AJ. Integration of press-fit implants in cortical bone: A study on interface kinetics. J Biomed Mater Res 1998; 41:574–83.

[162] MacDonald DE, Betts F, Doty SB, Boskey AL. A methodological study for the analysis of apatite-coated dental implants retrieved from humans. Ann Periodontol 2000; 5:175–84.

[163] MacDonald DE, Betts F, Stranick M, Doty S, Boskey AL. Physicochemical study of plasma-sprayed hydroxyapatite-coated implants in humans. J Biomed Mater Res 2001; 54:480–90.

[164] Li L-H, Kong Y-M, Kim H-W, Kim Y-W, Kim H-E, Heo S-J, et al. Improved biological performance of Ti implants due to surface modification by micro-arc oxidation. Biomaterials 2004; 25:2867–75.

[165] Kim HM, Miyaji F, Kokubo T, Nakamura T. Preparation of bioactive Ti and its alloys via simple chemical surface treatment. J Biomed Mater Res 1996; 32:409-17.

[166] Webster TJ, Ellison K, Price RL, Karen M, Haberstroh. Increased osteoblast function on nanostructured materials due to novel surface roughness properties. Mater Sci Forum 2003; 426–432:3127–32.

[167] Wang L, DY Li. Mechanical, electrochemical and tribological properties of nanocrystalline surface of brass produced by sandblasting and annealing. Surf Coat Technol 2003; 167:188–96.

[168] Webster TJ, Siegel RW, Bizos R. Enhanced functions of osteoblasts on nanophase ceramics. Biomaterials 2000; 21:1803–10.

[169] Luke G, Gutwein, Webster Thomas J. Increased viable osteoblast density in the presence of nanophase compared to conventional alumina and titania particles. Biomaterials 2004; 25:4175–83.

[170] Niinomi M, Kuroda D, Fukunaga KI, Fukui H, Kato Y, Yashiro, et al. In: Gorynin IV, Ushkov SS, editors. Science and technology, proceedings of the IX world conference on titanium, St. Petersburg Russia, CRISM, Promety, vol. I– III; 1999. 223.

[171] WS. Hummers Jr., RE. Offeman, Preparation of graphitic oxide, J. Am. Chem. Soc. 1958; 80:1339-1339.

[172] S. Ranganatha, T.V. Venkatesha, Fabrication and electrochemical characterization of Znehalloysite nanotubes composite coatings, RSC Adv. 2014; 4:31230-31238.

[173] Yuan-Hsiang Yu, et al., High-performance polystyrene/graphene-based nanocomposites with excellent anti-corrosion properties, Polym. Chem. 2014; 5:535-550.

[174] Yi Liu, Jing Huang, Hua Li, Synthesis of hydroxyapatiteereduced graphite oxide nanocomposites for biomedical applications: oriented nucleation and epitaxial growth of hydroxyapatite, J. Mater. Chem. B 2013; 1:1826-1834.

[175] Mercedes Vila, et al., Macroporous solegel hydroxyapatite moulding via

confinement into shaped acrylateeacrylamide copolymers, J. Eur. Ceram. Soc. 2012; 32:2121-2127.

[176] Zhongli Shi, et al., Size effect of hydroxyapatite nanoparticles on proliferation and apoptosis of osteoblast-like cells, Acta Biomater. 2009; 5:338-345.

[177] Sepidar Sayyar, et al., Synthesis and characterization of covalently linked graphene/chitosan composites, JOM 2016; 68:384-390.

[178] V. Geetha, T. Gomathi, P.N. Sudha, Preparation and characterization of Graphene-grafted-chitosan/hydroxyapatite composite, J. Chem. Pharmaceut. Res. 2015; 7:871-876.

[179] Ming Li, et al., In situ synthesis and biocompatibility of nano hydroxyapatite on pristine and chitosan functionalized graphene oxide, J. Mater. Chem. B 2013: 1:475-484.

[180] Karina Bustos-Ramírez, et al., Covalently bonded chitosan on graphene oxide via redox reaction, Materials 2013; 6:911-926.

[181] D. Gopi, S. Nithiya, E. Shinyjoy, L. Kavitha, Spectrochim., Spectroscopic investigation on formation and growth of mineralized nanohydroxyapatite for bone tissue engineering applications, Spectrochim. Acta A Mol. Biomol. Spectrosc. 2012; 92:194-200.

[182] A.J. Salinas, et al., Substitutions of cerium, gallium and zinc in ordered mesoporous bioactive glasses, Acta Biomater. 2011; 7:3452-3458.

[183] Ana Jankovic, et al., Bioactive hydroxyapatite/graphene composite coating and its corrosion stability in simulated body fluid, J. Alloys Compd. 2015; 624:148-157.

[184] M.R. Nikpour, S.M. Rabiee, M. Jahanshahi, Synthesis and characterization of

hydroxyapatite/chitosan nanocomposite materials for medical engineering applications, Compos. B Eng. 2012; 43:1881-1886.

[185] S. Baradaran, et al., Mechanical properties and biomedical applications of a nanotube hydroxyapatite-reduced graphene oxide composite, Carbon 2014; 69:32-45.

[186] Gururaj M. Neelgund, Aderemi Oki, Zhiping Luo, In situ deposition of hydroxyapatite on graphene nanosheets, Mater. Res. Bull. 2013; 48:175-179.

[187] Ming Li, et al., Electrophoretic deposition and electrochemical behavior of novel graphene oxide-hyaluronic acid-hydroxyapatite nanocomposite coatings, Appl. Surf. Sci. 2013; 284:804-810.

[188] Cheng-Chei Wu, et al., FT-IR and XRD investigations on sintered fluoridated hydroxyapatite composites, J. Mol. Struct. 2010; 979:72-76.

[189] Jose Reyes-Gasga, et al., XRD and FTIR crystallinity indices in sound human tooth enamel and synthetic hydroxyapatite, Mater. Sci. Eng. C 2013; 33:4568-4574.

[190] Peichao Lian, et al., Large reversible capacity of high quality graphene sheets as an anode material for lithium-ion batteries, Electrochim. Acta 55 2010; 12:3909-3914.

[191] Ana Jankovi_c, et al., Graphene-based antibacterial composite coatings electrodeposited on titanium for biomedical applications, Prog. Org. Coating 2015; 83:1-10.

[192] Marie Kalbacova, et al., Graphene substrates promote adherence of human osteoblasts and mesenchymal stromal cells, Carbon 2010; 48:4323-4329.

[193] Y. Liu, Z. Dang, Y. Wang, J. Huang, H. Li, Hydroxyapatite/graphene-nanosheet

composite coatings deposited by vacuum cold spraying for biomedical applications: inherited nanostructures and enhanced properties, Carbon 2014; 67:250-259.

[194] Y.W. Zhu, S. Murali, W.W. Cai, X.S. Li, J.W. Suk, J.R. Potts, R.S. Ruoff, Graphene and graphene oxide: synthesis, properties, and applications, Adv. Mater. 2010; 22:5226.

[195] A. Jankovic, S. Erakovic, M. Vukašinovic-Sekulic, V. Miškovic-Stankovic, S.J. Park, K.Y. Rhee, Graphene-based antibacterial composite coatings electrodeposited on titanium for biomedical applications. Prog. Org. Coat. 2015; 83.

[196] A. Jankovic, S. Erakovic, M. Mitric, I.Z. Matic, Z.D. Juranic, G.C.P. Tsui, C.Y. Tang, V. Miškovic-Stankovic, K.Y. Rhee, S.J. Park, Bioactive hydroxyapatite/graphene composite coating and its corrosion stability in simulated body fluid. J. Alloys Compd. 2015; 624:148.

[197] T. Szatkowski, A. Kolodziejczak-Radzimska, J. Zdarta, K. Szwarc-Rzepka, D. Paukszta, M. Wysokowski, H. Ehrlich, T. Jesionowski, Synthesis and characterization of hydroxyapatite/chitosan composites. Physicochem. Prob. Miner. Process. 2015; 51:575.

[198] F.A. López, A.L.R. Mercê, F.J. Alguacil, A. López-Delgado, A kinetic study on the thermal behaviour of chitosan. J. Therm. Anal. Calorim. 2008; 91:633.

[199] L. Cordero-Arias, S. Cabanas-Polo, H. Gao, J. Gilabert, E. Sanchez, J.A. Roether, D. W. Schubert, S. Virtanene, A.R. Boccaccini, Electrophoretic deposition of nanostructured-TiO 2/chitosan composite coatings on stainless steel. RSC Adv.

2013; 3:11247.

[200] S. Tang, B. Tian, Y.J. Guo, Z.A. Zhu, Y.P. Guo. Chitosan/carbonated hydroxyapatite composite coatings: fabrication, structure and biocompatibility. Surf. Coat. Technol. 2014; 251: 210.

[201] F. Gebhardt, S. Seuss, M.C. Turhan, H. Hornberger, S. Virtanen, A.R. Boccaccini, Characterization of electrophoretic chitosan coatings on stainless steel. Mater. Lett. 2012; 66: 302.

[202] J. Reyes-Gasga, E.L. Martinez-Pineiro, G. Rodriguez-Alvarez, G.E. Tiznado-Orozco, R. Garcia-Garcia, E.F. Bres, XRD and FTIR crystallinity indices in sound human tooth enamel and synthetic hydroxyapatite. Mater. Sci. Eng. C 2013; 33:4568.

[203] Debrupa L, Sanat G, Arvind A, Carbon nanotube reinforced hydroxyapatite composite for orthopedic application: a review, Mater. Sci. Eng. C 2012; 32:1727-1758.

[204] Thomas J. Webster, et al., Nano-biotechnology: carbon nanofibres as improved neural and orthopaedic implants, Nanotechnology 2003; 15:48.

[205] N. Ribeiro, S.R. Sousa, F.J. Monteiro, Influence of crystallite size of nanophased hydroxyapatite on fibronectin and osteonectin adsorption and on MC3T3-E1 osteoblast adhesion and morphology, J. Colloid Interface Sci. 2010; 351: 398-406.

[206] Ming Li, et al., Electrophoretic deposition and electrochemical behavior of novel graphene oxide-hyaluronic acid-hydroxyapatite nanocomposite coatings, Appl. Surf. Sci. 2013; 284:804-810.

[207] Chunlei Qiu, et al., A new approach to develop palladium-modified Ti-based alloys

for biomedical applications, Mater. Des. 2016; 109:98-111.

[208] Junlei Tang, Yu Zuo, Study on corrosion resistance of palladium films on 316L stainless steel by electroplating and electroless plating, Corrosion Sci. 2008; 50:2873-2878.

[209] Y.Y. Shi, et al., Electrophoretic deposition of graphene oxide reinforced chitosanehydroxyapatite nanocomposite coatings on Ti substrate, J. Mater. Sci. Mater. Med. 2016; 27:48.

[210] Marija S. Djosic, Miodrag Mitric, VB Miskovic-Stankovic, The porosity and roughness of electrodeposited calcium phosphate coatings in simulated body fluid, J. Serb. Chem. Soc. 2015; 80:237-251.

[211] Chang L, et al., One-pot synthesis of grapheneechitosan nanocomposite modified carbon paste electrode for selective determination of dopamine, Electron. J. Biotechnol. 2014; 17:183-188.

[212] A.R. Rafieerad, et al., Mechanical properties, corrosion behavior and in-vitro bioactivity of nanostructured Pd/PdO coating on Tie6Ale7Nb implant, Mater. Des. 2016; 103:10-24.

[213] Marija Đošic, Sanja Erakovic, Ana Jankovic, Maja Vukašinov-Sekulic, Ivana Z. Matic, Jovica Stojanovic, Kyong Yop Rhee, Vesna Miškovic, Stankovic, Soo-Jin Parke, In vitro investigation of electrophoretically deposited bioactive hydroxyapatite/chitosan coatings reinforced by graphene, J Ind Eng Chem 2017; 47:336–347.

[214] Došić, Marija S., Miodrag Mitrić, and Vesna B. Mišković-Stanković. The porosity and roughness of electrodeposited calcium phosphate coatings in simulated body

fluid. J Serb Chem Soc 2015; 80:237-251.

[215] Liu, C, et al. One-pot synthesis of graphene–chitosan nanocomposite modified carbon paste electrode for selective determination of dopamine. Electron J Biotechn 2014; 17:183-188.

[216] Z. Pawlak, T. Kaldonski, R. Pai, E. Bayraktar, A. Oloyede, A comparative study on the tribological behaviour of hexagonal boron nitride (h-BN) as lubricating micro-particlesdan additive in porous sliding bearings for a car clutch, Wear 2009; 267:1198-1202.

[217] Seiji B, Shigeo M, Morphology and microstructure of electrochemically deposited calcium phosphates in a modified simulated body fluid, Biomaterials 1998; 19:1245-1253.

[218] Xie, Y, et al. Effects of graphene plates' adoption on the microstructure, mechanical properties, and in vivo biocompatibility of calcium silicate coating. Int J Nanomedicine 2015; 10:3855.

[219] Kvetková, L, et al. Fracture toughness and toughening mechanisms in graphene platelet reinforced Si3N4 composites. Scripta Mater 2012; 66: 793-796.

[220] E Mohseni, E Zalnezhad, AR Bushroa, Comparative investigation on the adhesion of hydroxyapatite coating on Ti–6Al–4V implant: A review paper, International Journal of Adhesion and Adhesives 48, 238-257.